Cell

A microbial amino-acid-conjugated bile acid, tryptophan-cholic acid, improves glucose homeostasis via the orphan receptor MRGPRE

Graphical abstract

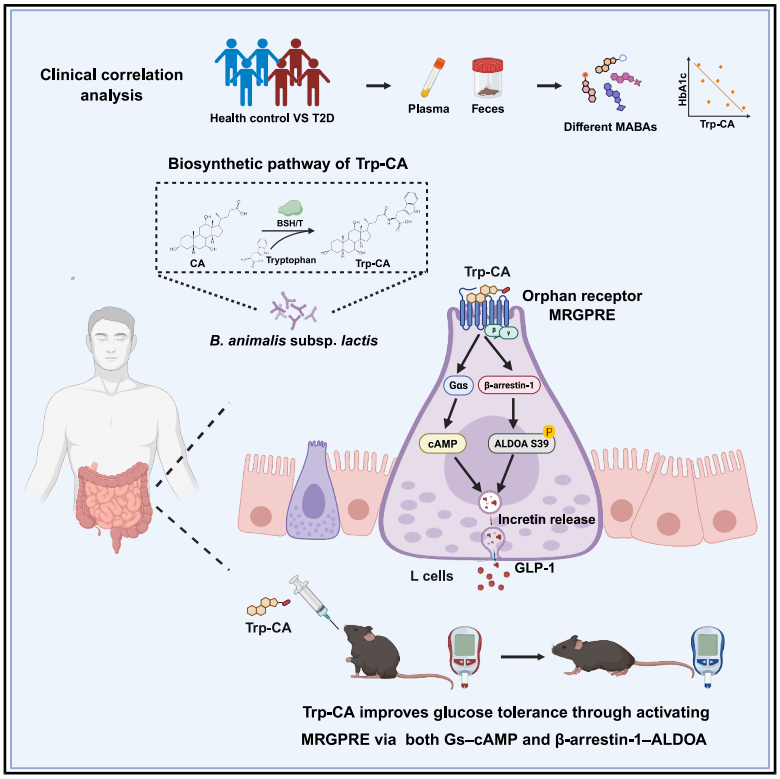

Highlights

- Revealed microbiota-host interaction via microbial amino-acid-conjugated bile acids
- Trp-CA serves as the endogenous ligand of the orphan GPCR MRGPRE
- Identified a non-itch function of the itch family receptor MRGPRE in glucose control
- MRGPRE activation boosts GLP-1 secretion via the Gs-cAMP and β-arrestin-1-ALDOA pathways

Authors

Jun Lin, Qixing Nie, Jie Cheng, ..., Yanli Pang, Jin-Peng Sun, Changtao Jiang

Correspondence

yuxiao@sdu.edu.cn (X.Y.),
jiln@bjmu.edu.cn (L.J.),
yanlipang@bjmu.edu.cn (Y.P.),
sunjinpeng@sdu.edu.cn (J.-P.S.),
jiangchangtao@bjmu.edu.cn (C.J.)

In brief

The microbial-derived bile acid tryptophan-conjugated cholic acid improves type 2 diabetes by promoting GLP-1 secretion in the intestine via activation of the orphan GPCR MRGPRE, revealing another candidate receptor for bile acids and its physiological and pathophysiological importance.

Lin et al., 2025, Cell *188*, 1–19
August 21, 2025
https://doi.org/10.1016/j.cell.2025.05.010

CellPress

Cell

CellPress

Article

A microbial amino-acid-conjugated bile acid, tryptophan-cholic acid, improves glucose homeostasis via the orphan receptor MRGPRE

Jun Lin,[1,2,3,18] Qixing Nie,[1,2,4,18] Jie Cheng,[5,6,18] Ya-Ni Zhong,[5,18] Tianyao Zhang,[5,18] Xiuying Zhang,[7,18] Xiaoyan Ge,[6,18] Yong Ding,[1,2,3,18] Canyang Niu,[5,8] Yuhua Gao,[1,2,3] Kai Wang,[1,2,3] Mingxin Gao,[9] Xuemei Wang,[1,2,3] Weixuan Chen,[10] Chuyu Yun,[10] Chuan Ye,[1,2,3] Jinkun Xu,[1,2,3] Weike Shaoyong,[1,2,3] Lijun Zhang,[9] Pan Shang,[5,6] Xi Luo,[1,2,3] Zhiwei Zhang,[1,2,3] Xin Zheng,[9] Xueying Sha,[9] Jinxin Zhang,[1,2,3] Shaoping Nie,[4] Xuguang Zhang,[11] Fazheng Ren,[12] Huiying Liu,[1,2,3] Erdan Dong,[8,13,14] Xiao Yu,[9,*] Linong Ji,[7,*] Yanli Pang,[1,15,16,*] Jin-Peng Sun,[5,6,*] and Changtao Jiang[1,2,3,17,19,*]

[1]Department of Immunology, School of Basic Medical Sciences, State Key Laboratory of Female Fertility Promotion, Center for Reproductive Medicine, Third Hospital, Peking University, Beijing, China

[2]NHC Key Laboratory of Medical Immunology, Peking University, Beijing, China

[3]Department of Physiology and Pathophysiology, Center for Obesity and Metabolic Disease Research, School of Basic Medical Sciences, State Key Laboratory of Vascular Homeostasis and Remodeling, Peking University, Beijing 100191, China

[4]State Key Laboratory of Food Science and Resources, China-Canada Joint Lab of Food Science and Technology, Key Laboratory of Bioactive Polysaccharides of Jiangxi Province, Nanchang University, Nanchang, China

[5]Department of Biochemistry and Molecular Biology, School of Basic Medical Sciences, Shandong University, Jinan, China

[6]Advanced Medical Research Institute, Meili Lake Translational Research Park, Cheeloo College of Medicine, Shandong University, Jinan, China

[7]Department of Endocrinology and Metabolism, Peking University People's Hospital, Peking University Diabetes Centre, Beijing, China

[8]Research Center for Cardiopulmonary Rehabilitation, University of Health and Rehabilitation Sciences Qingdao Hospital (Qingdao Municipal Hospital), School of Health and Life Sciences, University of Health and Rehabilitation Sciences, Qingdao, China

[9]Key Laboratory Experimental Teratology of the Ministry of Education and Department of Physiology, School of Basic Medical Sciences, Shandong University, Jinan, China

[10]Department of Obstetrics and Gynecology, Peking University Third Hospital, Beijing, China

[11]Shanghai Institute of Nutrition and Health, The Chinese Academy of Sciences, Shanghai, China

[12]Department of Nutrition and Health, Beijing Advanced Innovation Center for Food Nutrition and Human Health, China Agricultural University, No. 10 Tianxiu Road, Haidian District, Beijing 100193, China

[13]The Institute of Cardiovascular Sciences, School of Basic Medical Sciences, State Key Laboratory of Vascular Homeostasis and Remodeling, NHC Key Laboratory of Cardiovascular Molecular Biology and Regulatory Peptides, Beijing Key Laboratory of Cardiovascular Receptors Research, Health Science Center, Peking University, Beijing, China

[14]Department of Cardiology and Institute of Vascular Medicine, Peking University Third Hospital, Beijing, China

[15]National Clinical Research Center for Obstetrics and Gynecology (Peking University Third Hospital), Beijing, China

[16]Beijing Advanced Center of Cellular Homeostasis and Aging-Related Diseases, Institute of Advanced Clinical Medicine, Peking University, Beijing, China

[17]Center of Basic Medical Research, Institute of Medical Innovation and Research, Peking University Third Hospital, Beijing, China

[18]These authors contributed equally

[19]Lead contact

*Correspondence: yuxiao@sdu.edu.cn (X.Y.), jiln@bjmu.edu.cn (L.J.), yanlipang@bjmu.edu.cn (Y.P.), sunjinpeng@sdu.edu.cn (J.-P.S.), jiangchangtao@bjmu.edu.cn (C.J.)

https://doi.org/10.1016/j.cell.2025.05.010

SUMMARY

Recently, microbial amino-acid-conjugated bile acids (MABAs) have been found to be prevalent in human samples. However, their physiological significance is still unclear. Here, we identify tryptophan-conjugated cholic acid (Trp-CA) as the most significantly decreased MABA in patients with type 2 diabetes (T2D), and its abundance is negatively correlated with clinical glycemic markers. We further demonstrate that Trp-CA improves glucose tolerance in diabetic mice. Mechanistically, we find that Trp-CA is a ligand of the orphan G protein-coupled receptor (GPCR) Mas-related G protein-coupled receptor family member E (MRGPRE) and determine the binding mode between the two. Both MRGPRE-Gs-cyclic AMP (cAMP) and MRGPRE-β-arrestin-1-aldolase A (ALDOA) signaling pathways contribute to the metabolic benefits of Trp-CA. Additionally, we find that the bacterial bile salt hydrolase/transferase of *Bifidobacterium* is responsible for the production of Trp-CA. Together, our findings pave the way for further research on MABAs and offer additional therapeutic targets for the treatment of T2D.

INTRODUCTION

Type 2 diabetes (T2D) is a growing global health concern, frequently associated with obesity, fatty liver disease, and cardiovascular issues.[1] The gut microbiota plays a key role in host health maintenance and disease prevention.[2,3] In recent years, increasing evidence suggests that the gut microbiota and their metabolites, particularly bile acids, significantly influence host glucose homeostasis and act as critical signaling molecules in glucose and energy metabolism.[4–6]

Although many studies have reported that certain bile acids and their analogs improve host metabolism, the presence of treatment-emergent adverse events still hinders the clinical application of bile-acid-related drugs, particularly the occurrence of pruritus (i.e., incessant itch).[7,8] Compared with traditional bile acids, newly discovered types of bile acids are an untapped resource with great potential to overcome bile acid deficiencies. Notably, amino-acid-conjugated bile acids, the most frequent of which are glycine or taurine conjugates, are synthesized by the enzyme bile acid coenzyme A:amino acid N-acyltransferase (BAAT) in the liver.[9] However, recent studies have reported that gut microbes can conjugate bile acids with a variety of other amino acids to produce microbial amino-acid-conjugated bile acids (MABAs).[10,11] Subsequently, the presence of nearly all the MABAs was confirmed in the human intestine lumen and stool by using a special sampling capsule or reverse metabolomics approach.[12,13] Although bacterial re-conjugation of bile acids shapes the host bile acid pool, it is not yet understood whether such bile acids have important normo- or pathophysiological effects. Previously well-studied bile acids mainly play a role in host glucose homeostasis via activation of two receptors: farnesoid X receptor (FXR) and Takeda G-coupled protein receptor 5 (TGR5).[8] But it is still unclear whether bile acids, including MABAs, activate other receptors that are involved in regulating glucose homeostasis.

G protein-coupled receptors (GPCRs) are important pharmacological targets, including for the treatment of T2D.[14] However, many GPCRs remain orphaned as their endogenous ligand(s) has not been identified, and thus the identification of such ligands has the potential to provide key insights into physiology as well as further drug development.[15] Here, we identified the orphan GPCR, Mas-related G protein-coupled receptor family member E (MRGPRE), as a previously unknown bile acid receptor. MRGPRE belongs to the itch receptor family, but it is not currently reported to activate itch.[16,17] Heretofore, its physiological function remained unclear.

In this study, we used untargeted metabolomics to explore if the newly discovered MABAs are linked to clinical glycemic markers. We found that tryptophan-conjugated cholic acid (Trp-CA) was significantly lower in patients with T2D compared with healthy controls. We then showed that Trp-CA improved glucose tolerance in high-fat diet (HFD)-fed mice independently of classical bile acid receptors. We screened the most highly expressed GPCRs in the intestine and found that the orphan receptor MRGPRE is the receptor of Trp-CA. Together, our data reveal the microbial production of Trp-CA and drug development for MRGPRE as potential therapeutic strategies to treat T2D.

RESULTS

Trp-CA is negatively correlated with clinical glycemic markers

To identify potential MABAs that are associated with the improvement of T2D, we enrolled 80 individuals that were newly diagnosed with T2D (n = 40) or were considered healthy as controls (n = 40) (Figure 1A; Table S1). We found that the fecal metabolic profile of the study participants with T2D was strikingly different from the healthy controls (Figure 1B). Based on molecular networking, we observed that many MABAs are present in human feces and further focused on the differences in MABA abundance between the individuals with T2D and the healthy controls by matching the tandem mass spectrometry (MS/MS) spectra of the previously reported MABAs[13] (Figure 1C). We found that among all the MABAs analyzed, Trp-CA was clearly the most different between the two groups, with it being significantly lower in the participants with T2D compared with the healthy controls (Figures 1D, 1E, and S1A). For further validation, we synthesized Trp-CA and compared its MS/MS spectra with that of Trp-CA from human stool and found an identical spectrum and retention time with authentic synthetic standard materials (Figures S1B and S1C). Next, we quantified the MABAs changed in Figure 1D by liquid chromatography (LC)-MS/MS and confirmed that Trp-CA was clearly the most different between the two groups (Figure S1D).

Furthermore, the fecal Trp-CA level was negatively correlated with fasting blood glucose (FBG), percent hemoglobin A1c (%HbA1c), and the body mass index (BMI) but not with triglyceride (TG) levels (Figures 1F, 1G, S1E, and S1F). We should note, however, that Trp-CA was a very minor quantitative component of the bile acid pool. Even so, it was stably detected with the equivalent weight of glycodeoxycholic acid (GDCA) and glycoursodeoxycholic acid (GUDCA) (Figure S1G), two bile acids stably detected in the population with a previously defined physiological function.[18,19]

Trp-CA improves glucose homeostasis and ameliorates obesity in HFD-fed mice

Consistent with the clinical results above, we found significantly lower fecal Trp-CA levels in mice induced to have T2D induced by 8 weeks of HFD feeding compared with control mice fed a normal chow diet (Figure 1H). In addition, Trp-CA was largely undetectable in the feces of antibiotic-treated specific-pathogen-free (SPF) and germ-free (GF) mice, indicating the contribution of the gut microbiota to the production of Trp-CA (Figures S1H and S1I). Considering that bacterial bile salt hydrolase/transferase (BSH/T) can hydrolyze host-conjugated bile acids to free bile acids,[20] we then incubated Trp-CA with human stool-derived *ex vivo* communities for 1 day. Unlike glycocholic acid (GCA), we found that Trp-CA was relatively stable in the microecological environment (Figure S1J).

We next explored whether Trp-CA can alleviate glucose intolerance in diabetic mice. Though Trp-CA did not cause any difference in body weight and glucose tolerance in chow diet-fed mice (Figures S1K–S1M), Trp-CA-gavaged mice showed a significantly lower weight gain compared with control mice, accompanied by lower fat mass and food intake upon HFD feeding

Please cite this article in press as: Lin et al., A microbial amino-acid-conjugated bile acid, tryptophan-cholic acid, improves glucose homeostasis via the orphan receptor MRGPRE, Cell (2025), https://doi.org/10.1016/j.cell.2025.05.010

CellPress

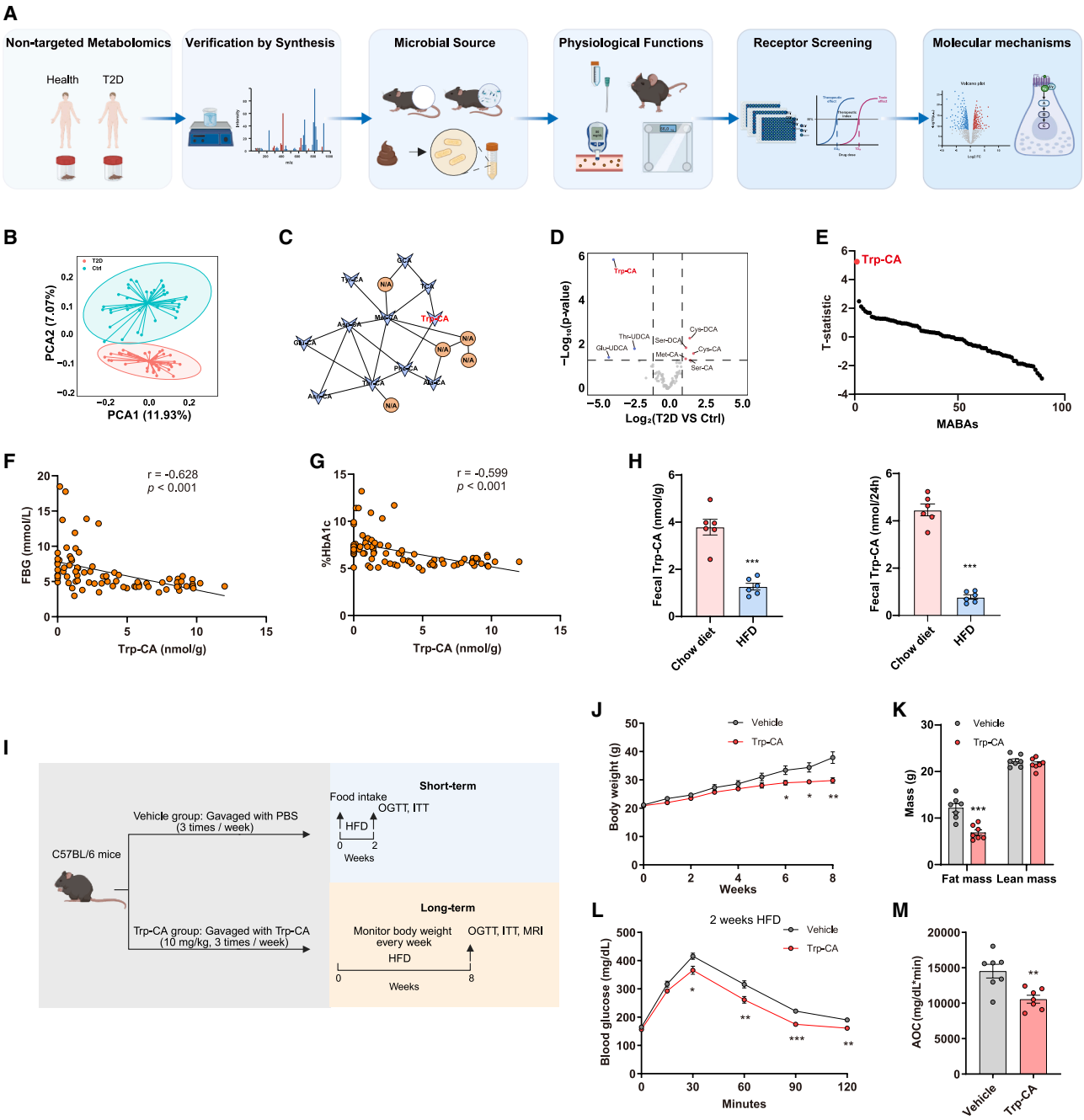

Figure 1. Trp-CA alleviates HFD-induced glucose intolerance

(A) A schematic illustrating the overall research flow of this paper.

(B) Metabolomic profile of the fecal samples between healthy controls and patients with T2D (n = 40/group).

(C) Molecular network of liquid chromatography-tandem mass spectrometry (LC-MS/MS) data for the identification of the interesting feature. Features were annotated by spectral matching in Global Natural Product Social Molecular Networking (GNPS). NA, not annotated.

(D) Volcano plot depicting differential MABAs between healthy controls and patients with T2D.

(E) T-statistics of detected MABAs from untargeted metabolomics.

(F and G) Correlative analysis of fecal Trp-CA level with FBG (F) and %HbA1c (G) (n = 80). Correlations between variables were assessed by linear regression analysis. Linear correction index r and p values were calculated.

(H) Trp-CA concentrations in feces (left) or 24 h fecal Trp-CA output (right) from control mice and HFD-fed mice (n = 6 mice/group).

(I) Experimental scheme for (J)–(M) (n = 7 mice/group).

(J) Body weight.

(K) Fat mass and lean mass.

(legend continued on next page)

(Figures 1I–1K and S1N). Furthermore, Trp-CA-gavaged mice were more glucose sensitive relative to control mice after 8 weeks of consuming an HFD based on the area of curve (AOC) in oral glucose tolerance tests (OGTTs)[21] (Figures S1O and S1P). The glucose improvement in Trp-CA-treated mice occurred within 2 weeks of HFD feeding, before body weight changes, suggesting an obesity-independent effect (Figures 1L and 1M). However, improved insulin resistance at 8 weeks seems weight-loss related (Figures S1Q and S1R). To confirm the therapeutic effect of Trp-CA in mice with established obesity, C57BL/6J mice were subjected to HFD feeding for 8 weeks and kept on the HFD after a 2-week treatment with PBS or Trp-CA (Figure S1S). We found that Trp-CA administration significantly improved glucose tolerance of the obese mice compared with the vehicle control (Figures S1T and S1U).

Trp-CA is an endogenous ligand of the orphan GPCR receptor MRGPRE

By analyzing Trp-CA levels in different tissues from untreated SPF mice, we found that the levels of Trp-CA were vastly higher in the feces and intestinal contents than in the intestinal tissues, and it could not be detected in either the serum or the liver (Figure S2A). As noted, 2-week Trp-CA-gavaged mice showed increased Trp-CA concentrations in the gut lumen compared with control mice but did not differ in the composition of the bile acid pool due to the stability of Trp-CA (Figures S1J, S2A, and S2B). To elucidate the site of Trp-CA action and its acute glucoregulatory effects, we conducted hyperglycemic clamps in mice with duodenal, colonic, and intravenous delivery of Trp-CA. A small intestinal catheter was placed in the intestine to target the duodenum or colon during a 50-min infusion.[22,23] The data revealed that colonic delivery of Trp-CA significantly promoted the first and the second phase of insulin secretion accompanied by an increased glucose infusion rate (GIR), but duodenal and intravenous infusion of Trp-CA did not (Figures S2C–S2N). To examine whether Trp-CA treatment alters insulin sensitivity (i.e., the index of GIR) to impact hepatic glucose production and glucose uptake, we conducted hyperinsulinemic-euglycemic clamps in C57BL/6J mice with duodenal, colonic, and intravenous delivery of Trp-CA (Figure S2O). We observed that intestinal infusion of Trp-CA significantly increased the GIR due to lower glucose production and unaltered glucose uptake, but intravenous delivery of Trp-CA did not (Figures S2P–S2AG). These above data revealed the glucoregulatory role of Trp-CA, which primarily acts in the intestine. Consistent with Trp-CA levels in different tissues, pharmacokinetic data indicated that Trp-CA has poor oral absorption and is unlikely to affect peripheral tissues as it cannot enter the circulation (Figures S3A and S3B). Thus, it may affect host glucose metabolism through receptors in intestinal tissues.

To explore whether Trp-CA promotes glucose tolerance through known bile acid receptors,[5,6,8,24–26] such as TGR5, FXR, vitamin D receptor (VDR), and the pregnane X receptor (PXR), we tested the effects of Trp-CA on these receptors by luciferase reporter gene assays. However, under conditions close to the physiological concentration of Trp-CA in the intestinal contents, Trp-CA failed to affect the activity of these receptors *in vitro* (Figures S3C–S3G).

GPCRs are critical sensors of diverse small molecules and regulate various aspects of host physiology.[15] Thus, we hypothesized that Trp-CA could improve glucose homeostasis via a GPCR. Using the parallel receptorome expression and screening via transcriptional output-Tango (PRESTO-Tango) system,[27] we screened Trp-CA for activation of the top 100 GPCRs, based on their relative gene expression in the intestine from a public transcriptomic data (GEO: GSE46843). We found that Trp-CA could only significantly activate MRGPRE, a member of the itch family receptors[16] (Figure 2A).

Ligand binding to GPCRs is often coupled with extracellular conformational changes, which can be detected by a fluorescein arsenical hairpin-bioluminescence resonance energy transfer (FlAsH-BRET) assay.[17,28–31] We utilized this assay to screen specific positions of extracellular loops (ECLs) that incorporate FlAsH motifs to identify the Trp-CA-induced conformational alterations that occur at the extracellular region of *Homo sapiens* MRGPRE (hMRGPRE). Notably, Trp-CA induced the separation of both ECL1 and ECL3 from the N terminus of hMRGPRE, indicating a potential structural rearrangement between ECL1 or ECL3 and the N terminus of hMRGPRE coupled to Trp-CA binding (Figures 2B, 2C, S3H, and S3I). Moreover, similar conformational changes between ECL1 and the N terminus were detected in mouse MRGPRE by FlAsH-BRET assays (Figures S3J–S3M). Taken together, these findings provide a structural perspective on the activation of MRGPRE induced by Trp-CA.

Next, we used CRISPR-Cas9 to generate *Mrgpre*$^{-/-}$ mice and administrated Trp-CA to them by oral gavage (Figures 2D and S3N). Upon a 2-week HFD feeding regimen, treatment with Trp-CA significantly improved glucose intolerance in *Mrgpre*$^{+/+}$ mice, while *Mrgpre*$^{-/-}$ mice on the same HFD-bile acid treatment regimen failed to show a beneficial effect (Figures 2E and 2F). Furthermore, we crossed *Villin*-Cre mice with *Mrgpre*$^{fl/fl}$ mice to enable the selective loss of *Mrgpre* expression in the intestine (*Mrgpre*$^{\Delta IE}$) (Figures S3O and S3P). Body weight and cumulative food intake on a chow diet and on an HFD were similar in *Mrgpre*$^{\Delta IE}$ mice versus control mice for each diet (Figures S3Q, S3R, S3U, and S3V). Glucose tolerance was slightly attenuated in *Mrgpre*$^{\Delta IE}$ mice on a chow diet compared with floxed controls, and this defect was more apparent in the mutant mice compared with the floxed controls after HFD feeding (Figures S3S, S3T, S3W, and S3X). Consistent with *Mrgpre*$^{-/-}$ mice, the beneficial effects of Trp-CA on glucose metabolism in *Mrgpre*$^{\Delta IE}$ mice

(L) Blood glucose in OGTTs of 2-week HFD-fed mice.
(M) AOC of OGTTs.
All data are presented as the means ± SEMs. In (H), the *p* values were determined by a two-tailed Student's t test with Welch's correction. In (K) and (M), the *p* values were determined by a two-tailed Student's t test. In (J) and (L), the *p* values were determined by two-way repeated-measures ANOVA with unpaired Student's t test post hoc. $^{*}p < 0.05$, $^{**}p < 0.01$, and $^{***}p < 0.001$ versus the control group.
See also Figures S1 and S2.

Please cite this article in press as: Lin et al., A microbial amino-acid-conjugated bile acid, tryptophan-cholic acid, improves glucose homeostasis via the orphan receptor MRGPRE, Cell (2025), https://doi.org/10.1016/j.cell.2025.05.010

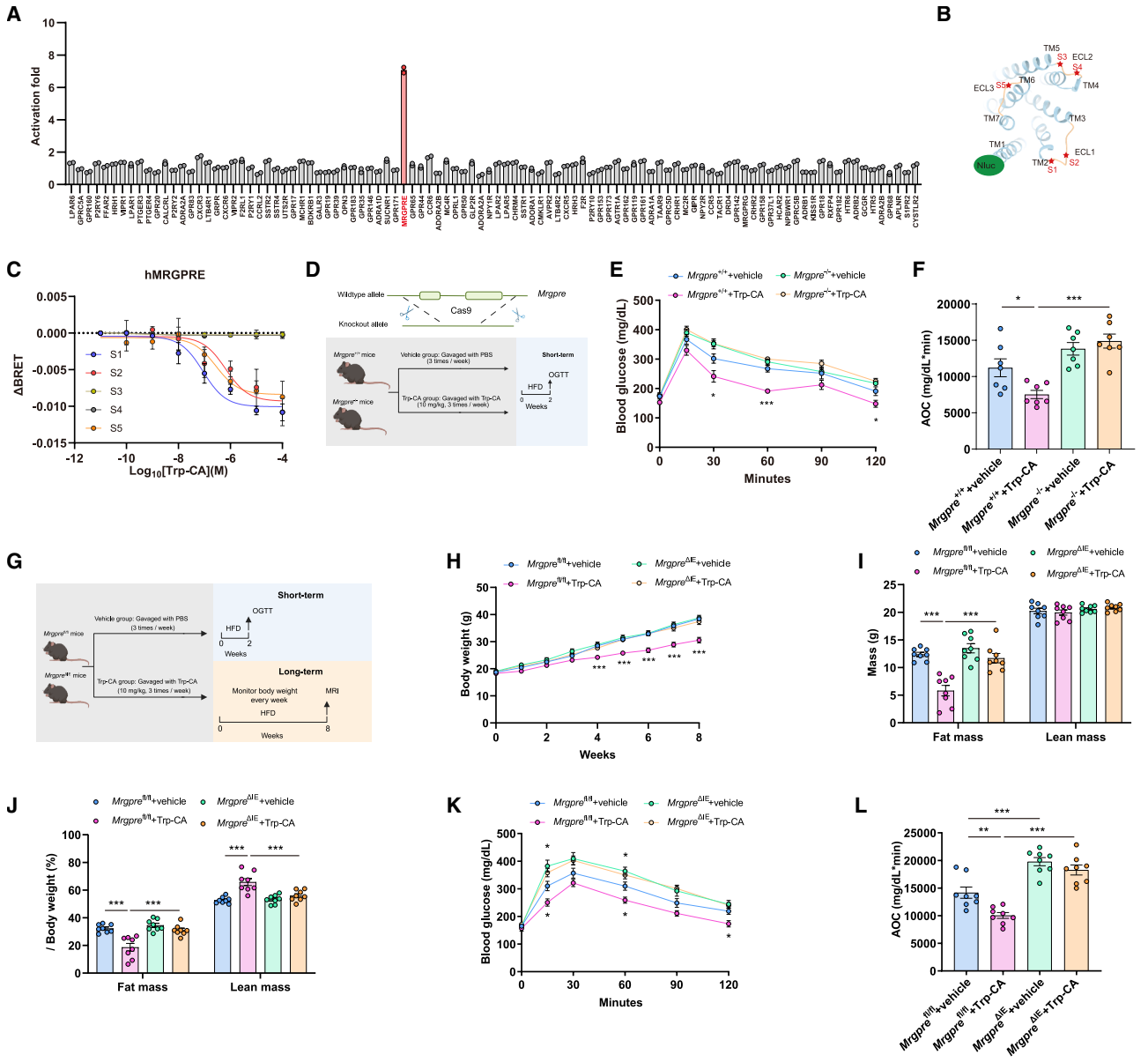

Figure 2. Trp-CA is an endogenous ligand of the orphan receptor MRGPRE

(A) Activation fold of GPCRs by 10 μM Trp-CA as measured by the PRESTO-Tango system.

(B) Schematic representation of the FlAsH-BRET assay design. The NLUC was inserted at the N-terminal of hMRGPRE (hMRGPRE), and the FlAsH motifs were inserted in the designated positions in the figure.

(C) Representative curves of five MRGPRE FlAsH-BRET sensors in response to Trp-CA stimulation. $n = 3$ biological replicates.

(D) Experimental scheme for (E) and (F) ($n = 7$ mice/group).

(E) Blood glucose in OGTTs.

(F) AOC of OGTTs.

(G) Experimental scheme for (H)–(L) ($n = 8$ mice/group).

(H) Body weight.

(I) Fat mass and lean mass.

(J) The ratio of fat mass and lean mass to body weight.

(K) Blood glucose in OGTTs of 2-week HFD-fed mice.

(L) AOC of OGTTs.

All data are presented as the means ± SEMs. In (E), (H), and (K), the p values were determined by two-way repeated-measures ANOVA with least significant difference (LSD) test. In (F), (I), (J), and (L), the p values were determined by two-way ANOVA with Tukey's post hoc test. $^{*}p < 0.05$, $^{**}p < 0.01$, and $^{***}p < 0.001$ versus the control group.

See also Figure S3.

Please cite this article in press as: Lin et al., A microbial amino-acid-conjugated bile acid, tryptophan-cholic acid, improves glucose homeostasis via the orphan receptor MRGPRE, Cell (2025), https://doi.org/10.1016/j.cell.2025.05.010

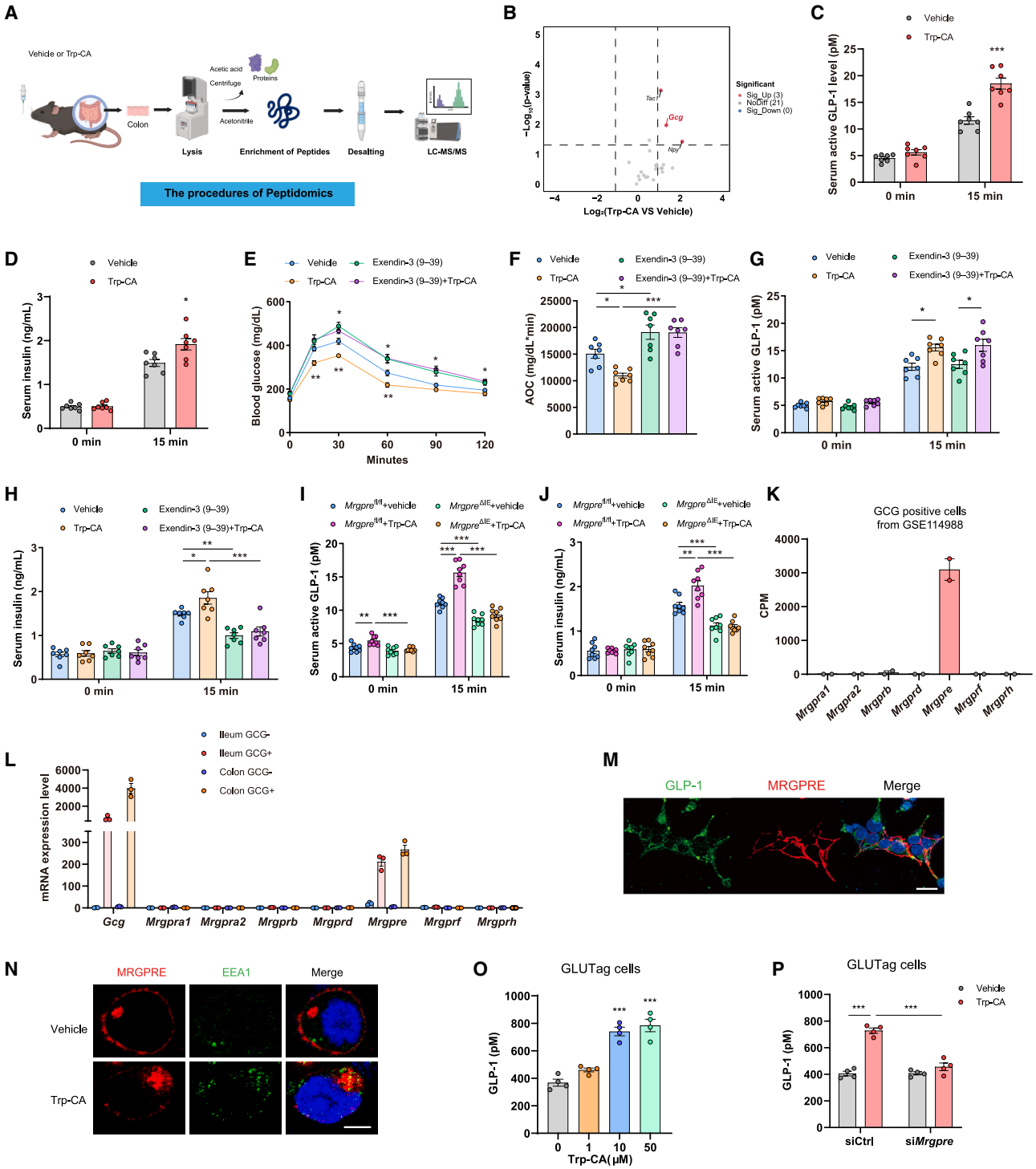

Figure 3. Trp-CA improves glucose tolerance by promoting GLP-1 secretion

(A) A schematic diagram illustrating the workflow of peptidomics.

(B) Volcano map of peptidomics analysis showing fold change of protein abundance in colon tissues from mice treated with PBS or Trp-CA versus $-\log_{10}$ (*p* values).

(C and D) Serum active GLP-1 (C) and insulin (D) levels at 0 and 15 min after oral glucose gavage ($n = 7$ mice/group). Related to Figure 1L.

(E–H) HFD-fed C57BL/6J mice were treated with PBS (vehicle), Trp-CA (10 mg/kg), exendin-3 (9–39), and exendin-3 (9–39) with Trp-CA (10 mg/kg), three times per week for the 2 weeks ($n = 7$ mice/group).

(E) Blood glucose in OGTTs of 2-week HFD-fed mice.

(legend continued on next page)

were completely blunted, as indicated by a lack of a beneficial effect on body weight, fat mass, and glucose tolerance compared with control mice (Figures 2G–2L).

To examine whether the acute glucoregulatory role of Trp-CA relies on an MRGPRE-dependent signaling pathway, we performed hyperglycemic and hyperinsulinemic-euglycemic clamps in *Mrgpre*$^{fl/fl}$ and *Mrgpre*$^{\Delta IE}$ mice with colonic infusion of Trp-CA or vehicle. We observed that colonic infusion of Trp-CA promoted 1st and 2nd phase insulin secretion and a higher GIR in *Mrgpre*$^{fl/fl}$ mice, while *Mrgpre*$^{\Delta IE}$ mice failed to show these beneficial effects of Trp-CA (Figures S3Y–S3AB). In addition, Trp-CA significantly increased the GIR due to lower glucose production and unaltered glucose uptake in *Mrgpre*$^{fl/fl}$ mice but not in *Mrgpre*$^{\Delta IE}$ mice (Figures S3AC–S3AH). These data collectively demonstrate that MRGPRE is a receptor for Trp-CA and acts *in vivo* to mediate the beneficial effects of Trp-CA on glucose metabolism.

Trp-CA induces GLP-1 secretion via MRGPRE activation

Given the lumen-restricted nature of Trp-CA and the glucoregulatory role of Trp-CA in the intestine (Figure S2), we speculated that it might improve glucose metabolism by affecting gut hormone secretion. We performed peptidomics analysis of colon tissue from the mice treated with or without Trp-CA (Figure 3A). Among the 24 genes with the annotation of peptides, *Gcg*, *Tac1*, and *Npy* showed higher levels in the Trp-CA-treated mice compared with the control-treated mice (Figure 3B). *Gcg*, whose gene encodes for pro-glucagon, is eventually cleaved into glucagon-like peptides, including glucagon-like peptide (GLP)-1 and GLP-2, in the intestine.[32] Thus, we detected serum insulin and GLP-1 levels at 0 and 15 min after delivery of a bolus of oral glucose in mice treated with PBS or Trp-CA for 2 weeks and found that Trp-CA was associated with a greater level of serum insulin and GLP-1 level at the 15 min time point compared with vehicle-treated mice, while there was no difference in the levels of gastric inhibitory polypeptide (GIP), another potent stimulator of insulin secretion (Figures 3C, 3D, and S4A).

To further confirm that the beneficial effects of 2-week-Trp-CA gavage on glucose homeostasis were caused by elevation of GLP-1 levels, we inhibited the GLP-1 receptor in mice using a GLP-1 receptor antagonist, exendin-3 (9–39) amide. We found that Trp-CA still stimulated GLP-1 secretion after GLP-1 receptor inhibition in the exendin + Trp-CA group, while insulin secretion and its hypoglycemic effects were abolished in the exendin + Trp-CA group compared with the Trp-CA group (Figures 3E–3H).

Next, we detected the serum insulin and GLP-1 levels at 0 and 15 min after an oral glucose challenge in *Mrgpre*$^{-/-}$ and *Mrgpre*$^{\Delta IE}$ mice treated with Trp-CA and the corresponding control mice. Genetic ablation of *Mrpgre* resulted in a blunting of the elevation of serum GLP-1 and insulin induced by Trp-CA during an oral glucose challenge or during an oral glucose challenge of the mutant versus floxed control mice on either a chow diet or on an HFD (Figures 3I, 3J, and S4B–S4G). We also observed that the elevation of serum C-peptide induced by Trp-CA disappeared in *Mrgpre*$^{\Delta IE}$ mice (Figure S4H). The GLP-1 contributes to enteral glucose tolerance by enhancing insulin secretion.[33] In addition to OGTTs, we also performed intravenous glucose tolerance tests (IVGTTs) in 2-week Trp-CA-gavaged mice. We observed that an enteral glucose-dependent pathway was necessary for the benefits of chronic Trp-CA treatment on GLP-1 secretion and glucose regulation (Figures S4I–S4L).

Intestinal GLP-1 is produced and secreted by enteroendocrine L cells.[32] Based on information from publicly available databases, we found that *Mrgpre* is highly expressed in GCG-positive (GCG$^+$) cells in the intestine relative to other receptors of the itch family (Figures 3K and S4M). Next, we crossed *Gcg*-Cre mice with *Actb*-tdTomato/EGFP reporter mice to label GLP-1-producing cells. In Cre-expressing offspring, the tdTomato cassette was deleted, enabling membrane-targeted EGFP expression in GCG$^+$ cells, which were then sorted (Figure S4N). Consistent with the public data, we found that *Mrgpre* is highly expressed in GCG$^+$ cells from both the ileum and the colon relative to other receptors of the itch family (Figure 3L).

We further explored the protein expression level of *Mrpgre* in L cells *in vitro* and *in vivo*. After we validated the commercial MRGPRE antibody by performing double staining in HEK293T cells transiently expressing a FLAG-tagged mouse *Mrgpre* construct, we then determined that *Mrgpre* was indeed expressed in L cells *in vitro* and *in vivo* (Figures 3M, S4O, and S4P). Many GPCRs are internalized upon activation.[34] We confirmed MRPGRE was internalized in early endosome antigen 1 (EEA1)-expressing endosomes in GLUTag cells treated with Trp-CA (Figure 3N). Taken together, these results indicate that Trp-CA is a ligand of MRGPRE, which is expressed in enteroendocrine L cells in the gut epithelium.

(F) AOC of OGTTs.
(G and H) Serum active GLP-1 (G) and insulin (H) at 0 and 15 min after oral glucose gavage.
(I and J) Serum active GLP-1 (I) and insulin (J) levels at 0 and 15 min after oral glucose gavage (n = 7 mice/group). Related to Figure 2K.
(K) CPM of itch family receptors in GCG-positive cells from GEO: GSE114988 dataset.
(L) Relative mRNA expression level of *Gcg* and itch family receptors in GCG-negative cells and GCG-positive cells from mice ileum and colon after fluorescence-activated cell sorting (FACS) (n = 3 biological replicates).
(M) Co-immunostaining of MRGPRE and GLP-1 in GLUTag cells. Scale bar, 50 μM.
(N) Co-immunostaining of MRGPRE and EEA1, a marker of endosomes, in GLUTag cells. Scale bar, 20 μM.
(O) Active GLP-1 level in cell culture. GLUTag cells were treated with the indicated dose of Trp-CA for 1 h.
(P) Active GLP-1 level in cell culture. GLUTag cells transfected with an siCtrl or with an si*Mrgpre* were treated with Trp-CA (10 μM) for 1 h.
All data are presented as the means ± SEMs. n = 4 biological replicates for (O) and (P). In (B)–(D), the p values were determined by a two-tailed Student's t test. In (E), the p values were determined by two-way repeated-measures ANOVA with LSD test. In (F)–(H) and (P), the p values were determined by one-way ANOVA with Tukey's post hoc test. In (I) and (J), the p values were determined by two-way ANOVA with Tukey's post hoc test. $^*p < 0.05$, $^{**}p < 0.01$, and $^{***}p < 0.001$ versus the control group.
See also Figure S4.

Please cite this article in press as: Lin et al., A microbial amino-acid-conjugated bile acid, tryptophan-cholic acid, improves glucose homeostasis via the orphan receptor MRGPRE, Cell (2025), https://doi.org/10.1016/j.cell.2025.05.010

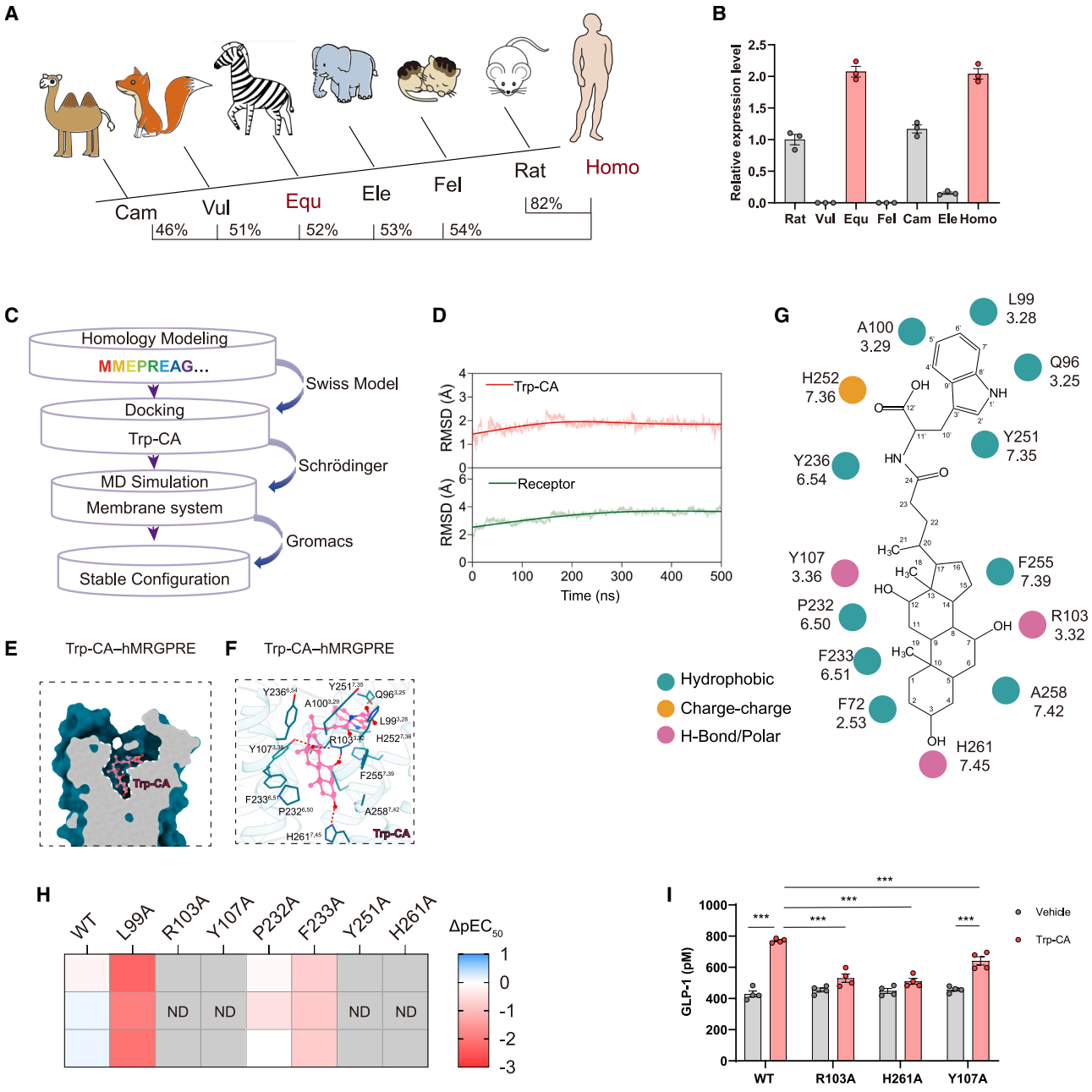

Figure 4. The structural basis of binding and activation of hMRGPRE by Trp-CA

(A) A simplified evolutionary tree of MRGPRE across 7 different mammal species, showing ascending amino acid sequence homology with homo MRGPRE: *Camelus dromedarius* (Cam; 46%), *Vulpes vulpes* (Vul; 51%), *Equus burchelli* (Equ; 52%), *Elephas maximus* (Ele; 53%), *Felis catus* (Fel; 54%), *Rattus norvegicus* (Rat; 82%), and *Homo sapiens* (Homo; 100%), respectively.

(B) The membrane protein levels of seven MRGPRE receptors from different species (n = 3 biological replicates).

(C) A schematic diagram illustrating the strategy of template building, ligand-binding site searching, and molecular dynamics (MD) simulation for Trp-CA-hMRGPRE complex, using our solved cryo-EM structure of the 2-MOA-eqMRGPRE-Gq complex as a template.

(D) The average root-mean-square deviation (RMSD) value of Trp-CA (upper) and hMRGPRE (lower) during triplicate 500 ns of MD simulation.

(E and F) Cutaway view (E) and 3D representation (F) of binding pocket between Trp-CA and hMRGPRE. Hydrogen bonds or polar interactions are shown as red dashed lines.

(G) 2D representation of the interaction between pocket residues of hMRGPRE and Trp-CA during 500 ns MD simulation. The hydrophobic interactions, charge-charge interactions, and hydrogen bonds/polar interactions are colored cyan, orange, and pink, respectively.

(H) Effects of mutations of the binding pocket of MRGPRE in response to stimulation with Trp-CA using a G protein dissociation assay. The heatmap is colored according to the value of ΔpEC_{50} (ΔpEC_{50} = pEC_{50} of mutant − pEC_{50} of WT). ND, not detectable due to low signal (n = 3 independent experiments).

(legend continued on next page)

We further tested the effect of Trp-CA on GLP-1 secretion in two mouse enteroendocrine L cell lines (GLUTag and STC-1) and one human enteroendocrine L cell line (NCI-H716). We found that Trp-CA was able to stimulate GLP-1 secretion at a comparable physiological concentration (10 μM) among all three cell lines (Figures 3O, S2A, S4Q, and S4R). To elucidate the functional role of MRGPRE in Trp-CA-induced GLP-1 secretion of L cell lines, we knocked down the expression of *Mrgpre* in GLUTag cells and STC-1 cells. We observed that *Mrgpre* knockdown cells blocked Trp-CA-induced GLP-1 secretion (Figures 3P and S4S).

Trp-CA induces GLP-1 secretion partially via an MRGPRE-Gs-cAMP pathway

After the discovery of the membrane receptor for Trp-CA, we next investigated the signaling mechanism underlying GLP-1 secretion via Trp-CA stimulation and MRGPRE activation. Firstly, we found that Trp-CA only induced significant Gs dissociation from MRGPRE (half-maximal effective concentration [EC_{50}] = 9.6 ± 1.0 μM) (Figure S5A). Notably, none of the other representative bile acids in our assay activated MRGPRE-Gs signaling (Figure S5B). We then found that Trp-CA dose-dependently induced increased cyclic AMP (cAMP) levels (Figure S5C). Gs-cAMP signaling is a classic pathway for GLP-1 secretion in L cells.[35] As expected, both Gs inhibition and knockdown of Gs protein *in vivo* partially inhibited Trp-CA-induced GLP-1 secretion (Figures S5D–S5M). After confirming that Trp-CA can promote GLP-1 secretion via the Gs-cAMP pathway, we used a Gαs-Gβγ dissociation assay to validate the results of our previous receptor screens by the PRESTO-Tango assay (Figure S5N).

Cryo-EM structure of MRGPRE and interaction between MRGPRE and Trp-CA

We next investigated the interaction between Trp-CA and MRGPRE via a high-resolution structural analysis. Although we assembled the Trp-CA-hMRGPRE complex *in vitro*, the Trp-CA-hMRGPRE complex was prone to aggregation, and thus we were unable to generate a 3D classification to provide a high-resolution cryoelectron microscopy (cryo-EM) map (Figures S6A–S6C). By screening MRGPRE homologs, we found that hMRGPRE and *Equus burchelli* MRGPRE (eqMRGPRE) had the highest relative expression levels (Figures 4A and 4B). A recent study screened >1,000 metabolites against the near-complete GPCRome by using PRESTO-Salsa technology and displayed this dataset in an interactive web interface (http://palmlab.shinyapps.io/presto-salsa/), which shows that 2-methoxycinnamaldehyde (2-MOA) weakly activates hMRGPRE (log_2 activation fold = 1.131906).[36] Although we found that 2-MOA did not activate hMRGPRE based on either Gs or Gq dissociation assays, we found that it did activate Gq signaling of eqMGRPRE (Figure S6D). Using 2-MOA and eqMRGPRE, we were able to form a stable complex and solve the 2-MOA-eqMRGPRE-Gq complex structure at an overall resolution of 2.5 Å (Figures S6E–S6M; Table S2). Gq activation with mutational analysis verified the binding of 2-MOA with eqMRGPRE (Figures S6N–S6P).

We further built the structure model of hMRGPRE utilizing the Swiss-Model software, exploiting the 2-MOA-eqMRGPRE-Gq complex structure as a template (Figures 4C and 4D). According to the "SiteMap" algorithm, we identified 3 potential ligand-binding pockets in the Trp-CA-hMRGPRE complex structure. We next prepared the model of Trp-CA using the "LigPrep" algorithm and performed molecular docking by Schrödinger. Simulation trajectory file from GROMACS revealed potential binding poses of Trp-CA. Further molecular dynamics (MD) simulation results and a free binding energy analysis showed that site 1 was relatively stable (Figures 4D–4F, S6Q, and S6R). In this mode, Trp-CA mainly formed interactions with residues from TM2–TM3 and TM6–TM7. The steroid core of the CA moiety packed parallel to TM6 and inserted into the orthosteric pocket of MRGPRE vertically. The CA moiety is flanked by hydrophobic residues F72$^{2.53}$, P232$^{6.50}$, Y236$^{6.54}$, and F233$^{6.51}$ on one side and F255$^{7.39}$ and A258$^{7.42}$ on the other side. The 3 hydroxyl groups at positions C3, C7, and C12 of Trp-CA formed hydrogen bonds with H261$^{7.45}$ in TM7 and R103$^{3.32}$ and Y107$^{3.36}$ in TM3, respectively. In the middle linker region, the carboxyl group of the main chain of the Trp moiety of Trp-CA formed a charge-charge interaction with H252$^{7.36}$. The tryptophan ring of the Trp moiety inserted in a hydrophobic pocket created by L99$^{3.28}$, A100$^{3.29}$, and Y251$^{7.35}$, forming extensive hydrophobic and π-π packings (Figures 4F and 4G). Notably, mutations of these interaction residues, such as L99$^{3.28}$A, R103$^{3.32}$A, Y107$^{3.36}$A, P232$^{6.50}$, F233$^{6.51}$A, Y251$^{7.35}$A, and H261$^{7.45}$A, resulted in significantly lower Gs activities downstream of hMRGPRE stimulated with Trp-CA (Figures 4H and S6S). Moreover, tryptophan-conjugated chenodeoxycholic acid (Trp-CDCA) and tryptophan-conjugated deoxycholic acid (Trp-DCA), which lack hydroxylation at C12 or C7 positions, respectively, were not able to activate hMRGPRE-Gs signaling (Figure S6T). These results are consistent with our structural model and indicate that the hydrogen bonds between C7/C12 hydroxyl and R103$^{3.32}$/Y107$^{3.36}$ serve as important structural determinants for recognition of Trp-CA by MRGPRE.

Consistently, mutations of critical interaction residues, such as R103$^{3.32}$A, Y107$^{3.36}$A, and H261$^{7.45}$A of MRGPRE, abolished Trp-CA-induced GLP-1 secretion (Figure 4I).

Trp-CA induces GLP-1 secretion partially via an MRGPRE-β-arrestin-1-ALDOA pathway

Inhibition of the Gs-cAMP pathway only partially reversed the effects of Trp-CA *in vitro* and *in vivo*, indicating the possibility of other signaling pathways that contribute to MRGPRE-mediated GLP-1 secretion. Parallel to G protein activities, arrestins act as scaffolds for downstream effectors of GPCR signaling, and thus

(I) Active GLP-1 level in cell culture. MRGPRE KO GLUTag cells transfected with an MRPGRE WT or MRGPRE R103A or MRGPRE H261A or MRGPRE Y107A were treated with/without Trp-CA (10 μM) for 1 h (n = 4 biological replicates).

All data are presented as the means ± SEMs. In (I), the p values were determined by two-way ANOVA with Tukey's post hoc test. ***$p < 0.001$ versus the control group.

See also Figures S5 and S6.

Please cite this article in press as: Lin et al., A microbial amino-acid-conjugated bile acid, tryptophan-cholic acid, improves glucose homeostasis via the orphan receptor MRGPRE, Cell (2025), https://doi.org/10.1016/j.cell.2025.05.010

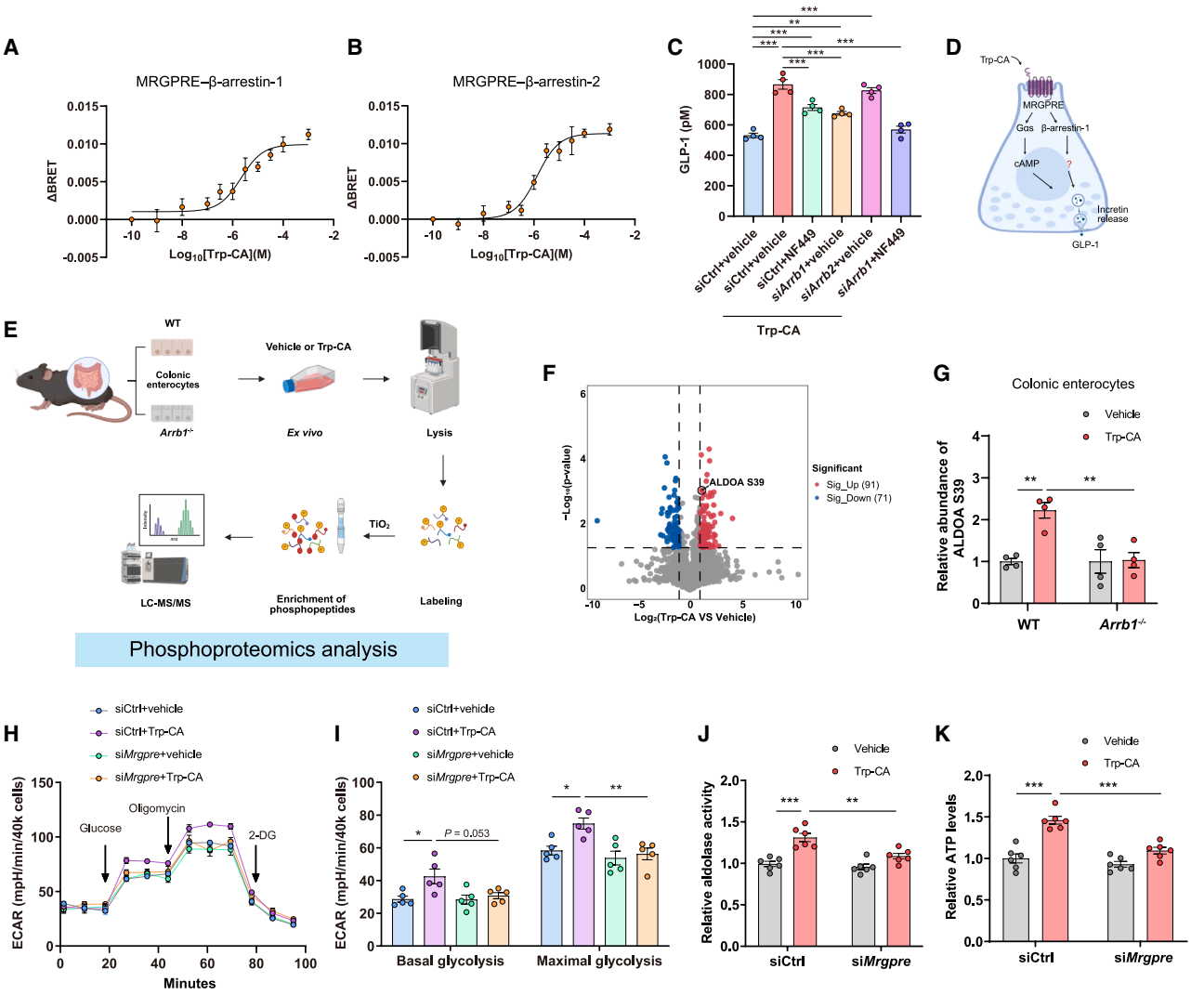

Figure 5. Trp-CA promotes cellular glycolysis by inducing ALDOA phosphorylation

(A and B) Trp-CA-induced β-arrestin-1 (A) or β-arrestin-2 (B) recruitment in HEK293T cells transfected with MRGPRE ($n = 3$).

(C) Active GLP-1 level in cell culture. GLUTag cells transfected with an siCtrl or with an si*Arrb1* or with an si*Arrb2* were treated with DMSO (vehicle), 10 μM Trp-CA, and 10 μM Trp-CA plus 10 μM NF449 (Gs inhibitor) for 1 h. $n = 4$ biological replicates.

(D) Schematic representation of the working hypothesis of how Trp-CA induces GLP-1 secretion via activation of MRGPRE in L cells.

(E) A schematic diagram illustrating the workflow of phosphoproteomics.

(F) Volcano map of phosphoproteomic analysis showing relative fold change ($\log_2$) of protein abundance in intestinal epithelium from mice treated with vehicle or Trp-CA versus $-\log_{10}$ (p values). p values calculated by two-tailed Student's t test.

(G) Quantification of the phosphorylation level of ALDOA (Ser39) in intestinal epithelium isolated from WT or *Arrb1*$^{-/-}$ mice treated with vehicle or 10 mg/kg Trp-CA. $n = 4$ mice/group.

(H and I) Extracellular acidification rate (ECAR) (H) and calculated glycolytic metabolic parameters (I) of GLUTag cells transfected with an siCtrl or with an si*Mrgpre*, which were treated with DMSO (vehicle) or 10 μM Trp-CA for 1 h.

(J and K) Relative aldolase activity (J) and relative ATP level (K) of cell lysates from GLUTag cells transfected with an siCtrl or with an si*Mrgpre*, which were treated with DMSO (vehicle) or 10 μM Trp-CA for 10 min.

All data are presented as the means ± SEMs. $n = 3$ biological replicates for (A) and (B); $n = 5$ biological replicates for (H) and (I); $n = 6$ biological replicates for (J) and (K). In (C), (G), and (I)–(K), the p values were determined by two-way ANOVA with Tukey's post hoc. *$p < 0.05$, **$p < 0.01$, and ***$p < 0.001$ versus the control group. See also Figure S7.

GPCR-arrestin-effector signalosomes exist to convey specific functions independently of GPCR-G protein complexes.[37–45] Here, we found that MRGPRE dose-dependently recruited β-arrestin-1/2 in response to Trp-CA stimulation (Figures 5A and 5B). We then observed that the beneficial effects of Trp-CA on GLP-1 secretion in GLUTag cells were partly abrogated by small interfering RNA (siRNA)-mediated knockdown of *Arrb1* (the gene encoding β-arrestin-1) but not by knockdown

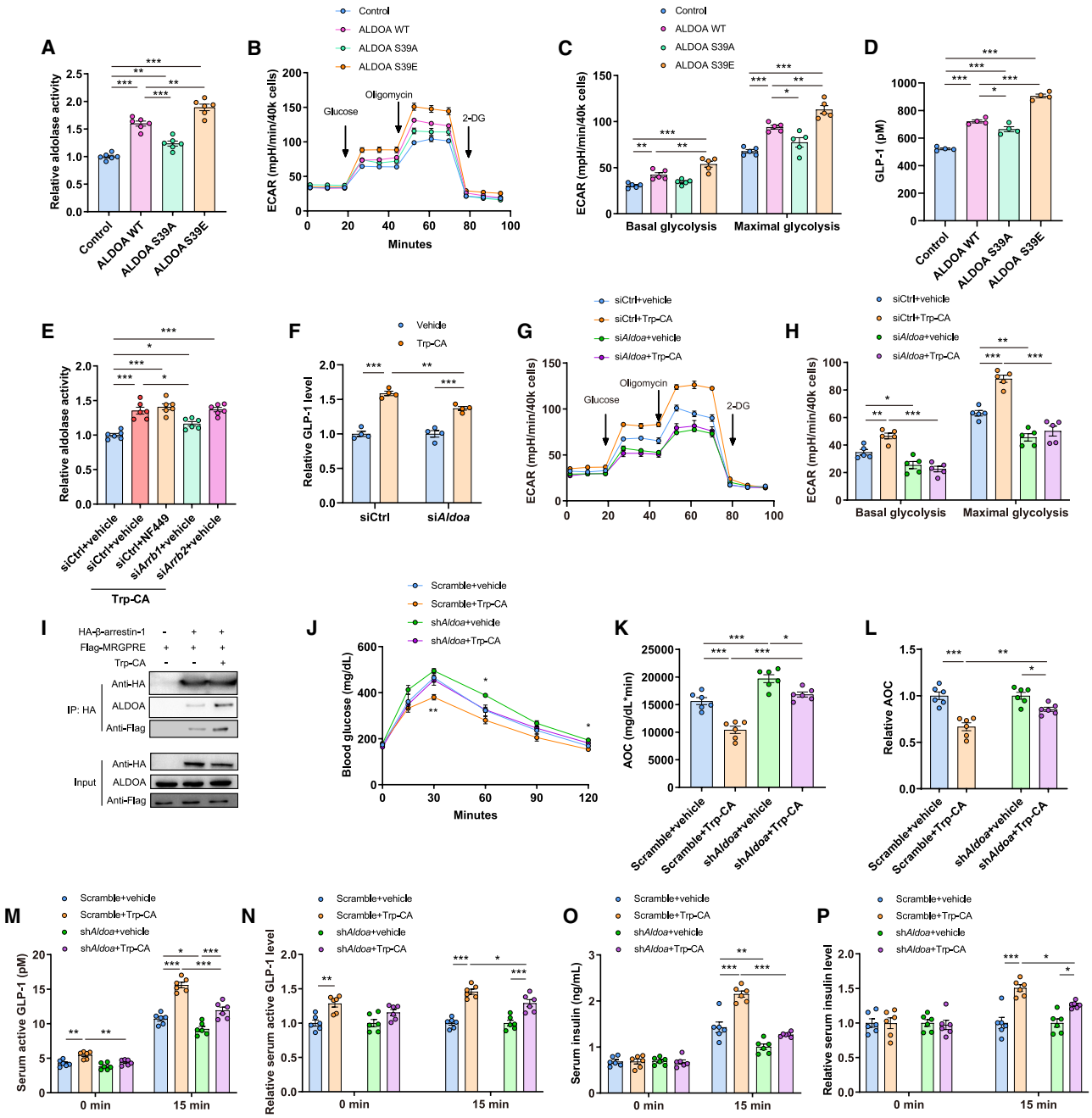

Figure 6. Trp-CA induces GLP-1 secretion partially via an MRGPRE-β-arrestin-1-ALDOA pathway

(A–D) GLUTag cells transfected with empty vector (control), ALDOA WT, ALDOA S39A mutant, and ALDOA S39E mutant.

(A) Relative aldolase activity of indicated cell lysates.

(B and C) ECAR (B) and calculated glycolytic metabolic parameters (C) of indicated GLUTag cell.

(D) Active GLP-1 level in cell culture.

(E) Relative aldolase activity of cell lysates from GLUTag cells transfected with an siCtrl or with an si*Arrb1* or with an si*Arrb2* were treated with DMSO (vehicle), 10 μM Trp-CA, and 10 μM Trp-CA plus 10 μM NF449 for 10 min.

(F) Relative active GLP-1 level in cell culture. Related to Figure S7I.

(G and H) ECAR (G) and calculated glycolytic metabolic parameters (H) of GLUTag cells transfected with an siCtrl or with an si*Aldoa*, which were treated with DMSO (vehicle) or 10 μM Trp-CA for 1 h.

(I) Immunoblot analysis of whole-cell extracts that were immunopurified by anti-hemagglutinin (HA) immunoprecipitation (HA-IP) from HEK293T cells expressed HA-β-arrestin-1 and FLAG-MRGPRE. Where indicated, the cells were pretreated with or without 10 μM Trp-CA for 10 min.

(J–P) HFD-fed scramble and sh*Aldoa* mice were treated with PBS (vehicle), Trp-CA (10 mg/kg) three times per week for 2 weeks (n = 6 mice/group).

(legend continued on next page)

of *Arrb2* (the gene encoding β-arrestin-2) (Figure 5C). Knockdown of *Arrb1* in the presence of NF449 could completely block the effects of Trp-CA in GLUTag cells (Figure 5C). Finally, *in vivo*, we found that Trp-CA-induced GLP-1 and insulin secretion was attenuated in *Arrb1*$^{-/-}$ mice but not in *Arrb2*$^{-/-}$ mice (Figures S7A and S7B). These results demonstrate that Gs-cAMP and β-arrestin-1 signaling both contribute to the effects of Trp-CA on GLP-1 and insulin secretion to regulate glucose homeostasis (Figure 5D).

As scaffold signaling hubs, β-arrestins can promote the phosphorylation of downstream proteins.[46–50] To explore the phosphorylated proteins induced by Trp-CA-MRGPRE-β-arrestin-1 signaling, we performed a quantitative phosphoproteomic analysis in the intestinal epithelium, which was cultured *ex vivo*, of wild-type (WT) littermates and *Arrb1*$^{-/-}$ mice with or without Trp-CA treatment (Figure 5E). We found that the abundance of 91 phosphorylated proteins increased and the abundance of 71 phosphorylated proteins decreased after Trp-CA treatment in WT mice but not in *Arrb1*$^{-/-}$ mice (Figure 5F). Glycolysis increases intracellular ATP concentrations and induces GLP-1 secretion.[51,52] Fructose-bisphosphate aldolase A (ALDOA) was the only differentially phosphorylated protein associated with the glycolytic pathway that was found to be of interest (Figures 5F, 5G, and S7C). Trp-CA-induced S39 phosphorylation of ALDOA was also confirmed in GLUTag cells (Figure S7D). Thus, ALDOA S39 phosphorylation may modulate glycolytic metabolism in L cells. As expected, we found that Trp-CA treatment increased the glycolytic metabolism, aldolase enzyme activity, and ATP levels of control cells but not *Mrgpre* knockdown cells (Figures 5H–5K).

Next, S39 phosphorylation of ALDOA modulated the aldolase enzyme activity in GLUTag cells (Figures 6A and S7E). ALDOA-S39E (phospho-mimetic mutant)-expressing cells showed a greater glycolytic metabolism than ALDOA-WT-expressing cells, and ALDOA-S39A (non-phosphorylatable mutant)-expressing cells showed an impaired glycolytic metabolism compared with ALDOA-WT-expressing cells (Figures 6B, 6C, and S7F). And altered glycolytic metabolism also regulated GLP-1 secretion in GLUTag cells (Figure 6D). Moreover, Trp-CA-induced aldolase activity and ATP production were dependent on β-arrestin-1 recruitment (Figures 6E and S7G). Knockdown of *Aldoa* led to a reduction in glycolytic metabolism and GLP-1 levels (Figures 6F–6H, S7H, and S7I). In addition, we found that non-phosphorylatable ALDOA partly inhibited Trp-CA-induced GLP-1 secretion *in vitro* (Figures S7J and S7K). By co-immunoprecipitation, we found that Trp-CA induced an association of β-arrestin-1 with ALDOA and MRPGRE, which provides a molecular basis of phosphorylation (Figures 6I and S7L).

To explore whether ALDOA mediates the improved effects of Trp-CA on glucose metabolism *in vivo*, we generated *Aldoa* knockdown mice by injection of an short hairpin RNA (shRNA)-expressing lentivirus into the intestine of WT mice and found that *Aldoa* knockdown impaired the beneficial effects of Trp-CA on GLP-1 and insulin levels, as well as on glucose homeostasis (Figures 6J–6P and S7M). These results collectively demonstrate that Trp-CA-induced phosphorylation of ALDOA contributes to greater glycolysis and increased GLP-1 level, like the increase in GLP-1 induced by the Gs-cAMP pathway.

BSH/T of *B. animalis* subsp. *lactis* is responsible for the production of Trp-CA

To identify potential bacterial producers of Trp-CA, we screened 98 bacterial species from our lab that covered the main gut bacterial phyla. Among them, 4 *Bifidobacterium* species displayed strong Trp-CA production activity (Figure 7A). We further confirmed that Trp-CA production of 4 *Bifidobacterium* species in the time course and crude extracts of these bacteria could efficiently activate MRGPRE. Among these 4 *Bifidobacterium* species, *Bifidobacterium animalis* subsp. *lactis* (*B. animalis* subsp. *lactis*) showed the highest Trp-CA production (Figures 7B and 7C).

Recent studies illustrated a role of bacterial BSH/T by functioning as an amine N-acyl transferase that conjugates amines to form MABAs.[53,54] To test whether the BSH/T of *B. animalis* subsp. *lactis* (BAL BSH/T) was capable of Trp-CA production, we purified the BAL BSH/T (GenBank: AEN76601.1) to analyze its ability to synthesize Trp-CA (Figures 7D and S7N). We found that BAL BSH/T was indeed capable of catalyzing Trp-CA production (Figures 7E and 7F).

To verify the role of BAL BSH/T and *B. animalis* subsp. *lactis* in host glucose metabolism, BAL BSH/T was expressed in *E. coli* Nissle 1917 by genomic integration via CRISPR-Cas9.[55] Compared with control *E. coli*, *E. coli*-BAL BSH/T and *B. animalis* subsp. *lactis* colonization resulted in improved glucose tolerance and increased GLP-1 and insulin levels in HFD-fed mice (Figures 7G–7J and S7O). Our data showed that the 3 hydroxyl groups at positions C3, C7, and C12 of Trp-CA are indispensable for the activation of MRGPRE (Figures 4G and 4H); thus, we detected changes in the abundance of all MABAs with cholic acid as a backbone. These three increased MABAs failed to activate MRGPRE, which confirmed the benefits of Trp-CA (Figures S7P and S7Q). Furthermore, *B. animalis* subsp. *lactis* colonization improved glucose tolerance only in *Mrgpre*$^{fl/fl}$ mice but not in *Mrgpre*$^{\Delta IE}$ mice (Figures S7R–S7U).

Finally, to further explore human relevance and to further validate that the level of fecal Trp-CA was related to GLP-1 levels

(J) Blood glucose in OGTTs.
(K) AOC of OGTTs.
(L) Relative AOC of OGTTs.
(M–P) Serum active GLP-1 (M), relative active GLP-1 (N), insulin (O), and relative insulin (P) levels at 0 and 15 min after oral glucose gavage.
All data are presented as the means ± SEMs. n = 6 biological replicates for (A) and (E); n = 5 biological replicates for (B), (C), (G), and (H); and n = 4 biological replicates for (D) and (F). In (A), (C), and (D), the p values were determined by one-way ANOVA with Tukey's post hoc test. In (E), (F), (H), and (K)–(P), the p values were determined by two-way ANOVA with Tukey's post hoc test. In (J), the p values were determined by two-way repeated-measures ANOVA with LSD test. $^{*}p < 0.05$, $^{**}p < 0.01$, and $^{***}p < 0.001$ versus the control group.
See also Figure S7.

Please cite this article in press as: Lin et al., A microbial amino-acid-conjugated bile acid, tryptophan-cholic acid, improves glucose homeostasis via the orphan receptor MRGPRE, Cell (2025), https://doi.org/10.1016/j.cell.2025.05.010

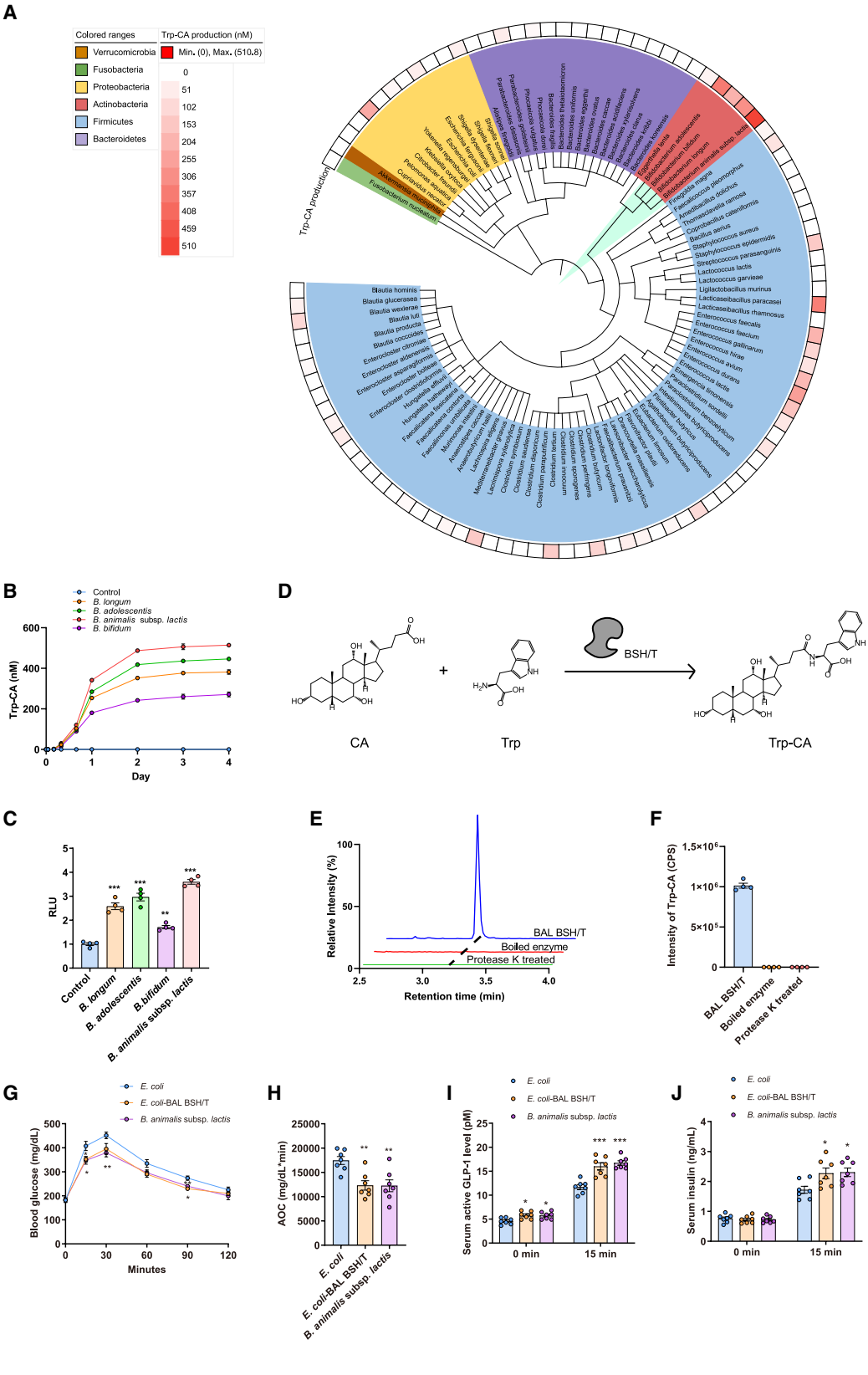

(legend on next page)

Please cite this article in press as: Lin et al., A microbial amino-acid-conjugated bile acid, tryptophan-cholic acid, improves glucose homeostasis via the orphan receptor MRGPRE, Cell (2025), https://doi.org/10.1016/j.cell.2025.05.010

and glucose homeostasis, we recruited a cohort of healthy individuals ($n = 21$) and patients with T2D ($n = 28$) (Table S3). The T2D group had lower fecal Trp-CA levels than the healthy controls (Figure S7V). We next correlated the Trp-CA levels with the GLP-1 levels and 120-min glucose levels during an OGTT in the entire cohort. We found that Trp-CA levels were positively correlated with the serum levels of GLP-1 at 120 min and inversely correlated with blood glucose levels at 120 min (Figures S7W and S7X).

DISCUSSION

Bile acids, synthesized from cholesterol in hepatocytes, are known for aiding lipid absorption and influencing host metabolism.[56] The physiological effects of newly discovered MABAs remain unclear. Our study reveals that Trp-CA, one of the MABAs, improves glucose tolerance in HFD-fed mice prior to obesity onset, acting independently of traditional bile acid receptors like FXR and TGR5.

Here, we found that Trp-CA is a ligand of the orphan receptor MRGPRE. Although MRGPRE belongs to the itch family receptors, we validated the physiological role of MRGPRE in promoting GLP-1 secretion. Obeticholic acid (OCA), a bile acid derivative, is approved as a second-line therapy for primary biliary cholangitis, but its dosage is limited by pruritus.[57] Trp-CA has poor oral absorption. At the dose used in our mouse studies (10 mg/kg), its serum levels remained below the threshold that elicits pruritus (data not shown).

Numerous studies have demonstrated that L cells, when stimulated by nutrients or metabolites, secrete GLP-1, which acts on GLP-1 receptors of intestinal vagal afferent nerves. This transmits neural signals through the central nervous system to vagal efferent nerves, thereby inhibiting hepatic gluconeogenesis.[58–60] In hyperinsulinemic-euglycemic clamp experiments, we found that both duodenal and colonic perfusion of Trp-CA significantly suppressed hepatic gluconeogenesis. Considering our series of experiments showing that Trp-CA stimulates GLP-1 secretion from L cells, and given the distribution of L cells throughout the small intestine and colon,[35] it is reasonable to hypothesize that the widespread gut enteric nervous system senses GLP-1 secretion to mediate the inhibition of hepatic gluconeogenesis induced by Trp-CA under conditions of suppressed endogenous insulin secretion.

In conclusion, our findings identify a distinctive receptor and its downstream signaling pathways for a specific MABA, namely, Trp-CA. And we show that MRGPRE could be an additional therapeutic target to treat glucose dysregulation in T2D. These results give impetus for the further study of other MABAs, including their roles in physiology and the receptors they bind, as well as their clinical relevance.

Limitations of the study

To elucidate Trp-CA's binding mode with hMRGPRE, we attempted to obtain the structure of the complex. Although the complex was formed *in vitro*, high-resolution cryo-EM imaging was hindered by receptor aggregation. Consequently, we modeled hMRGPRE based on the eqMRGPRE structure for Trp-CA docking and confirmed the binding site via mutagenesis of critical residues. This aligns with common structural biology practices, where homologous proteins are used when direct structural determination is challenging.[61–64] Further efforts to resolve the hMRGPRE structure are ongoing.

Notably, in the Trp-CA interaction model proposed in our study, three hydroxyl substituents on the steroidal nucleus form important hydrogen bonding interactions, which are very important and are responsible for inactivation of Trp-CDCA and Trp-DCA to MRGPRE. However, we cannot rule out the possibility of finding other bile acids that activate MRGPRE receptors in future studies.

L cells are the dominant cell type releasing GLP-1 in the intestine.[32] Therefore, we used intestine-specific knockout/knockdown to study how Trp-CA regulates GLP-1 secretion in L cells, which is a widely used approach in the field.[59,65,66] However, as our approach is not cell-type-specific, we cannot exclude whether Trp-CA acts on other cells as well, which is also a worthwhile follow-up study.

RESOURCE AVAILABILITY

Lead contact

Further information and requests for resources and reagents should be directed to the lead contact, Changtao Jiang (email: jiangchangtao@bjmu.edu.cn).

Materials availability

Materials in this work are available from the lead contact.

Figure 7. BSH/T of *B. animalis* subsp. *lactis* is responsible for the production of Trp-CA

(A) Phylogenetic tree of the 98 different gut bacteria species and the yield of Trp-CA. The phylogenetic tree was constructed using the 16S rRNA gene sequences by the maximum likelihood method. The tree was colored in terms of the phylum of each node; the outer heatmap displayed the Trp-CA production in the indicated species.

(B) Production of Trp-CA by different *Bifidobacterium* for the indicated times in days. $n = 3$ biological replicates.

(C) Activation fold of MRGPRE in the Tango system by crude extract of indicated bacteria.

(D) A schematic diagram illustrating that BSH/T can mediate the biosynthesis of Trp-CA from CA and Trp.

(E and F) Representative extracted ion chromatogram (E) and quantified production (F) of Trp-CA in enzymatic assays with BAL BSH/T under different conditions.

(G–J) HFD-fed SPF mice were treated with control *E. coli*, *E. coli*-BAL BSH/T, or *B. animalis* subsp. *lactis* one time per week for 2 weeks ($n = 7$ mice/group).

(G) Blood glucose in OGTTs.

(H) AOC of OGTTs.

(I and J) Serum active GLP-1 (I) and insulin (J) levels at 0 and 15 min after oral glucose gavage.

All data are presented as the means ± SEMs. $n = 4$ biological replicates for (C) and (F). In (C) and (H)–(J), the p values were determined by one-way ANOVA with Tukey's post hoc test. In (G), the p values were determined by two-way repeated-measures ANOVA with LSD test. $^{*}p < 0.05$, $^{**}p < 0.01$, and $^{***}p < 0.001$ versus the control group.

See also Figure S7.

Data and code availability

Non-targeted metabolome data for Trp-CA identification are available through NGDC (https://ngdc.cncb.ac.cn/) at NGDC: OMIX010009. Phosphoproteomics data and peptidomics data of mouse colonic tissues are available through NMDC (https://nmdc.cn/) at NMDC: NMDC10019848. The cryo-EM density map and atomic coordinates are available through Electron Microscopy Data Bank at EMDB: EMD-64464 and the Protein Data Bank at PDB: 9UST, respectively.

This paper does not report original code.

Any additional information required to reanalyze the data reported in this paper is available from the lead contact upon request.

ACKNOWLEDGMENTS

This work was supported by the National Natural Science Foundation of China (no. 92357305, 82130022, 82288102, and 82341226), the National Key Research and Development Program of China (no. 2022YFA0806400, 2024YFA1802100, and 2024YFA1803000), the National Natural Science Foundation of China (no. 82330118, 92149306, 82171627, 32271232, 82300890, and 82330022), the National Science Fund for Distinguished Young Scholars Grant (82225011), the Scientific Research Innovation Capability Support Project for Young Faculty (ZYGXQNJSKYCXNLZCXM-H2), and the Noncommunicable Chronic Diseases-National Science and Technology Major Project (2023ZD0506900). C.J. acknowledges support from the Tencent Foundation through the Xplorer Prize and from the Beijing Outstanding Young Scientist Program (no. JWZQ20240102003). J.-P.S. acknowledges support from the New Cornerstone Investigator Program and Extension Funding of the National Science Fund for Distinguished Young Scholars (no. 82425105). X.Y. acknowledges support from the Open Research Project in State Key Laboratory of Vascular Homeostasis and Remodeling (Peking University). The cryo-EM data were collected at the Center of Cryo Electron Microscopy, Shandong University. Cryo-EM specimens were screened at the Center of Cryo Electron Microscopy, Shandong University, with assistance from L. Qi, D. He, and M. Gu.

AUTHOR CONTRIBUTIONS

C.J. conceptualized, organized, and supervised the entire study. J.L., Q.N., J.C., Y.-N.Z., T.Z., Xiuying Zhang, X.G., Y.D., C.N., Y.G., K.W., M.G., X.W., W.C., C. Yun, C. Ye, J.X., W.S., L.Z., P.S., X.L., Z.Z., Xin Zheng, X.S., J.Z., S.N., Xuguang Zhang, F.R., and H.L. performed the experiments and analyzed the data. C.J. and Y.P. designed the studies to screen and identify Trp-CA; C.J. designed screening studies to find the Trp-CA bacterial producers and biosynthesis enzymes; C.J., Y.P., X.Y., and J.-P.S. designed and supervised the animal studies; J.-P.S. and C.J. designed the strategy to screen the receptor of Trp-CA; J.-P.S., X.Y., and C.J. designed the β-arrestin signaling studies and proposed the concept of regional signaling compartmentalization in intestinal L cells; J.-P.S. and E.D. designed molecular dynamics simulations and structural biology experiments. L.J. collected and provided clinical samples. J.L. and C.J. wrote the manuscript. J.L., Q.N., J.C., Y.-N.Z., T.Z., Xiuying Zhang, X.G., Y.D., and J.-P.S. revised the manuscript. J.L., Q.N., J.C., Y.-N.Z., T.Z., Xiuying Zhang, X.G., and Y.D. contributed equally to this work. All authors edited the manuscript and approved the final manuscript.

DECLARATION OF INTERESTS

C.J., X.Z., Y.P., K.W., and J.L. are named inventors on patents covering Trp-CA and bacterial producers for metabolic disorders.

STAR★METHODS

Detailed methods are provided in the online version of this paper and include the following:

SUPPLEMENTAL INFORMATION

Supplemental information can be found online at https://doi.org/10.1016/j.cell.2025.05.010.

Received: February 25, 2024
Revised: October 2, 2024
Accepted: May 8, 2025
Published: May 29, 2025

REFERENCES

1. Nauck, M.A., Wefers, J., and Meier, J.J. (2021). Treatment of type 2 diabetes: challenges, hopes, and anticipated successes. Lancet Diabetes Endocrinol. *9*, 525–544. https://doi.org/10.1016/S2213-8587(21)00113-3.
2. Perler, B.K., Friedman, E.S., and Wu, G.D. (2023). The Role of the Gut Microbiota in the Relationship Between Diet and Human Health. Annu. Rev. Physiol. *85*, 449–468. https://doi.org/10.1146/annurev-physiol-031522-092054.
3. Sorbara, M.T., and Pamer, E.G. (2022). Microbiome-based therapeutics. Nat. Rev. Microbiol. *20*, 365–380. https://doi.org/10.1038/s41579-021-00667-9.
4. Liu, S.M., Ifebi, B., Johnson, F., Xu, A., Ho, J., Yang, Y., Schwartz, G., Jo, Y.H., and Chua, S., Jr. (2023). The gut signals to AGRP-expressing cells of

the pituitary to control glucose homeostasis. J. Clin. Invest. *133*, e164185. https://doi.org/10.1172/JCI164185.

5. Wu, Q., Liang, X., Wang, K., Lin, J., Wang, X., Wang, P., Zhang, Y., Nie, Q., Liu, H., Zhang, Z., et al. (2021). Intestinal hypoxia-inducible factor 2alpha regulates lactate levels to shape the gut microbiome and alter thermogenesis. Cell Metab. *33*, 1988–2003.e7. https://doi.org/10.1016/j.cmet.2021.07.007.
6. Zheng, X., Chen, T., Jiang, R., Zhao, A., Wu, Q., Kuang, J., Sun, D., Ren, Z., Li, M., Zhao, M., et al. (2021). Hyocholic acid species improve glucose homeostasis through a distinct TGR5 and FXR signaling mechanism. Cell Metab. *33*, 791–803.e7. https://doi.org/10.1016/j.cmet.2020.11.017.
7. Sanyal, A.J., Ratziu, V., Loomba, R., Anstee, Q.M., Kowdley, K.V., Rinella, M.E., Sheikh, M.Y., Trotter, J.F., Knapple, W., Lawitz, E.J., et al. (2023). Results from a new efficacy and safety analysis of the REGENERATE trial of obeticholic acid for treatment of pre-cirrhotic fibrosis due to non-alcoholic steatohepatitis. J. Hepatol. *79*, 1110–1120. https://doi.org/10.1016/j.jhep.2023.07.014.
8. Fiorucci, S., Distrutti, E., Carino, A., Zampella, A., and Biagioli, M. (2021). Bile acids and their receptors in metabolic disorders. Prog. Lipid Res. *82*, 101094. https://doi.org/10.1016/j.plipres.2021.101094.
9. Solaas, K., Ulvestad, A., Söreide, O., and Kase, B.F. (2000). Subcellular organization of bile acid amidation in human liver: a key issue in regulating the biosynthesis of bile salts. J. Lipid Res. *41*, 1154–1162. https://doi.org/10.1016/S0022-2275(20)32022-8.
10. Quinn, R.A., Melnik, A.V., Vrbanac, A., Fu, T., Patras, K.A., Christy, M.P., Bodai, Z., Belda-Ferre, P., Tripathi, A., Chung, L.K., et al. (2020). Global chemical effects of the microbiome include new bile-acid conjugations. Nature *579*, 123–129. https://doi.org/10.1038/s41586-020-2047-9.
11. Lucas, L.N., Barrett, K., Kerby, R.L., Zhang, Q., Cattaneo, L.E., Stevenson, D., Rey, F.E., and Amador-Noguez, D. (2021). Dominant Bacterial Phyla from the Human Gut Show Widespread Ability To Transform and Conjugate Bile Acids. Published online August 31, 2021. mSystems, e0080521. https://doi.org/10.1128/mSystems.00805-21.
12. Shalon, D., Culver, R.N., Grembi, J.A., Folz, J., Treit, P.V., Shi, H., Rosenberger, F.A., Dethlefsen, L., Meng, X., Yaffe, E., et al. (2023). Profiling the human intestinal environment under physiological conditions. Nature *617*, 581–591. https://doi.org/10.1038/s41586-023-05989-7.
13. Gentry, E.C., Collins, S.L., Panitchpakdi, M., Belda-Ferre, P., Stewart, A.K., Carrillo Terrazas, M., Lu, H.H., Zuffa, S., Yan, T., Avila-Pacheco, J., et al. (2024). Reverse metabolomics for the discovery of chemical structures from humans. Nature *626*, 419–426. https://doi.org/10.1038/s41586-023-06906-8.
14. Ghislain, J., and Poitout, V. (2021). Targeting lipid GPCRs to treat type 2 diabetes mellitus - progress and challenges. Nat. Rev. Endocrinol. *17*, 162–175. https://doi.org/10.1038/s41574-020-00459-w.
15. Wacker, D., Stevens, R.C., and Roth, B.L. (2017). How Ligands Illuminate GPCR Molecular Pharmacology. Cell *170*, 414–427. https://doi.org/10.1016/j.cell.2017.07.009.
16. Cao, C., and Roth, B.L. (2023). The structure, function, and pharmacology of MRGPRs. Trends Pharmacol. Sci. *44*, 237–251. https://doi.org/10.1016/j.tips.2023.02.002.
17. Yang, F., Guo, L.L., Li, Y., Wang, G.P., Wang, J., Zhang, C., Fang, G.X., Chen, X., Liu, L., Yan, X., et al. (2021). Structure, function and pharmacology of human itch receptor complexes. Nature *600*, 164–169. https://doi.org/10.1038/s41586-021-04077-y.
18. Sun, L., Xie, C., Wang, G., Wu, Y., Wu, Q., Wang, X., Liu, J., Deng, Y., Xia, J., Chen, B., et al. (2018). Gut microbiota and intestinal FXR mediate the clinical benefits of metformin. Nat. Med. *24*, 1919–1929. https://doi.org/10.1038/s41591-018-0222-4.
19. Studer, E., Zhou, X., Zhao, R., Wang, Y., Takabe, K., Nagahashi, M., Pandak, W.M., Dent, P., Spiegel, S., Shi, R., et al. (2012). Conjugated bile acids activate the sphingosine-1-phosphate receptor 2 in primary rodent hepatocytes. Hepatology *55*, 267–276. https://doi.org/10.1002/hep.24681.
20. Gonzalez, F.J., Jiang, C., and Patterson, A.D. (2016). An Intestinal Microbiota-Farnesoid X Receptor Axis Modulates Metabolic Disease. Gastroenterology *151*, 845–859. https://doi.org/10.1053/j.gastro.2016.08.057.
21. Virtue, S., and Vidal-Puig, A. (2021). GTTs and ITTs in mice: simple tests, complex answers. Nat. Metab. *3*, 883–886. https://doi.org/10.1038/s42255-021-00414-7.
22. Zhang, S.Y., Li, R.J.W., Lim, Y.M., Batchuluun, B., Liu, H., Waise, T.M.Z., and Lam, T.K.T. (2021). FXR in the dorsal vagal complex is sufficient and necessary for upper small intestinal microbiome-mediated changes of TCDCA to alter insulin action in rats. Gut *70*, 1675–1683. https://doi.org/10.1136/gutjnl-2020-321757.
23. Bauer, P.V., Duca, F.A., Waise, T.M.Z., Dranse, H.J., Rasmussen, B.A., Puri, A., Rasti, M., O'Brien, C.A., and Lam, T.K.T. (2018). Lactobacillus gasseri in the Upper Small Intestine Impacts an ACSL3-Dependent Fatty Acid-Sensing Pathway Regulating Whole-Body Glucose Homeostasis. Cell Metab. *27*, 572–587.e6. https://doi.org/10.1016/j.cmet.2018.01.013.
24. Ma, L., Yang, F., Wu, X., Mao, C., Guo, L., Miao, T., Zang, S.K., Jiang, X., Shen, D.D., Wei, T., et al. (2022). Structural basis and molecular mechanism of biased GPBAR signaling in regulating NSCLC cell growth via YAP activity. Proc. Natl. Acad. Sci. USA *119*, e2117054119. https://doi.org/10.1073/pnas.2117054119.
25. Yang, F., Mao, C., Guo, L., Lin, J., Ming, Q., Xiao, P., Wu, X., Shen, Q., Guo, S., Shen, D.D., et al. (2020). Structural basis of GPBAR activation and bile acid recognition. Nature *587*, 499–504. https://doi.org/10.1038/s41586-020-2569-1.
26. Krasowski, M.D., Yasuda, K., Hagey, L.R., and Schuetz, E.G. (2005). Evolution of the pregnane x receptor: adaptation to cross-species differences in biliary bile salts. Mol. Endocrinol. *19*, 1720–1739. https://doi.org/10.1210/me.2004-0427.
27. Kroeze, W.K., Sassano, M.F., Huang, X.P., Lansu, K., McCorvy, J.D., Giguère, P.M., Sciaky, N., and Roth, B.L. (2015). PRESTO-Tango as an open-source resource for interrogation of the druggable human GPCRome. Nat. Struct. Mol. Biol. *22*, 362–369. https://doi.org/10.1038/nsmb.3014.
28. Bokoch, M.P., Zou, Y., Rasmussen, S.G.F., Liu, C.W., Nygaard, R., Rosenbaum, D.M., Fung, J.J., Choi, H.J., Thian, F.S., Kobilka, T.S., et al. (2010). Ligand-specific regulation of the extracellular surface of a G-protein-coupled receptor. Nature *463*, 108–112. https://doi.org/10.1038/nature08650.
29. Lin, H., Xiao, P., Bu, R.Q., Guo, S., Yang, Z., Yuan, D., Zhu, Z.L., Zhang, C.X., He, Q.T., Zhang, C., et al. (2022). Structures of the ADGRG2-G_s complex in apo and ligand-bound forms. Nat. Chem. Biol. *18*, 1196–1203. https://doi.org/10.1038/s41589-022-01084-6.
30. Xiao, P., Guo, S., Wen, X., He, Q.T., Lin, H., Huang, S.M., Gou, L., Zhang, C., Yang, Z., Zhong, Y.N., et al. (2022). Tethered peptide activation mechanism of the adhesion GPCRs ADGRG2 and ADGRG4. Nature *604*, 771–778. https://doi.org/10.1038/s41586-022-04590-8.
31. Ping, Y.Q., Mao, C., Xiao, P., Zhao, R.J., Jiang, Y., Yang, Z., An, W.T., Shen, D.D., Yang, F., Zhang, H., et al. (2021). Structures of the glucocorticoid-bound adhesion receptor GPR97-G_o complex. Nature *589*, 620–626. https://doi.org/10.1038/s41586-020-03083-w.
32. Sandoval, D.A., and D'Alessio, D.A. (2015). Physiology of proglucagon peptides: role of glucagon and GLP-1 in health and disease. Physiol. Rev. *95*, 513–548. https://doi.org/10.1152/physrev.00013.2014.
33. Breitman, I., Isbell, J.M., Saliba, J., Jabbour, K., Flynn, C.R., Marks-Shulman, P.A., Laferrère, B., Abumrad, N.N., and Tamboli, R.A. (2013). Effects of proximal gut bypass on glucose tolerance and insulin sensitivity in humans. Diabetes Care *36*, e57. https://doi.org/10.2337/dc12-1722.
34. Moo, E.V., van Senten, J.R., Bräuner-Osborne, H., and Møller, T.C. (2021). Arrestin-Dependent and -Independent Internalization of G Protein-Coupled Receptors: Methods, Mechanisms, and Implications on Cell Signaling. Mol. Pharmacol. *99*, 242–255. https://doi.org/10.1124/molpharm.120.000192.

35. Gribble, F.M., and Reimann, F. (2021). Metabolic Messengers: glucagon-like peptide 1. Nat. Metab. *3*, 142–148. https://doi.org/10.1038/s42255-020-00327-x.

36. Chen, H.W., Rosen, C.E., González-Hernández, J.A., Song, D.G., Potempa, J., Ring, A.M., and Palm, N.W. (2023). Highly multiplexed bioactivity screening reveals human and microbiota metabolome-GPCRome interactions. Cell *186*, 3095–3110.e19. https://doi.org/10.1016/j.cell.2023.05.024.

37. Liao, Y.Y., Zhang, H., Shen, Q., Cai, C., Ding, Y., Shen, D.D., Guo, J., Qin, J., Dong, Y., Zhang, Y., et al. (2023). Snapshot of the cannabinoid receptor 1-arrestin complex unravels the biased signaling mechanism. Cell *186*, 5784–5797.e17. https://doi.org/10.1016/j.cell.2023.11.017.

38. Liu, C.H., Gong, Z., Liang, Z.L., Liu, Z.X., Yang, F., Sun, Y.J., Ma, M.L., Wang, Y.J., Ji, C.R., Wang, Y.H., et al. (2017). Arrestin-biased AT1R agonism induces acute catecholamine secretion through TRPC3 coupling. Nat. Commun. *8*, 14335. https://doi.org/10.1038/ncomms14335.

39. He, Q.T., Xiao, P., Huang, S.M., Jia, Y.L., Zhu, Z.L., Lin, J.Y., Yang, F., Tao, X.N., Zhao, R.J., Gao, F.Y., et al. (2021). Structural studies of phosphorylation-dependent interactions between the V2R receptor and arrestin-2. Nat. Commun. *12*, 2396. https://doi.org/10.1038/s41467-021-22731-x.

40. Mao, C., Xiao, P., Tao, X.N., Qin, J., He, Q.T., Zhang, C., Guo, S.C., Du, Y. Q., Chen, L.N., Shen, D.D., et al. (2023). Unsaturated bond recognition leads to biased signal in a fatty acid receptor. Science *380*, eadd6220. https://doi.org/10.1126/science.add6220.

41. Shang, P., Rong, N., Jiang, J.J., Cheng, J., Zhang, M.H., Kang, D., Qi, L., Guo, L., Yang, G.M., Liu, Q., et al. (2023). Structural and signaling mechanisms of TAAR1 enabled preferential agonist design. Cell *186*, 5347–5362.e24. https://doi.org/10.1016/j.cell.2023.10.014.

42. Dong, J.H., Wang, Y.J., Cui, M., Wang, X.J., Zheng, W.S., Ma, M.L., Yang, F., He, D.F., Hu, Q.X., Zhang, D.L., et al. (2017). Adaptive Activation of a Stress Response Pathway Improves Learning and Memory Through Gs and beta-Arrestin-1-Regulated Lactate Metabolism. Biol. Psychiatry *81*, 654–670. https://doi.org/10.1016/j.biopsych.2016.09.025.

43. Smith, J.S., Lefkowitz, R.J., and Rajagopal, S. (2018). Biased signalling: from simple switches to allosteric microprocessors. Nat. Rev. Drug Discov. *17*, 243–260. https://doi.org/10.1038/nrd.2017.229.

44. Thomsen, A.R.B., Plouffe, B., Cahill, T.J., 3rd, Shukla, A.K., Tarrasch, J.T., Dosey, A.M., Kahsai, A.W., Strachan, R.T., Pani, B., Mahoney, J.P., et al. (2016). GPCR-G Protein-beta-Arrestin Super-Complex Mediates Sustained G Protein Signaling. Cell *166*, 907–919. https://doi.org/10.1016/j.cell.2016.07.004.

45. Rajagopal, S., Rajagopal, K., and Lefkowitz, R.J. (2010). Teaching old receptors new tricks: biasing seven-transmembrane receptors. Nat. Rev. Drug Discov. *9*, 373–386. https://doi.org/10.1038/nrd3024.

46. Cheng, J., Yang, Z., Ge, X.Y., Gao, M.X., Meng, R., Xu, X., Zhang, Y.Q., Li, R.Z., Lin, J.Y., Tian, Z.M., et al. (2022). Autonomous sensing of the insulin peptide by an olfactory G protein-coupled receptor modulates glucose metabolism. Cell Metab. *34*, 240–255.e10. https://doi.org/10.1016/j.cmet.2021.12.022.

47. Ko, M.J., Chiang, T., Mukadam, A.A., Mulia, G.E., Gutridge, A.M., Lin, A., Chester, J.A., and van Rijn, R.M. (2021). beta-Arrestin-dependent ERK signaling reduces anxiety-like and conditioned fear-related behaviors in mice. Sci. Signal. *14*, eaba0245. https://doi.org/10.1126/scisignal.aba0245.

48. Slosky, L.M., Bai, Y., Toth, K., Ray, C., Rochelle, L.K., Badea, A., Chandrasekhar, R., Pogorelov, V.M., Abraham, D.M., Atluri, N., et al. (2020). beta-Arrestin-Biased Allosteric Modulator of NTSR1 Selectively Attenuates Addictive Behaviors. Cell *181*, 1364–1379.e14. https://doi.org/10.1016/j.cell.2020.04.053.

49. Thomsen, A.R.B. (2023). GPCRs and β-arrestins — an on-off relationship. Cell Res. *33*, 819–820. https://doi.org/10.1038/s41422-023-00838-8.

50. Cahill, T.J., 3rd, Thomsen, A.R.B., Tarrasch, J.T., Plouffe, B., Nguyen, A. H., Yang, F., Huang, L.Y., Kahsai, A.W., Bassoni, D.L., Gavino, B.J., et al. (2017). Distinct conformations of GPCR-beta-arrestin complexes mediate desensitization, signaling, and endocytosis. Proc. Natl. Acad. Sci. USA *114*, 2562–2567. https://doi.org/10.1073/pnas.1701529114.

51. Trabelsi, M.S., Daoudi, M., Prawitt, J., Ducastel, S., Touche, V., Sayin, S.I., Perino, A., Brighton, C.A., Sebti, Y., Kluza, J., et al. (2015). Farnesoid X receptor inhibits glucagon-like peptide-1 production by enteroendocrine L cells. Nat. Commun. *6*, 7629. https://doi.org/10.1038/ncomms8629.

52. Reimann, F., Habib, A.M., Tolhurst, G., Parker, H.E., Rogers, G.J., and Gribble, F.M. (2008). Glucose sensing in L cells: a primary cell study. Cell Metab. *8*, 532–539. https://doi.org/10.1016/j.cmet.2008.11.002.

53. Guzior, D.V., Okros, M., Shivel, M., Armwald, B., Bridges, C., Fu, Y., Martin, C., Schilmiller, A.L., Miller, W.M., Ziegler, K.M., et al. (2024). Bile salt hydrolase acyltransferase activity expands bile acid diversity. Nature *626*, 852–858. https://doi.org/10.1038/s41586-024-07017-8.

54. Rimal, B., Collins, S.L., Tanes, C.E., Rocha, E.R., Granda, M.A., Solanki, S., Hoque, N.J., Gentry, E.C., Koo, I., Reilly, E.R., et al. (2024). Bile salt hydrolase catalyses formation of amine-conjugated bile acids. Nature *626*, 859–863. https://doi.org/10.1038/s41586-023-06990-w.

55. Jiang, Y., Chen, B., Duan, C., Sun, B., Yang, J., and Yang, S. (2015). Multigene editing in the Escherichia coli genome via the CRISPR-Cas9 system. Appl. Environ. Microbiol. *81*, 2506–2514. https://doi.org/10.1128/AEM.04023-14.

56. Ahmad, T.R., and Haeusler, R.A. (2019). Bile acids in glucose metabolism and insulin signalling - mechanisms and research needs. Nat. Rev. Endocrinol. *15*, 701–712. https://doi.org/10.1038/s41574-019-0266-7.

57. Nevens, F., Trauner, M., and Manns, M.P. (2023). Primary biliary cholangitis as a roadmap for the development of novel treatments for cholestatic liver diseases†. J. Hepatol. *78*, 430–441. https://doi.org/10.1016/j.jhep.2022.10.007.

58. Waise, T.M.Z., Dranse, H.J., and Lam, T.K.T. (2018). The metabolic role of vagal afferent innervation. Nat. Rev. Gastroenterol. Hepatol. *15*, 625–636. https://doi.org/10.1038/s41575-018-0062-1.

59. Bauer, P.V., Duca, F.A., Waise, T.M.Z., Rasmussen, B.A., Abraham, M.A., Dranse, H.J., Puri, A., O'Brien, C.A., and Lam, T.K.T. (2018). Metformin Alters Upper Small Intestinal Microbiota that Impact a Glucose-SGLT1-Sensing Glucoregulatory Pathway. Cell Metab. *27*, 101–117.e5. https://doi.org/10.1016/j.cmet.2017.09.019.

60. Duca, F.A., Côté, C.D., Rasmussen, B.A., Zadeh-Tahmasebi, M., Rutter, G.A., Filippi, B.M., and Lam, T.K.T. (2015). Metformin activates a duodenal Ampk-dependent pathway to lower hepatic glucose production in rats. Nat. Med. *21*, 506–511. https://doi.org/10.1038/nm.3787.

61. Wu, J., Yan, Z., Li, Z., Yan, C., Lu, S., Dong, M., and Yan, N. (2015). Structure of the voltage-gated calcium channel Cav1.1 complex. Science *350*, aad2395. https://doi.org/10.1126/science.aad2395.

62. Jeong, H., Clark, S., Goehring, A., Dehghani-Ghahnaviyeh, S., Rasouli, A., Tajkhorshid, E., and Gouaux, E. (2022). Structures of the TMC-1 complex illuminate mechanosensory transduction. Nature *610*, 796–803. https://doi.org/10.1038/s41586-022-05314-8.

63. Jasti, J., Furukawa, H., Gonzales, E.B., and Gouaux, E. (2007). Structure of acid-sensing ion channel 1 at 1.9 A resolution and low pH. Nature *449*, 316–323. https://doi.org/10.1038/nature06163.

64. Shen, H., Zhou, Q., Pan, X., Li, Z., Wu, J., and Yan, N. (2017). Structure of a eukaryotic voltage-gated sodium channel at near-atomic resolution. Science *355*, eaal4326. https://doi.org/10.1126/science.aal4326.

65. Li, R.J.W., Barros, D.R., Kuah, R., Lim, Y.M., Gao, A., Beaudry, J.L., Zhang, S.Y., and Lam, T.K.T. (2024). Small intestinal CaSR-dependent and CaSR-independent protein sensing regulates feeding and glucose tolerance in rats. Nat. Metab. *6*, 39–49. https://doi.org/10.1038/s42255-023-00942-4.

66. Yan, S., Conley, J.M., Reilly, A.M., Stull, N.D., Abhyankar, S.D., Ericsson, A.C., Kono, T., Molosh, A.I., Kubal, C.A., Evans-Molina, C., et al. (2022). Intestinal Gpr17 deficiency improves glucose metabolism by promoting

GLP-1 secretion. Cell Rep. *38*, 110179. https://doi.org/10.1016/j.celrep.2021.110179.

67. Pettersen, E.F., Goddard, T.D., Huang, C.C., Couch, G.S., Greenblatt, D. M., Meng, E.C., and Ferrin, T.E. (2004). UCSF Chimera—A visualization system for exploratory research and analysis. J. Comp. Chem. *25*, 1605–1612. https://doi.org/10.1002/jcc.20084.
68. Wang, K.Y., Gao, M.X., Qi, H.B., An, W.T., Lin, J.Y., Ning, S.L., Yang, F., Xiao, P., Cheng, J., Pan, W., et al. (2024). Differential contributions of G protein- or arrestin subtype-mediated signalling underlie urocortin 3-induced somatostatin secretion in pancreatic delta cells. Br. J. Pharmacol. *181*, 2600–2621. https://doi.org/10.1111/bph.16351.
69. Du, Y.Q., Sha, X.Y., Cheng, J., Wang, J., Lin, J.Y., An, W.T., Pan, W., Zhang, L.J., Tao, X.N., Xu, Y.F., et al. (2022). Endogenous Lipid-GPR120 Signaling Modulates Pancreatic Islet Homeostasis to Different Extents. Diabetes *71*, 1454–1471. https://doi.org/10.2337/db21-0794.
70. Abadpour, S., Tyrberg, B., Schive, S.W., Huldt, C.W., Gennemark, P., Ryberg, E., Rydén-Bergsten, T., Smith, D.M., Korsgren, O., Skrtic, S., et al. (2020). Inhibition of the prostaglandin D_2-GPR44/DP2 axis improves human islet survival and function. Diabetologia *63*, 1355–1367. https://doi.org/10.1007/s00125-020-05138-z.
71. Liu, C., Du, M.X., Abuduaini, R., Yu, H.Y., Li, D.H., Wang, Y.J., Zhou, N., Jiang, M.Z., Niu, P.X., Han, S.S., et al. (2021). Enlightening the taxonomy darkness of human gut microbiomes with a cultured biobank. Microbiome *9*, 119. https://doi.org/10.1186/s40168-021-01064-3.
72. Gomez-Mendoza, M., Marin, M.L., and Miranda, M.A. (2014). Two-channel dansyl/tryptophan emitters with a cholic acid bridge as reporters for local hydrophobicity within supramolecular systems based on bile salts. Org. Biomol. Chem. *12*, 8499–8504. https://doi.org/10.1039/c4ob01394h.
73. Hoki, J.S., Le, H.H., Mellott, K.E., Zhang, Y.K., Fox, B.W., Rodrigues, P.R., Yu, Y., Helf, M.J., Baccile, J.A., and Schroeder, F.C. (2020). Deep Interrogation of Metabolism Using a Pathway-Targeted Click-Chemistry Approach. J. Am. Chem. Soc. *142*, 18449–18459. https://doi.org/10.1021/jacs.0c06877.
74. Wang, M., Carver, J.J., Phelan, V.V., Sanchez, L.M., Garg, N., Peng, Y., Nguyen, D.D., Watrous, J., Kapono, C.A., Luzzatto-Knaan, T., et al. (2016). Sharing and community curation of mass spectrometry data with Global Natural Products Social Molecular Networking. Nat. Biotechnol. *34*, 828–837. https://doi.org/10.1038/nbt.3597.
75. Olsen, R.H.J., DiBerto, J.F., English, J.G., Glaudin, A.M., Krumm, B.E., Slocum, S.T., Che, T., Gavin, A.C., McCorvy, J.D., Roth, B.L., et al. (2020). TRUPATH, an open-source biosensor platform for interrogating the GPCR transducerome. Nat. Chem. Biol. *16*, 841–849. https://doi.org/10.1038/s41589-020-0535-8.
76. Guo, L., Cheng, J., Lian, S., Liu, Q., Lu, Y., Zheng, Y., Zhu, K., Zhang, M., Kong, Y., Zhang, C., et al. (2023). Structural basis of amine odorant perception by a mammal olfactory receptor. Nature *618*, 193–200. https://doi.org/10.1038/s41586-023-06106-4.
77. Yin, Y.L., Ye, C., Zhou, F., Wang, J., Yang, D., Yin, W., Wang, M.W., Xu, H. E., and Jiang, Y. (2021). Molecular basis for kinin selectivity and activation of the human bradykinin receptors. Nat. Struct. Mol. Biol. *28*, 755–761. https://doi.org/10.1038/s41594-021-00645-y.
78. Nehmé, R., Carpenter, B., Singhal, A., Strege, A., Edwards, P.C., White, C. F., Du, H., Grisshammer, R., and Tate, C.G. (2017). Mini-G proteins: Novel tools for studying GPCRs in their active conformation. PLoS One *12*, e0175642. https://doi.org/10.1371/journal.pone.0175642.
79. Liu, P., Jia, M.Z., Zhou, X.E., De Waal, P.W., Dickson, B.M., Liu, B., Hou, L., Yin, Y.T., Kang, Y.Y., Shi, Y., et al. (2016). The structural basis of the dominant negative phenotype of the Gαi1β1γ2 G203A/A326S heterotrimer. Acta Pharmacol. Sin. *37*, 1259–1272. https://doi.org/10.1038/aps.2016.69.
80. Zhao, L.H., Ma, S., Sutkeviciute, I., Shen, D.D., Zhou, X.E., de Waal, P.W., Li, C.Y., Kang, Y., Clark, L.J., Jean-Alphonse, F.G., et al. (2019). Structure and dynamics of the active human parathyroid hormone receptor-1. Science *364*, 148–153. https://doi.org/10.1126/science.aav7942.
81. Zheng, S.Q., Palovcak, E., Armache, J.P., Verba, K.A., Cheng, Y., and Agard, D.A. (2017). MotionCor2: anisotropic correction of beam-induced motion for improved cryo-electron microscopy. Nat. Methods *14*, 331–332. https://doi.org/10.1038/nmeth.4193.
82. Punjani, A., Rubinstein, J.L., Fleet, D.J., and Brubaker, M.A. (2017). cryoSPARC: algorithms for rapid unsupervised cryo-EM structure determination. Nat. Methods *14*, 290–296. https://doi.org/10.1038/nmeth.4169.
83. Emsley, P., and Cowtan, K. (2004). Coot: model-building tools for molecular graphics. Acta Crystallogr. D Biol. Crystallogr. *60*, 2126–2132. https://doi.org/10.1107/S0907444904019158.
84. Adams, P.D., Afonine, P.V., Bunkóczi, G., Chen, V.B., Davis, I.W., Echols, N., Headd, J.J., Hung, L.-W., Kapral, G.J., Grosse-Kunstleve, R.W., et al. (2010). PHENIX: a comprehensive Python-based system for macromolecular structure solution. Acta Crystallogr. D Biol. Crystallogr. *66*, 213–221. https://doi.org/10.1107/S0907444909052925.
85. Waterhouse, A., Bertoni, M., Bienert, S., Studer, G., Tauriello, G., Gumienny, R., Heer, F.T., de Beer, T.A.P., Rempfer, C., Bordoli, L., et al. (2018). SWISS-MODEL: homology modelling of protein structures and complexes. Nucleic Acids Res. *46*, W296–W303. https://doi.org/10.1093/nar/gky427.
86. Halgren, T.A. (2009). Identifying and Characterizing Binding Sites and Assessing Druggability. J. Chem. Inf. Model. *49*, 377–389. https://doi.org/10.1021/ci800324m.
87. Friesner, R.A., Murphy, R.B., Repasky, M.P., Frye, L.L., Greenwood, J.R., Halgren, T.A., Sanschagrin, P.C., and Mainz, D.T. (2006). Extra precision glide: Docking and scoring incorporating a model of hydrophobic enclosure for protein-ligand complexes. J. Med. Chem. *49*, 6177–6196. https://doi.org/10.1021/jm051256o.
88. Halgren, T.A., Murphy, R.B., Friesner, R.A., Beard, H.S., Frye, L.L., Pollard, W.T., and Banks, J.L. (2004). Glide: A new approach for rapid, accurate docking and scoring. 2. Enrichment factors in database screening. J. Med. Chem. *47*, 1750–1759. https://doi.org/10.1021/jm030644s.
89. Friesner, R.A., Banks, J.L., Murphy, R.B., Halgren, T.A., Klicic, J.J., Mainz, D.T., Repasky, M.P., Knoll, E.H., Shelley, M., Perry, J.K., et al. (2004). Glide: A new approach for rapid, accurate docking and scoring. 1. Method and assessment of docking accuracy. J. Med. Chem. *47*, 1739–1749. https://doi.org/10.1021/jm0306430.
90. Jorgensen, W.L., Maxwell, D.S., and Tirado-Rives, J. (1996). Development and testing of the OPLS all-atom force field on conformational energetics and properties of organic liquids. J. Am. Chem. Soc. *118*, 11225–11236. https://doi.org/10.1021/ja9621760.
91. Lee, J., Cheng, X., Swails, J.M., Yeom, M.S., Eastman, P.K., Lemkul, J.A., Wei, S., Buckner, J., Jeong, J.C., Qi, Y.F., et al. (2016). CHARMM-GUI Input Generator for NAMD, GROMACS, AMBER, OpenMM, and CHARMM/OpenMM Simulations Using the CHARMM36 Additive Force Field. J. Chem. Theory Comput. *12*, 405–413. https://doi.org/10.1021/acs.jctc.5b00935.
92. Van der Spoel, D., Lindahl, E., Hess, B., Groenhof, G., Mark, A.E., and Berendsen, H.J.C. (2005). GROMACS: Fast, flexible, and free. J. Comput. Chem. *26*, 1701–1718. https://doi.org/10.1002/jcc.20291.
93. Huang, J., Rauscher, S., Nawrocki, G., Ran, T., Feig, M., de Groot, B.L., Grubmüller, H., and MacKerell, A.D. (2017). CHARMM36m: an improved force field for folded and intrinsically disordered proteins. Nat. Methods *14*, 71–73. https://doi.org/10.1038/Nmeth.4067.
94. Zhang, Y., Wang, X., Lin, J., Liu, J., Wang, K., Nie, Q., Ye, C., Sun, L., Ma, Y., Qu, R., et al. (2024). A microbial metabolite inhibits the HIF-2alpha-ceramide pathway to mediate the beneficial effects of time-restricted feeding on MASH. Cell Metab. *36*, 1823–1838.e6. https://doi.org/10.1016/j.cmet.2024.07.004.
95. Ren, L., Li, C., Shao, W., Lin, W., He, F., and Jiang, Y. (2018). TiO_2 with Tandem Fractionation (TAFT): An Approach for Rapid, Deep, Reproducible, and High-Throughput Phosphoproteome Analysis. J. Proteome Res. *17*, 710–721. https://doi.org/10.1021/acs.jproteome.7b00520.

96. Sun, Y., Zhou, Y., Shi, Y., Zhang, Y., Liu, K., Liang, R., Sun, P., Chang, X., Tang, W., Zhang, Y., et al. (2021). Expression of miRNA-29 in Pancreatic β Cells Promotes Inflammation and Diabetes via TRAF3. Cell Rep. *34*, 108576. https://doi.org/10.1016/j.celrep.2020.108576.

97. Huang, Q., Gong, Q., Wen, T., Feng, S., Xu, J., Liu, J., Han, X., Liu, Q., Hu, J., and Zhu, L. (2020). Loss of LAMTOR1 in pancreatic β-cells increases glucose-stimulated insulin secretion in mice. Int. J. Mol. Med. *45*, 23–32. https://doi.org/10.3892/ijmm.2019.4409.

98. Li, E., Shan, H., Chen, L., Long, A., Zhang, Y., Liu, Y., Jia, L., Wei, F., Han, J., Li, T., et al. (2019). OLFR734 Mediates Glucose Metabolism as a Receptor of Asprosin. Cell Metab. *30*, 319–328.e8. https://doi.org/10.1016/j.cmet.2019.05.022.

99. Li, N., Yang, Z., Li, Q., Yu, Z., Chen, X., Li, J.C., Li, B., Ning, S.L., Cui, M., Sun, J.P., et al. (2018). Ablation of somatostatin cells leads to impaired pancreatic islet function and neonatal death in rodents. Cell Death Dis. *9*, 682. https://doi.org/10.1038/s41419-018-0741-4.

Please cite this article in press as: Lin et al., A microbial amino-acid-conjugated bile acid, tryptophan-cholic acid, improves glucose homeostasis via the orphan receptor MRGPRE, Cell (2025), https://doi.org/10.1016/j.cell.2025.05.010

STAR★METHODS

KEY RESOURCES TABLE

REAGENT or RESOURCE	SOURCE	IDENTIFIER
Chemicals and proteins		
Ampicillin	Sigma-Aldrich	Cat#BP021
Kanamycin	Sigma-Aldrich	Cat#D403
Metronidazole	Sigma-Aldrich	Cat#M1547
Vancomycin	Sigma-Aldrich	Cat#V2002
Gentamicin sulfate	Sigma-Aldrich	Cat#E003632
Methanol	Sigma-Aldrich	Cat#439193
Acetonitrile	Sigma-Aldrich	Cat#34851
Formic acid	Sigma-Aldrich	Cat#F0507
EtOAc	Beijing FreeMore bioscience	Cat#E116131
FITC-dextran (4 kDa)	Aladdin	Cat#F491425
Cholic acid	Aladdin	Cat#C103690
Deoxycholic acid	Aladdin	Cat#D103697
Chenodeoxycholic acid	Aladdin	Cat#C104902
Lithocholic acid	Aladdin	Cat#L106779
Sodium taurocholate hydrate	Aladdin	Cat#T134625
Glycocholic acid	Aladdin	Cat#G131002
Ursodeoxycholic acid	Aladdin	Cat#U110695
Tauroursodeoxycholic acid	Aladdin	Cat#T614340
Tauro-β-muricholic acid	MedChemExpress	HY-N9933
Calcitriol	MedChemExpress	HY-10002
Rifampicin	MedChemExpress	HY-B0272
MABAs (Arg-CA, Asp-CA, Asn-CA, etc)	This study	N/A
Critical commercial assays		
Aldolase Activity Assay Kit	Abcam	Cat#ab196994
ATP detection kit	Beyotime	Cat#S0027
Active GIP Elisa kit	Crystal Chem	Cat#81511
Active GLP-1 Elisa kit	Milipore	Cat#EZGLPHS-35K
Mouse insulin ELISA kit	Cusabio	Cat#CSB-E05071
Mouse C-peptide ELISA kit	Cloud-Clone Corp	Cat#CEA447Mu
MultiF Seamless Assembly Mix	Abclonal	Cat#RK21020
2 × Phanta Flash Master Mix (Dye Plus)	Vazyme	Cat#P520-01
FastPure Gel DNA Extraction Mini Kit	Vazyme	Cat#DC301-01
Lipofectamine 3000 transfection reagent	ThermoFisher Scientific	Cat#L3000015
Lipofectamine LTX transfection reagent	ThermoFisher Scientific	Cat#15338500
GloSensor™ cAMP Assay	Promega	Cat#E1291
Bright-Glo™ Luciferase Assay System	Promega	Cat#E2620
Dual-luciferase assay system	Promega	Cat#E1910
Biological samples and strains		
E. coli BL21 (DE3)	Thermo Scientific	Cat#EC0114
E. coli DH5α	Thermo Scientific	Cat#EC0112
B. animalis subsp. *lactis* JC24-02	Lab stock	N/A
E. coli Nissle 1917	Lab stock	N/A

(*Continued on next page*)

Please cite this article in press as: Lin et al., A microbial amino-acid-conjugated bile acid, tryptophan-cholic acid, improves glucose homeostasis via the orphan receptor MRGPRE, Cell (2025), https://doi.org/10.1016/j.cell.2025.05.010

Continued

REAGENT or RESOURCE	SOURCE	IDENTIFIER
Oligonucleotides		
siRNA used in this study	This study	Table S4
Primers used in this study	This study	Table S5
Recombinant DNA and plasmids		
pET-28a	Lab stock	N/A
PGL4-Shp-TK firefly luciferase construct	Lab stock	N/A
Human FXR expression plasmid	Lab stock	N/A
Human ASBT expression plasmid	Lab stock	N/A
Human VDR expression plasmid	Lab stock	N/A
Human PXR expression plasmid	Lab stock	N/A
pCMVSPORT6/hTGR5	Lab stock	N/A
cAMP response element-driven luciferase reporter plasmids	Lab stock	N/A
Renilla luciferase control vector	Lab stock	N/A
Human/Mouse/Equus quagga MRGPRE expression plasmid	This study	N/A
Mouse ALDOA WT/S39A/S39E expression plasmid	This study	N/A
PRESTO-Tango Kit	Addgene	Kit #1000000068
Human β-arrestin-1 expression plasmid	This study	N/A
Deposited data		
Public transcriptomic data of various tissues	Thorrez L	GEO: GSE46843
Transciptome data from cells sorted from different hormone reporter mouse organoid lines	Beumer J	GEO: GSE114988
Mouse enteroendocrine transcriptome	Gribble FM	GEO: GSE114913
2-MOA–eqMRGPRE–Gq	PDB protein bank (www.rscb.org/)	PDB: 9UST
Non-targeted metabolome data for Trp-CA identification	NGDC (https://ngdc.cncb.ac.cn/)	OMIX010009
Phosphoproteomic data of GLUTag cells	NMDC (https://nmdc.cn/)	NMDC10019848
Phosphoproteomic data of intestinal epithelium	NMDC (https://nmdc.cn/)	NMDC10019848
Peptidomics data of colon tissues	NMDC (https://nmdc.cn/)	NMDC10019848
Experimental models: Cell lines		
HEK293T	Lab stock	N/A
GLUTag	D. J. Drucker	University of Toronto
STC-1	Wei Jia	Shanghai Jiao Tong University
NCI-H716	Wei Jia	Shanghai Jiao Tong University
HTLA	Yi Rao	Capital Medical University
Experimental models: Mouse strains		
C57BL/6J	GemPharmatech	N/A
Mrgpre-/-	GemPharmatech	N/A
Mrpgre$^{flox/flox}$	GemPharmatech	N/A
Arrb1$^{-/-}$ / *Arrb2*$^{-/-}$	Duke University	Prof. RJ Lefkowitz
Gnas$^{fl/fl}$	Cyagen Suzhou	N/A
Actb-tdTomato/EGFP	The Jackson Laboratory	RRID:IMSR_JAX:007576
Villin/*Gcg*-Cre	GemPharmatech	N/A
Software and algorithms		
GraphPad Prism version 8.0	GraphPad	www.graphpad.com
Mega 7	Mega	http://www.megasoftware.net/
SPSS 27.0	SPSS	N/A

(*Continued on next page*)

Please cite this article in press as: Lin et al., A microbial amino-acid-conjugated bile acid, tryptophan-cholic acid, improves glucose homeostasis via the orphan receptor MRGPRE, Cell (2025), https://doi.org/10.1016/j.cell.2025.05.010

Continued

REAGENT or RESOURCE	SOURCE	IDENTIFIER
SnapGene Viewer	SnapGene	http://www.snapgene.com/products/snapgene_viewer/
Gromacs version 2019.6	Gromacs Software	https://www.gromacs.org/
UCSF Chimera	Pettersen et al.[67]	https://www.cgl.ucsf.edu/chimera/
UCSF ChimeraX	Pettersen et al.[67]	https://www.cgl.ucsf.edu/chimerax
Blast	NCBI	https://blast.ncbi.nlm.nih.gov/Blast.cgi
Other		
GAM broth, modified	Solarbio	Cat#LA4490
BHI medium	Solarbio	Cat#B8130
TSB medium	Solarbio	Cat#RL100111
MRGPRE antibody	LS bio	Cat#LS-C136078 RRID:AB_10913437
GLP-1 antibody	abcam	Cat#ab26278 RRID:AB_470838
Mouse anti DDDDK-Tag mAb	ABclonal	Cat# AE005; RRID: AB_2770401
ACTB Monoclonal Antibody	ABclonal	Cat# AC026; RRID: AB_2768234
Aldolase antibody	abcam	Cat#ab252953; RRID:AB_3099487
Tryptone	Oxoid	Cat#LP0042
ACQUITY UPLC CSH C18 column	Waters	Cat#186005297

EXPERIMENTAL MODEL AND STUDY PARTICIPANT DETAILS

Human study participants

The human study was approved by the Ethical Committee of the Peking University People's Hospital [2023PHB331-001] and informed written consent was obtained from all participants. Clinical parameters were determined at the Peking University People's Hospital. Individuals with fasting blood glucose $\geq$ 7.0 mmol/L and/or a %Hb1c $\geq$ 6.5 were classified as having type 2 diabetes (T2D). All the patients with T2D were drug treatment naive. The exclusion criteria were: type 1 diabetes, pregnancy, severe diabetic complications (diabetic retinopathy, diabetic neuropathy, diabetic nephropathy and diabetic foot); severe hepatic diseases including chronic persistent hepatitis, liver cirrhosis or the co-occurrence of positive hepatitis and abnormal hepatic transaminase; severe organic disease, including cancer, coronary heart disease, renal disease, thyroid disease, myocardial infarction or cerebral apoplexy; infectious disease; alcoholism; continuous antibiotic use for over 3 days within 3 months prior to enrollment; and continuous medication (including weight loss or psychotropic medication) for over 3 days prior to enrollment. One group of 80 individuals including 40 healthy controls (16 men and 24 women), and 40 patients with T2D (21 men and 19 women) were recruited for this study (the clinical indices are shown in Table S1). Another group of 49 individuals that underwent OGTTs, including 21 healthy controls (9 men and 12 women), and 28 patients with T2D (11 men and 17 women) were recruited for this study (the clinical indices are shown in Table S3). Stool samples were collected in collection cups and immediately frozen at -80°C until analysis.

Mice and treatments

All animal protocols were approved by the Animal Care and Use Committee of Peking University (permit: PUIRB-LA2023297). C57BL/6J mice, *Mrgpre*-/- mice, *Mrpgre*$^{fl/fl}$ mice, and *Villin/Gcg*-Cre mice were purchased from the GemPharmatech (Jiangsu, China). *Actb-tdTomato*/EGFP mice was purchased from The Jackson Laboratory. *Gnas*$^{fl/fl}$ mice (stock number S-CKO-02679) was purchased from Cyagen (Suzhou, China).[68] *Arrb1*$^{-/-}$ and *Arrb2*$^{-/-}$ mice were obtained from Prof. RJ Lefkowitz (Duke University, Durham, NC).[38,42,46,68,69] All mice (8-week-old) had free access to food and water under a strict 12-h light/dark cycle at a controlled temperature (23°C $\pm$ 2°C). All mice were randomly assigned to experimental groups, and the groups did not present differences in body weights before the treatments. Mice were euthanized by CO_2 asphyxiation, and no mice were excluded from the analysis.

To explore the effect of Trp-CA on glucose metabolism, 8-week-old C57BL/6J male SPF mice were fed 8 weeks of an HFD (D12492, Research Diets). Mice were treated with vehicle or 10 mg/kg Trp-CA by oral gavage 3 times per week. Mice were monitored for body weight, food intake, oral glucose tests (OGTTs), and insulin tolerance tests (ITTs) were performed after 2 weeks (to rule out secondary effects of weight loss) or 8 weeks of an HFD. The OGTTs were also performed in *Mrgpre*$^{-/-}$, *Mrgpre*$^{\Delta IE}$, *Gnas*^{iKO}, sh*Aldoa*, *Arrb1*$^{-/-}$, and *Arrb2*$^{-/-}$ mice after 2 weeks of HFD feeding.

To explore the effect of *B. animalis* subsp. *lactis* and *E. coli*-BAL BSH/T on glucose tolerance, 8-week-old C57BL/6J male mice were fed an HFD for 2 weeks. Mice were treated with 2 $\times$ 10^8 CFUs of control *E. coli*, *E. coli*-BAL BSH/T and *B. animalis* subsp. *lactis* in 200 μL of sterile anaerobic PBS once per week.

To investigate the role of *B. animalis* subsp. *lactis* on the production of Trp-CA, 8-week-old C57BL/6J SPF were treated with 2×10^8 CFUs of *B. animalis* subsp. *lactis* in 200 μL of sterile anaerobic PBS by gavage once and last for one week, feces were collected for MABAs detection.

OGTTs were performed in mice after a 6-hour fast. The glucose levels of tail vein blood samples were measured using a glucose analyzer (accu-chek, Roche, USA) at 0, 15, 30, 60, 90 and 120 min after oral administration of glucose (2 g/kg). For the IVGTTs, the glucose levels of tail vein blood samples were measured using a glucose analyzer at 0, 5, 15, 30, 45, 60, and 90 min after intravenous injection of glucose (1 g/kg).[70] For the ITT, insulin (1 U/kg) was administered via intraperitoneal injection after a 6-hour fast. The glucose levels of tail vein blood samples were measured at 0, 15, 30, 60, and 90 min after insulin load. For measurement of active GLP-1 and insulin, blood was mixed with 10% Dpp4 inhibitors (vol/vol) (1 μM sitagliptin and 0.1 nM diprotin A) and serum was isolated after centrifugation (3,000 rpm, 15 min, 4°C) and stored at -80°C until further analysis.

Bacteria

The bacteria strains were from our lab stock, which were isolated from human stool samples, as previously described.[71] The phylogenies of all the cultured isolates were determined by BLAST analysis of the 16S rRNA gene sequences against the NCBI 16S rRNA sequence database. Before administration by oral gavage, the bacterial solutions were diluted with anaerobic PBS to a final concentration of 2×10^8 CFU/0.2 mL. For the screen of Trp-CA-producing bacteria, the BHI medium (contain 100 μM CA and 100 μM tryptophan) was inoculated with different strains, the supernatant was harvested after 48 h incubation, which was further processed for LC-MS/MS analysis. High Trp-CA production bacteria list (more than 200 nM): *Bifidobacterium adolescentis* JC24-02, *Bifidobacterium bifidum* JC24-01, *Bifidobacterium animalis* subsp. *lactis* MN-Gup and JC24-02, *Bifidobacterium longum* B79 and BBMN68, *Citrobacter freundii* JC24-03, *Enterococcus avium* JC24-01, *Lacticaseibacillus paracasei* LC-19.

Cell culture

The GLUTag cell line was a gift from D. J. Drucker, University of Toronto. STC-1 cells and the NCI-H716 cells were obtained from Wei Jia, Shanghai Jiao Tong University Affiliated Sixth People's Hospital. The GLUTag cells and STC-1 cells were cultured in Dulbecco's modified Eagle's medium (DMEM) containing 10% FBS and 1% penicillin-streptomycin at 37°C under 5% CO_2。 The NCI-H716 was cultured in RPMI 1640 supplemented with 10% FBS and 1% penicillin–streptomycin at 37°C under 5% CO_2. For the GLP-1-secretion assay, the cells were cultured in collagen-coated 24-well plates overnight. On the day of treatment, the cells were starved in HBSS containing 0.2% BSA for 2 h and then treated with Trp-CA for 1 h. The cell supernatants were then collected for the measurement of GLP-1 concentration. For gene-knockdown experiments, target-specific siRNAs against *Mrgpre* or *Aldoa* or *Arrb1* or *Arrb2* and a scramble control (siCtrl) were transfected into GLUTag cells using Lipofectamine RNAiMAX (Invitrogen). The list of siRNA sequences was shown in Table S4.

METHOD DETAILS

Synthesis of Trp-CA

N,N-(3-dimethylaminopropyl)-N′-ethylcarbodiimide (EDC, 477 μL, 2.69 mmol) and cholic acid (1.0 g, 2.45 mmol) in anhydrous CH_2Cl_2 (20 mL) was cooled to 0°C under an inert atmosphere. Then, a solution containing L-tryptophan methyl ester hydrochloride (L-TrpMe·HCl, 935 mg, 3.67 mmol), N,N-diisopropyl-N-ethylammine (DIEA, 600 μL, 3.67 mmol) and 4-pyrrolidylpyridine (4-Pr-Py, 180 mg, 1.22 mmol) in anhydrous CH_2Cl_2 (30 mL) was added dropwise, and the reaction mixture was stirred overnight at room temperature. Afterwards, it was poured into water and extracted with CH_2Cl_2. The combined organic layers were washed with brine, dried over $MgSO_4$ and concentrated. Purification by column chromatography gave TrpMe-CA. A solution of TrpMe-CA (150 mg, 0.25 mmol) in MeOH (3 mL) was treated with methanolic KOH (1 mol, 2 mL) and stirred overnight at room temperature. Afterward, the solvent was evaporated and re-dissolved in H_2O and acidified with 1 M HCl. The mixture was extracted with AcOEt and then removed by vacuum. Trp-CA was obtained as a white solid after purification by column chromatography.[72]

Bacteria abundance

For detecting bacteria abundance, DNA was extracted from mouse fecal pellets using a CTAB-based DNA extraction protocol. For each sample, the fecal pellet was resuspended in 600 μL CTAB lysis buffer, and then the samples were lysed using a tissue laser. The tubes were then vortexed and then incubated for 1 h at 65°C. Seven hundred microliters of chloroform-isoamyl alcohol (24:1) was added to each tube, and the tubes were vortexed and then centrifuged at 13,000 rpm for 15 min at room temperature. 500 μL of supernatant was transferred to a 1.5 mL tube, 330 μL isopropanol was added and inverted gently to mix. The genomic DNA was precipitated at 12,000 × *g* for 2 min in a microcentrifuge. The DNA pellet was washed with 400 μL 70% ethanol twice and then subjected to dried vacuum centrifugation, upon which it was resuspended in 50 μL nuclease-free water. The genomic DNA of *E. coli* and *Bifidobacterium animalis* subsp. *lactis* was extracted to establish a standard curve by RT-qPCR. KAPA SYBR FAST qPCR Kit was used for the reactions (2 × KAPA SYBR FAST qPCR Master Mix: 10 μL, 10 μM forward/reverse Primer: 0.4 μL, Template gDNA: 1 μL, Water to 20 μL). Reaction conditions were conducted at 95°C for 3 min followed by 40 cycles of [95°C for 3 s, 60°C for 20 s, 72°C for 20 s]. This was followed by one cycle of 65°C for 5 s and 95°C for holding to calculate the disassociation curves. Different concentration of gDNA

was used as the template to get a corresponding Ct value with *Bifidobacterium animalis* subsp. *lactis* 16s rRNA or *E. coli uidA* primers (Table S5).

Mass spectrometric analysis

High resolution LC-MS analysis was performed on a Vanquish UHPLC coupled with a Thermo Q-Exactive HF high-resolution mass spectrometer equipped with a HESI ion source. Chromatographic separation was employed with an ACQUITY UPLC CSH C18 column (2.1 × 100 mm, 1.7 μm, Waters) at 40°C and a flow rate of 0.3 mL/min. The solvent A is 0.1% formic acid in water, and the solvent B is 0.1% formic acid in ACN. Samples were eluted using a linear gradient: 0-5 min, 10% B; 5-20 min, 10-100% B; 20-25 min, 100% B; 25-30 min, 100-10% B. Mass spectrometer parameters were: spray voltage 3.0 kV, capillary temperature 380°C, auxiliary gas heater temperature 400°C; sheath, auxiliary, and spare gas flow was 60, 20, and 1, respectively; S-lens RF level 50. MS1 data was collected in both positive and negative modes. Resolution was set at 240,000, and the scan range was set to *m/z* 100-1,000. The detailed instrument parameter setting referred to the description of Hoki et al.[73]

Molecular networking

To identify the key metabolites that associated with T2D, molecular networking of GNPS was performed.[74] Each LC-MS RAW files (Thermo Fisher) was converted to mzXML format using MSConvert (ProteoWizard), the mzXML files were uploaded to the UCSD MassIVE data storage server through WinSCP for GNPS analysis. Molecular networks were created using the online workflow at GNPS and visualized in Cytoscape. The molecular networking and MS-cluster parameters were as follows: parent and fragment ion mass tolerance 0.02 Da, minimum cosine score of 0.7, minimum matched fragment ions of 4, and a minimum cluster size of 4 (to minimize detection of more rare nodes found in few samples).

Synthetic procedures of amino acid-conjugated bile acids

Synthesis of the conjugated bile acids was adapted from a previous method.[10,13] Cholic acid (100 mg, 0.25 mmol) was dissolved in anhydrous tetrahydrofuran (THF, 4.9 mL, 0.05 mol) and cooled to 0°C with stirring. Ethyl chloroformate (28 μL) and trimethylamine (41 μL) were added sequentially, and the reaction was stirred for 1.5 h at 0°C. After complete conversion of starting material by TLC, a cold solution (4.9 mL) of different amino acid (0.37 mmol) and inorganic base ($NaHCO_3$ or NaOH, 0.37 mmol) was added in one portion. Then, the reaction was stirred for 2 h at 0°C to completion and gradually warmed to room temperature. After that point, THF was removed under reduced pressure, and 2 M HCl was added to acidify the reaction mixture to pH < 2, producing a white precipitate. The mixture was extracted in ethyl acetate (3 × 20 mL), then the combined organic lavers were washed with brine (50 mL) dried over $NaSO_4$ and concentrated *in vacuo*. Different amino acid-conjugated bile acids were obtained as a white solid after purification by column chromatography separately.

Quantification of amino acid-conjugated bile acids

Quantification of different amino acid-conjugated bile acids was performed by a liquid chromatography-tandem mass spectrometry (LC-MS/MS) system that composed of a Acquity Ultra-Performance Liquid Chromatography (UPLC) system (Waters Corporation, Milford, USA) coupled to a Sciex 5500 triple quadrupole linear ion trap mass spectrometer (AB SCIEX, Framingham, MA, USA.). Chromatographic separation was employed with an ACQUITY UPLC CSH C18 column (2.1 × 100 mm, 1.7 μm, Waters) at 40°C and a flow rate of 0.25 mL/min. The injection volume was 5 μL, Mobile phase A was 0.1% FA in water and mobile phase B was 0.1% FA in acetonitrile. All analytes were detected in negative ion multiple reaction monitoring (MRM) mode. Chromatographic separation was performed using a linear gradient as follows: 0-1 min, 40% B; 1-6 min, 40-100% B; 6-7 min, 100% B; 7-8 min, 100-40% B. The detailed MRM parameters was listed in Table S6. The standard curves with internal calibration were constructed using mixed working standard solutions with gradient dilution (0.1, 1, 10, 100, 1,000 nM), CA-d4 (0.2 μM) was used as internal standard for each concentration. Operational control of the LC-MS/MS was performed with Analyst version 1.6.2, and quantitative analysis was performed using MultiQuant software (version 3.0.1).

For the quantification of bile acids from intestine, intestinal contents and feces (lyophilized), accurately weighed samples (20 mg) were placed in a tube and 400 μL of ice-cold methanol containing 0.2 μM internal standards was added. The samples were thoroughly homogenized with a tissue homogenizer. Samples subsequently underwent ultrasonic extraction for 20 min for metabolites extraction. All samples were subsequently centrifuged at 14,000 rpm for 20 min at 4°C. The supernatant was filtered through a membrane filter (pore size, 0.22 μm) for LC-MS/MS analysis.

For the quantification of bile acids from serum or culture supernatant from bacteria, samples were diluted with ice-cold methanol (1:4) containing 0.2 μM internal standards (CA-d4). Then the samples were vortexed for 10 min and were incubated at -20°C for 1 h. All samples were subsequently centrifuged at 14,000 rpm for 20 min at 4°C. The supernatant was filtered through a membrane filter (pore size, 0.22 μm) for LC-MS/MS analysis.

Stability of Trp-CA

Stool-derived *ex vivo* communities in mGAM (10 mL) was added with 20 μM Trp-CA before incubation, and GCA was used as control. Then the two bile acids were incubated for continuous 2 day, and samples were collected every 6 h. The level of Trp-CA at different time points was analyzed by LC-MS/MS.

Receptor luciferase assay

After 24 h post-transfection, the cells were then exposed for 8 h to Trp-CA and agonists as positive control at the concentration of 10 μM for the TGR5, FXR, PXR and VDR test. Luciferase assays were performed using the dual-luciferase assay system (Promega). Firefly and Renilla luciferase activities were measured using a Centro microplate illuminometer (Berthold technology).

Tango GPCR screening system

HTLA cells, a HEK293T cell line that stably expresses β-arrestin-TEV and tTA-Luciferase (a kind gift from Yi Rao, Capital Medical University), were plated in 96-well tissue culture plates (Corning) in DMEM containing 10% FBS and 1% Penicillin/Streptomycin. One day after plating (after reaching approximately 90% confluence), 200 ng per well GPCR-Tango plasmids[27] in 200 μL DMEM were mixed with 400 ng polyethylenimine (Polysciences) in an equal volume of DMEM and incubated for 20 min at room temperature before adding the transfection mixture to the HTLA cells. 16-24 h after transfection, medium was replaced with indicated dose of Trp-CA or other metabolites. Supernatants were aspirated 16-24 h after stimulation and 50 μL per well of Bright-Glo solution (Promega) was added into each well. After 20 min incubation at room temperature, luminescence was quantified using a Centro microplate illuminometer (Berthold technology). Activation fold for each sample was calculated by dividing relative luminescence units (RLU) for each condition by RLUs from media alone controls.

G protein dissociation assay

The gene of one hundred of the most highly expressed GPCRs in the intestine were cloned into pcDNA3.1 with an N-terminal HA signal sequence and a FLAG tag for Gα-Gγ dissociation assays in HEK293T cells. G protein bioluminescence resonance energy transfer (BRET) probes including Gα-RLuc8 (Gαi-RLuc8, Gαq-RLuc8, Gαs-RLuc8), Gβ3, and Gγ9-GFP2 were generated according to previously described.[17,46,75] HEK293T cells were transiently co-transfected with these GPCRs and G protein BRET probes. 48 h after transfection, cells were distributed into 96-well microplates at a density of 5×10^4 cells per well. The cells were washed twice with Tyrode's buffer (140 mM NaCl, 2.7 mM KCl, 1mM $CaCl_2$, 12 mM $NaHCO_3$, 5.6 mM D-glucose, 0.5 mM $MgCl_2$, 0.37 mM NaH_2PO_4 and 25 mM HEPES, pH 7.4) as previously published and stimulated with Trp-CA, Trp-CDCA and Trp-DCA at indicated concentrations as specified in the text or Figure legends. BRET signal was measured after the addition of the luciferase substrate coelenterazine 400a (5 μM) using a Mithras LB940 microplate reader equipped with BRET filter sets. The BRET signal was calculated as the ratio of light emission at 510 nm/400 nm.

β-arrestin recruitment assay

HEK293T cells were transiently co-transfected with β-arrestin-1-Rluc or β-arrestin-2-Rluc and YFP-tagged receptor (MRGPRE WT) as previously described.[25,46] Twenty-four hours after transfection, the cells were distributed into 96-well microplates at a density of 5×10^4 cells per well. After another twenty-four hours incubation at 37°C, the cells were washed twice with Tyrode's buffer (140 mM NaCl, 2.7 mM KCl, 1 mM $CaCl_2$, 12 mM $NaHCO_3$, 5.6 mM D-glucose, 0.5 mM $MgCl_2$, 0.37 mM NaH_2PO_4 and 25 mM HEPES, pH 7.4) and stimulated for 10 min with Trp-CA at indicated concentrations as specified in the text or Figure legends. Luciferase substrate coelenterazine-h (5 μM) was added before light emissions were recorded using a Mithras LB940 microplate reader (Berthold Technologies) with BRET filter sets. The BRET signal was determined by calculating the ratio of luminescence at 530 nm/485 nm.

FlAsH-BRET assay

The FlAsH BRET assay was performed to monitor the extracellular conformational changes of hMRGPRE, mMRGPRE or eqMRGPRE as previously described.[17,28,31] HEK293T cells grown in six-well plates which transiently transfected with Nluc-MRGPRE with FlAsH sequences (-CCPGCC-) inserted at various extracellular loop regions respectively defined as S1 to S5 for hMRGPRE or S1 to S6 for mMRGPRE (Figures S3C and S3H) were incubated for 48 h at 37°C and 5% CO_2. Then the transfected cells were washed and incubated with 2.5 μM FlAsH-EDT2 at 37°C in 5% CO_2 for 40 min. Afterwards, cells were washed three times with BRET buffer (25 mM HEPES, pH 7.0, 1 mM $CaCl_2$, 140 mM NaCl, 2.7 mM KCl, 0.9 mM $MgCl_2$, 0.37 mM NaH_2PO_4, 5.5 mM D-glucose and 12 mM $NaHCO_3$) and re-suspended in 1 mL of BRET buffer and seeded into white-wall clear-bottom 96-well plates. Luciferase substrate coelenterazine H at a final concentration of 5 μM was added with increasing concentrations of Trp-CA and the readings were started immediately. The BRET signals between Nluc (440–480 nm) and the FlAsH fluorescent moiety (525–585 nm) emissions were determined using the Mithras LB 940 Multimode Microplate Reader.

Enzyme-linked immunosorbent assay

To evaluate cell surface expression of the MRGPRE wild-type, mutations, and Nluc-MRGPRE with FlAsH sequences (-CCPGCC-) inserted at various extracellular loop regions respectively defined as S1 to S5 for hMRGPRE; S1 to S6 for mMRGPRE (Figures S3I and S3L), HEK293T cells were transfected the plasmid of MRGPRE, and the FlAsH-BRET sensors using Lipofectamine 2000 (Thermo Fisher Scientific) as previously described.[17,25] 24 h post transfection, cells were divided into 24-well plates at a density of 2×10^5 cells per well and further incubated for 24 h at 37°C in 5% CO_2. The cells were washed three times with PBS, then fixed by 4% (w/v) paraformaldehyde for 5 min at 4°C, blocked with 5% (w/v) BSA for another 1 h. Further, the cells were washed and incubated with the mouse monoclonal anti-FLAG M2 primary antibody (Sigma-Aldrich, Cat# F1804, 1:1000) at 4°C for 1 h and incubated with secondary goat anti-mouse antibody (Thermo Fisher, Cat# A-21235, 1:5000) for 1 h at room temperature. After washing, TMB

(3,3',5,5'-tetramethylbenzidine) solution was added for color reaction, which was then stopped by adding an equal volume of 0.25 M HCl. The absorbance at 450 nm was determined using a TECAN luminescence counter (Infinite M200 Pro NanoQuant). The expression levels of the MRGPRE and the FlAsH-BRET sensors (Nluc-MRGPRE with FlAsH sequences (-CCPGCC-) inserted at various extracellular loop regions were normalized to that of the WT MRGPRE.

Protein structure related constructs

The hMRGPRE and eqMRGPRE receptors were cloned into a pFastBac vector containing an N-terminal bovine prolactin signal peptide followed by a FLAG epitope (DYKDDDDK). To facilitate expression and purification, a BRIL epitope was inserted to the N-terminal of MRGPRE.

As previously reported,[76] the Gαs used was a modified Gαs chimera, which was generated on the basis of the mini-Gs scaffold with replacement of the N terminus of Gs (residue 1 to residue 25) with Gαi1 (residue 1 to residue 18), providing possible binding sites for antibody fragments scFv16. In addition, the GGSGGSGG linker at the position of original Gs α-helical domain (V65-L203) was replaced by with that of human Gi1 (G60-K180). As previously reported,[41,77] the engineered $G\alpha_q q$ construct was generated based on mini-Gs/q_{71}[78] with two dominant-negative mutations (corresponding to G203A and A326S)[79] to decrease the affinity of nucleotide binding. The N-terminal (residue 1 to residue 18) and the α-helical domain of the mini-Gs/q_{71} were replaced by the corresponding sequences of the human Gαi1 to facilitate the binding of scFv16.

Protein structure related expression and purification

To stabilize the complex of hMRGPRE–Gs and eqMRGPRE–Gq, the modified Gαs (mGαs) chimera and the modified Gαq (miniGαq) were used, then complex was efficiently assembled on the membrane by co-expressing receptor with mGαs or miniGαq, Gβ1, Gγ2 and scFv16 subunits. Sf9 cells (Expression Systems) were grown in ESF 921 medium to a density of 2.5×10^6 cell/mL and then were co-infected with four separate baculoviruses (Bac-to-Bac Baculovirus system, Invitrogen) at a ratio of 2:1:1:1 for hMRGPRE, mGαs (a modified Gαs),[80] Gβ1γ2 and scFv16, respectively. Or co-infected with four separate baculoviruses (Bac-to-Bac Baculovirus system, Invitrogen) at a ratio of 2:1:1:1 for eqMRGPRE, miniGαq,[41,77] Gβ1γ2 and scFv16, respectively. 48 h post-infection, the cells were harvested by centrifugation and cell pellets were stored at -80°C.

Cell pellets were resuspended in 20 mM HEPES pH 7.5, 100 mM NaCl, 3mM $MgCl_2$ and 5 mM $CaCl_2$ supplemented with cOmplete Protease Inhibitor Cocktail tablets (Roche). Complex formation was initiated by addition of 20 μM Trp-CA or 20 μM 2-MOA, and apyrase (25 mU/mL, NEB). The suspension was incubated for 1 h at room temperature and then solubilized by 0.5% (w/v) lauryl maltose neopentyl glycol (LMNG; Anatrace) supplemented with 0.05% (w/v) cholesteryl hemisuccinate (CHS; Anatrace) for 2 h. Insoluble material was removed by centrifugation at 65,000 x g for 30 min and the solubilized complex was immobilized by batch binding to M1 anti-Flag affinity resin. The resin was packed into a glass column and washed with 30 column volumes of 20 mM HEPES pH 7.5, 100 mM NaCl, 3 mM $MgCl_2$, 5 mM $CaCl_2$, 20 μM Trp-CA or 20 μM 2-MOA, 0.01% (w/v) LMNG and 0.001% (w/v) CHS before bound material was eluted in buffer containing 10 mM EGTA and 0.2 mg/mL FLAG peptide. The complex was concentrated using an Amicon Ultra Centrifugal Filter (MWCO, 100 kDa) and subjected to size-exclusion chromatography on a Superose 6 Increase 10/300 column (GE Healthcare) that was pre-equilibrated with 20 mM HEPES pH7.5, 100 mM NaCl, 20 μM Trp-CA or 20 μM 2-MOA, 0.00075% (w/v) MNG, 0.00025% (w/v) glyco-diosgenin (GDN; Anatrace) and 0.0001% (w/v) CHS to separate complex from contaminants. Eluted fractions that consisted of receptor and G protein complex were pooled and concentrated.

Cryo-EM sample preparation and data acquisition

For cryo-EM grids preparation of the Trp-CA–hMRGPRE–Gs and 2-MOA–eqMRGPRE–Gq complexes, 3 μL of the purified complexes at ~8 mg/mL were applied onto glow-discharged holey carbon grids (Quantifoil, Au300 R1.2/1.3). Grids were plunge-frozen in liquid ethane using Vitrobot Mark IV (Thermo Fischer Scientific). Cryo-EM imaging was performed on a Titan Krios electron microscope at 300 kV accelerating voltage using a Gatan K3 Summit direct electron detector with an energy filter. Micrographs were collected with a nominal magnification of 81,000× using the EPU software in super-resolution mode at a calibrated pixel size of 1.06 Å and a defocus range of -1 to -2 μm. Each stack was acquired with an exposure time of 3.5 s and dose-fractionated to 32 frames with a total dose of 60 $e^-Å^{-2}$. A total of 3,500 movies and 6,271 movies were collected for Trp-CA–hMRGPRE–Gs and 2-MOA–eqMRGPRE–Gq complexes, respectively.

Cryo-EM data processing

Image stacks were subjected to beam-induced motion correction using MotionCor2.[81] Contrast transfer function (CTF) parameters were estimated from motion-corrected images using patch CTF estimation in cryoSPARC depending on its image processing software.[82]

For 2-MOA–eqMRGPRE–Gq complex, 6,271 movie stacks were imported in cryoSPARC v4.2, subjected to Patch motion correction (multi) followed by CTF estimation with Patch CTF estimation (multi). Motion corrected micrographs with CTF fit resolution better than 4 Å were selected for further processing. Each micrograph was manually inspected to take away bad pictures that were contaminated by crystalline ice or other visible contamination. Particles were autopicked by a Blob-picker module within the cryoSPARC 4.2 and extracted with a box size of 256 pixels and fourier cropped to 128 pixels for 2D classification. Clean particles with different orientations of the complex from three rounds of 2D classification were re-extracted with a box size of 128 pixels and fourier cropped

to 256 pixels. For purpose of better particle-picking, a conventional neural network-based method Topaz implemented in cryoSPARC, was used for particle picking. Total 2,050,394 particles were extracted with 256 pixels binned to 128 pixels from the dataset and subjected to 2D classification. A clean particle stack of 552,239 from the 2D classification step was selected and re-extracted with a box size of 256 pixels. This clean particle stack was subjected to ab-initio reconstruction and heterogeneous refinement with C1 symmetry served as 3D Classification. And then the best particles stacks were classed by Class3D focused on eqMRGPRE. Then 64,460 particle projections of the best class were further applied for homogenous refinement and non-uniform refinement with C1 symmetry, generating the best density map with global resolution of 3.02 Å. To improve the quality of eqMRGPRE receptor density map, a soft mask was applied to the receptor for density subtraction, and further refinement led to a 2.48 Å map for the receptor mask.

For Trp-CA–hMRGPRE–Gs complex, with the same steps mentioned above, a sum of 3,500 movie stacks were imported in cryoSPARC v4.2, but a well-defined subset was unable to be selected.

Model building and structure refinement

The coordinates of eqMRGPRE from AlphaFold2 was used as the initial model. The Gq heterotrimer (Gαq, Gβ1 and Gγ2) and scFv16 were generated using the HT2A–miniGq–scFv16 complex (PDB: 6WHA) as the initial model. After model fitted into the EM density map by UCSF Chimera,[67] coordinates were manual adjusted and rebuilt in COOT.[83] Then the coordinates were refined by using Phenix.[84] Residues or side chains could not be fitted with unambiguous EM density were not included in the final model. Structural figures were prepared in PyMoL, UCSF Chimera and UCSF ChimeraX. The extent of model overfitting was evaluated by refining the final model against one half-map. FSC curves were calculated between the resulting model and the half map as well as between the resulting model and the other half map for cross-validation.

Homology modelling and binding pockets analysis

The initial models of hMRGPRE were generated with the online homology modelling server SWISS-MODEL[85] using the eqMRGPRE–Gq complex as a template. The corresponding binding pockets were analyzed through the 'SiteMap' algorithm.[86] All atoms in hMRGPRE structures were considered as the receptors. The grid spacing was set to 0.7 Å, and points that bordered on too many assigned philic points were excluded. Each pocket required at least 15 site points, and the top 5 potential binding pockets were identified and analyzed.

Molecule docking

The GLIDE program (version 5.6, Schrödinger, LLC, New York, NY, 2010)[87,88] was used for docking studies. Prior to docking, ligands were prepared using ''Ligand Prep'' module. For GLIDE docking, complex structures of hMRGPRE were preprocessed according to the protein preparation procedure recommended and docking site was defined in terms of ligands. All docking calculations were run in the ''Standard Precision'' (SP) mode[89] with default values for all parameters. Five poses per prepared ligand were saved for each docking calculation. The best-docked structure was chosen using the Glide Score.[90]

Molecular dynamics (MD) simulation

We analyzed the molecular docking results of Trp-CA with hMRGPRE, the conformation with the lowest binding energy was selected for the next molecular dynamics (MD) simulation. All the MD simulation input files of Trp-CA with hMRGPRE complex were generated by the CHARMM-GUI website.[91] We embedded the hMRGPRE–Trp-CA complex into the double-layer POPC membrane, adding with 0.15 M NaCl to balance the system charge, and incorporation the ions into the system using the Monte Carlo method. The TIP3P model was used for hexagonal type water box. The steepest descent method was used to minimize the Trp-CA with hMRGPRE complex simulation system with a series of restraints for the hMRGPRE, Trp-CA and lipid atoms to ensure that the energy of the entire system converges to 500 kJ/(mol·nm). The simulation system was heated from 0 K to 310 K in the NVT ensemble (number of particles, volume and temperature are conserved) for 1,000 ps. Following this, the NPT ensemble simulations were run at 1 atm for 1,000 ps with 10.0 kcal mol 1 Å 2 harmonic restraints. The 500-ns MD simulation was carried out by Gromacs2019.5[92] with a Charmm36m all-atom force field.[93] In the MD simulation, the LINCS algorithm was used to constrain all the bonds involving hydrogen. The cutoff value for nonbonding interactions was 12 Å. A time step of 2 fs was used, and the trajectories were saved every 10 ps.

To study the stability of ligand–receptor–G protein complex binding, we extracted the receptor region of the hMRGPRE model generated using SWISS-MODEL and the Gs region of the ADGRG2–Gs complex (PDB:7XKE), and the hMRGPRE–Gs complex model for MD simulations was generated by Chimera. All the MD input files were generated, and all these MD simulation systems are executed using the molecular dynamics simulation parameters set at the beginning.

Immunofluorescence staining

For immunofluorescence staining, mice were treated as described above. 2 cm of ileum and colon was taken, the intestinal lumen was flushed with a gavage needle, fixed with 4% PFA, cryoprotected with 30% sucrose (w/v PBS), and sectioned (10 μm) for staining. Immunohistochemistry staining of GLUTag cells, mouse ileum and colon sections were performed by using antibodies for MRGPRE (LS-C136078; LS bio), EEA1 (ab2900, abcam), and GLP-1 (ab26278; abcam).

Please cite this article in press as: Lin et al., A microbial amino-acid-conjugated bile acid, tryptophan-cholic acid, improves glucose homeostasis via the orphan receptor MRGPRE, Cell (2025), https://doi.org/10.1016/j.cell.2025.05.010

FACS of L cells

The whole colon and the last quarter of the small intestine from *Gcg*-Cre;*Actb*-tdTomato/EGFP reporter mice were isolated and rinsed in cold PBS. Intestine epithelium tissues were collected by scraping and resuspended in TrypLE Express (Thermo Fisher Scientific, Waltham, MA) at 37 °C for 20 min to dissociate into single cell suspension. Cells were re-suspended in 1 mL 1 × PBS containing 1% BSA and 10 mM Y27632 (STEMCELL Technologies, Cambridge, MA). EGFP positive cells with a fluorescence signal measured above 10^3 were gated to collect the Gcg positive (i.e. GLP-1-producing) cells. We collected the EGFP-positive (GCG^+), and EGFP-negative (GCG^-) live cells for RNA extraction with RNeasy Kits (QIAGEN).

Assessment of cellular metabolism

Cellular respiration of HEK293T cells or GLUTag cells was measured by a Seahorse XF24 analyzer (Seahorse Bioscience, North Billerica, MA). 1×10^5 cells/well were seeded in Seahorse XF24-well culture plates in growth medium and incubated at 37°C / 5% CO_2 overnight. Cells were changed to the XF Glycolysis Stress Test Assay Medium and placed in a 37 °C non-CO_2 incubator for 1 h prior to the assay after they were washed two times with the same assay medium. An assay template was created on the XF Controller and allowed to calibrate and equilibrate, which consisted of 3-minute mix, 2-minute wait, and 3-minute measure cycles. Three basal rate measurements were conducted prior to the first injection, and then glucose (10 mM), oligomycin (1 mM), and 2-deoxy-d-glucose (2-DG, 100 mM) were injected into each well at the indicated time. After injection, the oxygen consumption rate and extracellular acidification rate were closely monitored until the rates stabilized, and then the experiment was terminated. After each measurement, the living cell number of each well was calculated using a BioTek cytation5 (Agilent, USA) after Hochest/PI double staining for further normalization.

Aldolase activity and cellular ATP detection

The aldolase activity was measured using the Aldolase Activity Assay Kit (Colorimetric) (ab196994, Abcam). Cellular ATP was detected by using ATP detection kit (Beyotime).

Surgical procedures for intestinal-specific knockdown mice

To generate $Gnas^{iKO}$ mice, $Gnas^{fl/fl}$ mice received an intestinal adenovirus overexpress cre recombinase injection to the ileum and colon as previously described.[94] Briefly, the intestinal segment between ileum and colon was elevated and ligated with vascular clamps at both ends to block distribution of virus and intestinal fluids. The intestinal portion was cut with a longitudinal 3 mm incision, then flushed with saline by an insulin needle inserting right below the 6 cm ligation, and 0.3 mL adenovirus (purchased from HanBio, Shanghai) expressing pAdEasy-CMV or pAdEasy-CMV-CRE (both at 1.0×10^{10} PFU/mL; 30 μL adenovirus was diluted with saline into a total volume of 300 μL for injection) was administrated via an insulin needle. 20 min later, vascular clamps were removed, and the intestine was flushed with 200 μL saline. After that, the incision was sutured with 10-0 suture. To generate Sh*Aldoa* mice or scramble mice, C57BL/6J mice received an intestinal-lentivirus (purchased from HanBio, Shanghai) overexpress ShRNA (pHBLV-U6-sh*Aldoa*-MCS-CMV-ZsGreen-PGK-PURO or pHBLV-U6-MCS-CMV-ZsGreen-PGK-PURO) injection to the ileum and colon. Verified siRNA sequence 5′-CCAAGTGGCGCTGTGTGCT-3′ (#1) and 5′-GCCATGGGCCTTGACTTTC-3′ (#2) were designed for Sh*Aldoa* vector construct.

Phylogenetic Analyses

The phylogenetic tree of stool isolates was calculated by maximum likelihood method using IQ-TREE software, with the 16S sequences of the stool isolates. The diagram was visualized using iTOL.

Expression and purification of BAL BSH/T

The gene for *B. animalis* subsp. *lactis* BSH/T (AEN76601.1, codon-optimized) cloned into pET-28a was synthesized by Synbiob. The construct was transformed into *E. coli* BL21 (DE3) cells and induced with 0.2 mM isopropyl-β-d-thiogalactoside (IPTG) for 16 h at 24°C. The cultured cells were harvested by centrifugation and re-suspended in PBS buffer. To prepare the supernatant fraction, cells in PBS buffer was broken by ultrasonic and centrifuged at 12,000 rpm for 20 min at 4°C. Recombinant protein in the supernatant was purified with HisTrap FF affinity chromatography and then was eluted with PBS buffer containing 1 M imidazole and final kept in cleaning PBS buffer through dialysis.

Activity assay of BAL BSH/T

In catalytic activity assays of BAL BSH/T, 2 μg purified enzyme was added to 100 μL reaction mixture which contained 50 mM phosphate buffer (pH 7.0) and required substrates (CA, tryptophan) and incubated at 37°C for 1 h. The reactions were quenched with the addition of 300 μL ice-cold methanol (1:4) containing 0.2 μM internal standards (CA-d4). The samples were vortexed for 10 min and were incubated at -20°C for 1 h. All samples were subsequently centrifuged at 14,000 rpm for 20 min at 4°C. The supernatant was filtered through a membrane filter (pore size, 0.22 μm) for LC-MS/MS analysis. All substrates mentioned above was applied at the final concentration of 2 mM in the reaction mixture. Besides, corresponding negative controls were undergone in the same conditions except for boiled or proteinase K treated protein. All samples were prepared in triplicate for analysis.

Please cite this article in press as: Lin et al., A microbial amino-acid-conjugated bile acid, tryptophan-cholic acid, improves glucose homeostasis via the orphan receptor MRGPRE, Cell (2025), https://doi.org/10.1016/j.cell.2025.05.010

Real-time quantitative PCR

Total RNA from tissues and cells was isolated with TRIzol™ Reagent (Thermo Fisher Scientific, USA) and reverse-transcribed with high-capacity cDNA reverse transcription kit. The relative expression of genes was detected by real-time fluorescence quantitative polymerase chain reaction (Light Cycler 480, Roche, Sweden) with SYBR Green Master Mix (Promega, USA). The list of primers was shown in Table S5.

Peptidomics

The mouse colon tissues were cut into small pieces, according to 1g: 3 mL 100 mM Tris-HCl (pH = 7.5), heating and boiling for 10 min. The samples were then added the steel ball and kept 50 Hz high-frequency oscillation in 4 °C tissue grinder for 10 min. To denature and precipitate proteins, the samples were further added final concentration of 1 M glacial acetic acid, vortex shaking for 2 min. After adding an equal volume of acetonitrile, the samples were vortexed for 2 min. Proteins were then further precipitated using 80% acetone. The samples were then centrifuged at 12,000 × *g* for 10 min at 4°C, supernatant was transfer to a clean tube for next freeze drying. After drying, samples were added 200 μL of 0.1% TFA solution to re-dissolve and desalted with C18 column. Lumos reversed-phase chromatography fusion was used for protein analysis.

Phosphoproteomics

Phosphoproteomics were performed as previously reported.[95] Briefly, intestinal epithelium or GLUTag cells was added to an appropriate amount of lysis buffer (including 4% SDS, 0.1 M Tris/HCl and 0.1 M DDT, pH 7.6) containing protease inhibitors and phosphatase inhibitors, and vortexed for 30 s. The samples were then ultrasonicated for 60 s (3 s on and 2 s off for one cycle), with an amplitude of 25%. After standing at room temperature for 30 min, and centrifugation at 15,000 rpm and 4°C for 10 min, the supernatant was carefully removed and centrifuged again. The protein concentration was measured using BCA protein quantitative assay. Phosphopeptides were enriched using titanium dioxide (TiO_2). TiO_2 beads in tubes and TiO_2 microcolumns packed on centrifugation adaptors (GL Sciences, 5010–21514) were individually equilibrated with 100 μL of loading buffer (70% ACN, 5% TFA and 20% lactic acid (Sigma-Aldrich, L6661)). After centrifugation, supernatants containing TiO_2 beads were removed. Peptides from all 6 subfractions in each experiment were diluted in 100 μL of loading buffer, mixed thoroughly with 5 mg of TiO_2 beads, and incubated for 30 min. The mixtures of TiO_2 beads and peptides were then centrifuged at 800 × *g* for 5 min, the supernatants were transferred into new clear tubes for a second round of phosphopeptide enrichment, and the enriched TiO_2 beads were suspended in 100 μL of loading buffer, transferred into microcolumns and then packed into centrifugation adaptors. Each column with enriched TiO_2 beads was washed four times with 120 μL of loading buffer (150 × *g*, 10 min), washed once with 100 μL of washing buffer 1 (30% ACN and 0.5% TFA) (250 × *g*, 8 min) and wash twice with washing buffer 2 (0.4% TFA and 80% ACN) (250 × *g*, 5 min). Phosphopeptides were eluted with 150 μL of elution buffer (15% NH_4OH (Wako, 013–23355), 40% ACN), and the first and second phosphopeptides enriched in each subfraction were combined, dried in a SpeedVac and stored at -80°C. Lumos reversed- phase chromatography fusion was used for protein analysis. The volcano map was performed using the OmicStudio tools at https://www.omicstudio.cn/tool.

Western blot analysis

Tissue and cell extracts were homogenized in ice-cold RIPA buffer with protease and phosphatase inhibitors and resolved on 8%-10% SDS–polyacrylamide gels and transferred to a PVDF membrane. After blocking with 5% nonfat milk, the PVDF membrane was incubated with the desired primary antibody (diluted in TBST supplemented with 5% BSA and 0.01% (m/v) NaN_3) overnight at 4°C on an orbital shaker with gentle shaking, followed by rinsing with TBST 3 times, 8 min each at room temperature, and then the secondary antibodies were incubated for 2 h at room temperatures with gentle shaking. The secondary antibody (diluted in TBST supplemented with 5% BSA) was then removed, and the PVDF membrane was further washed with TBST 3 times, 8 min each at room temperature.

Surgical procedures for clamp

As previously reported,[22,23] animals were given at least 6 days to acclimatize before surgeries were performed. Three days before the mouse clamp studies, a catheter was placed in the upper small intestine (1.5-2 cm distal to the pyloric sphincter) to target the duodenum or in the large intestine (1 cm distal to the cecum) to target the colon, while a catheter was placed in the jugular vein for infusion purposes and tail sampling was performed during the clamp studies. Following surgery, mice were housed individually and maintained on a standard light-dark cycle with ad libitum access to food and water. Food intake and body weight was monitored to ensure recovery from surgery.

Hyperglycemic clamp

After mice were anesthetized, intravenous tube embedding surgery were performed. Mice were allowed to recover for 4 to 5 days individually in cages before intravenous glucose infusion. The hyperglycemic clamp was conducted in conscious and unrestrained mice as previously reported.[96,97] The mice were fasted for 6 h and weighed to calculate the initial glucose infusion rate before the experiment. During experiment, blood samples were collected, and the blood glucose levels were detected with a glucose meter. The glucose infusion rate (GIR) should be adjusted according to blood glucose levels measured 2, 5, 10, 20, 30, 40, 50, 60, 75, and 90 min until plasma glucose levels were clamped at 16-18 mM. The insulin levels were detected by kit and the insulin secretion

curve was drawn when finished the experiment. The area under curve (AUC) were calculated, and 0-10 min and 10-90 min were recognized as first phase and second phase insulin secretion relatively.

Hyperinsulinemic-euglycemic clamp

Mice were allowed to recover for 4 to 5 days after the vascular surgery. Mice were fasted overnight before the experiments. The clamp procedure (180 min) was performed in conscious and unrestrained mice as described.[98] An initial bolus of [6,6-^{2}H] glucose (600 μg kg^{-1}) was administered, followed by continuous infusion of [6,6-^{2}H] glucose (30 μg kg^{-1} min^{-1}) until l termination of the clamp experiment to measure glucose kinetics. Serum samples were obtained at t = 50 and 60 min. Following this basal infusion period, insulin was constantly infused at the rate of 6 mU kg^{-1} min^{-1}. The glucose infusion rate (GIR) should be adjusted according to blood glucose levels measured every 10 min until plasma glucose levels were clamped at 5-6 mM. Serum samples were taken at t = 170 and 180 min. High resolution mass spectrometry coupled with Ultimate 3000 ultra-high performance liquid chromatography (UPLC) was used for the plasma samples analysis.

Serum insulin or C-peptide measurements

The Insulin measurement was determined as previously described.[99] In brief, for serum insulin levels determination, bloods were collected from mice in Glucose clamp experiment in different time points. For serum C-peptide levels determination, bloods were collected from mice at different time points during the hyperinsulinemic clamp. Insulin levels were measured by using an insulin ELISA kit (cat. # CSB-E05071, Cusabio) and C-peptide levels were measured by using a mouse C-peptide ELISA kit (cat. # CEA447Mu, Cloud-Clone Corp).

QUANTIFICATION AND STATISTICAL ANALYSIS

GraphPad Prism version 9.0 and SPSS version 27.0 were used for statistical analysis. The experimental data were shown as the mean ± SEMs. The sample size was estimated based on previous experience, sample availability and previously reported studies. No data were excluded from the data analysis. The normal distribution of the data was determined by the Shapiro-Wilk normality test. For statistical comparisons, unpaired two-tailed Student's t-test (the same standard deviation between two groups) or unpaired two-tailed Student's t-test with Welch's correction (different standard deviation between two groups) one-way ANOVA (between multiple groups) with Tukey's (the same standard deviation) or with Dunnett's T3 test (different standard deviation) analysis was used to compare normally distributed variables. Nonnormally distributed data were compared by the Mann-Whitney U test (between two groups) or the Kruskal-Wallis test (between multiple groups). Multiple groups with two fixed factors, we used ordinary two-way ANOVA, followed by Tukey's test. $P < 0.05$ was considered significant.

Supplemental figures

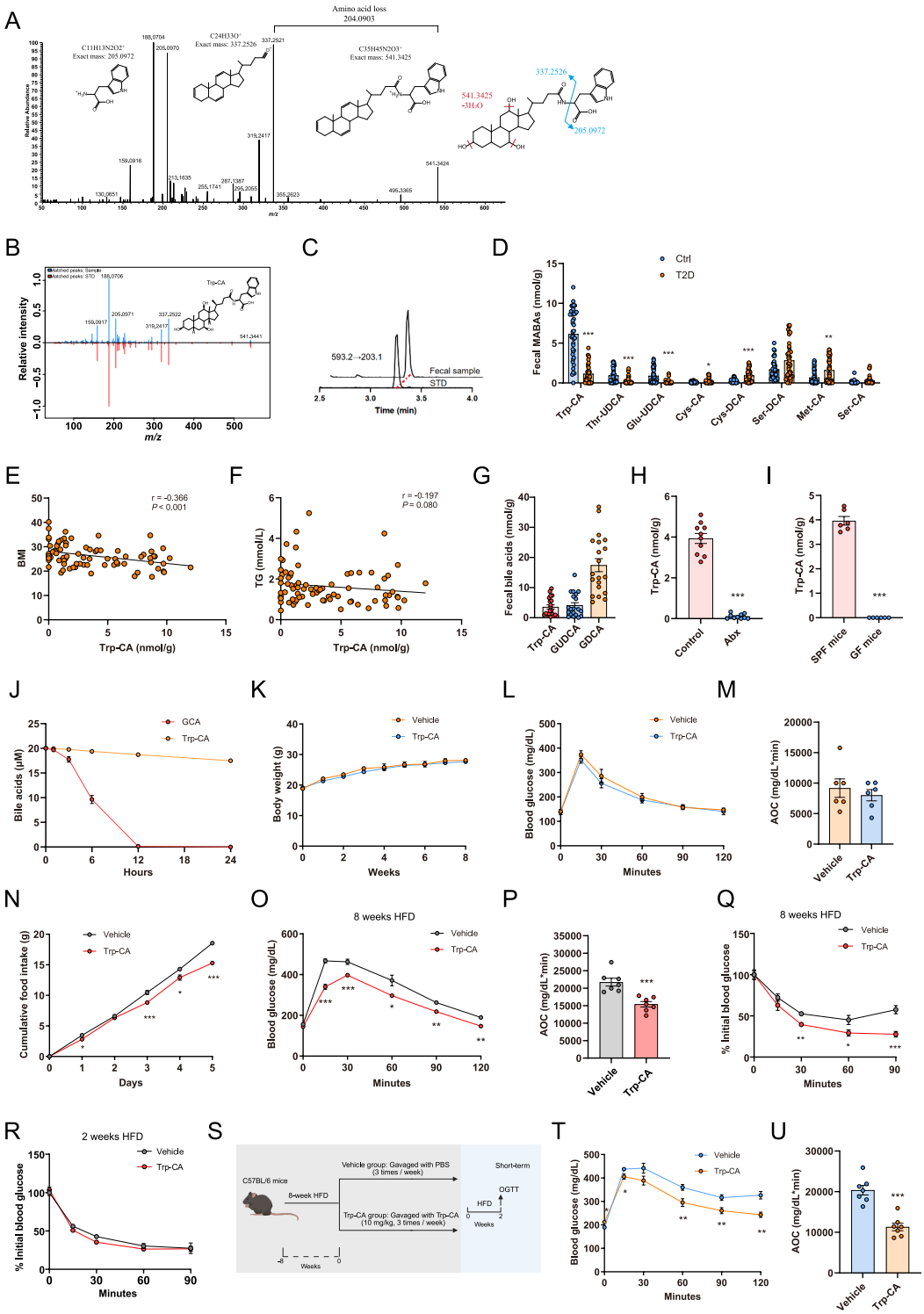

(legend on next page)

Figure S1. Trp-CA alleviates HFD-induced glucose tolerance, related to Figure 1

(A) Annotation of MS/MS fragmentation patterns for the tryptophan-conjugated bile acid (Trp-CA). Structures and related fragment ions are shown.

(B) The MS/MS spectra of the Trp-CA standard (bottom) and detected Trp-CA from the fecal sample of healthy controls.

(C) Extracted ion chromatograms of Trp-CA from fecal samples of healthy controls and Trp-CA standards.

(D) Quantitative data of the MABAs analyzed in the fecal samples between healthy controls and patients with T2D (n = 40/group).

(E and F) Correlative analysis of Trp-CA level with BMI (E) and TG (F) (n = 80). Correlations between variables were assessed by linear regression analysis. Linear correction index r and p values were calculated.

(G) Quantitative data of Trp-CA, GUDCA, and GDCA in stool samples from healthy individuals (n = 20).

(H) 8-week-old SPF mice were divided into two groups: drinking water control or antibiotics in the drinking water (n = 10 mice/group). Fecal Trp-CA level was quantified in SPF mice and antibiotic-treated mice.

(I) Fecal Trp-CA level in SPF mice and germ-free (GF) mice (n = 6 mice/group).

(J) Level of GCA and Trp-CA during the indicated bile acid incubation with stool-derived *ex vivo* communities for 24 h (n = 3 independent incubations).

(K–M) Chow diet-fed C57BL/6 mice were treated with PBS (vehicle), Trp-CA (10 mg/kg) three times per week for the 8 weeks.

(K) Body weight.

(L) Blood glucose in OGTTs.

(M) AOC of OGTTs. n = 6 mice/group.

(N–Q) HFD-fed C57BL/6 mice were treated with PBS (vehicle), Trp-CA (10 mg/kg) three times per week for the 8 weeks.

(N) Cumulative food intake.

(O) Blood glucose in OGTTs of 8-week HFD-fed mice.

(P) AOC of OGTTs.

(Q) Blood glucose in ITTs of 8-week HFD-fed mice. n = 7 mice/group.

(R) Blood glucose in ITTs of 2-week HFD-fed mice with PBS (vehicle), Trp-CA (10 mg/kg) three times per week. n = 7 mice/group.

(S) Experimental scheme for (T) and (U) (n = 7 mice/group). After 8 weeks of HFD-fed, C57BL/6 mice were treated with PBS (vehicle), Trp-CA (10 mg/kg) three times per week for the 2 weeks.

(T) Blood glucose in OGTTs.

(U) AOC of OGTTs.

All data are presented as the means ± SEMs. In (D), the p values were determined by a two-tailed Mann-Whitney U test. In (N), (O), (Q), and (T), the p values were determined by two-way repeated-measures ANOVA with unpaired Student's t test post hoc. In (H), (I), (P), and (U), the p values were determined by a two-tailed Student's t test. $^{*}p < 0.05$, $^{**}p < 0.01$, and $^{***}p < 0.001$ versus the vehicle group.

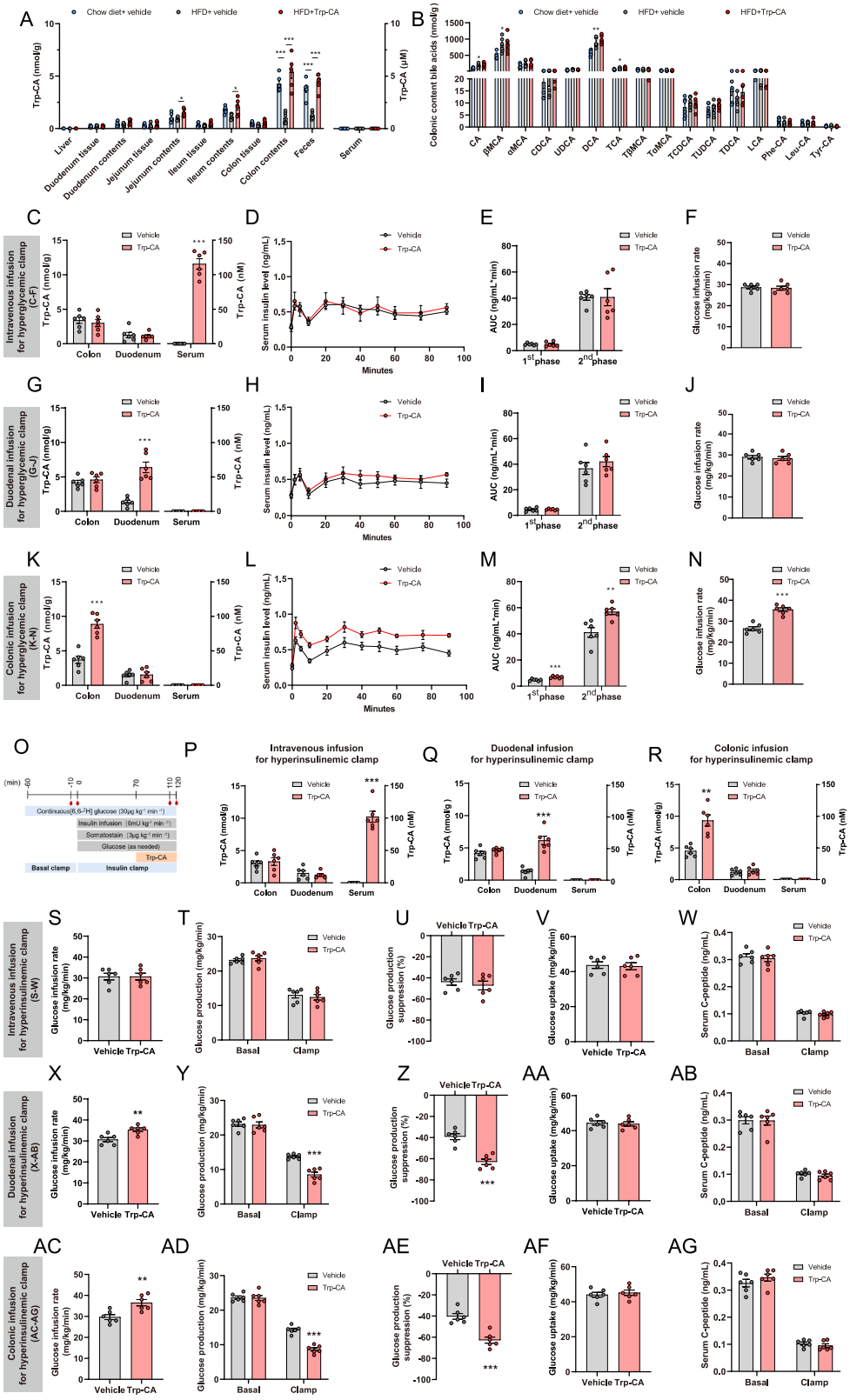

(legend on next page)

Figure S2. Glucose clamps in mice with colonic delivery of Trp-CA, related to Figure 1

(A) Quantifications of Trp-CA in tissues/lumens/feces in mice on chow diet, HFD, and HFD with 2-week Trp-CA gavage. *n* = 6 mice/group.
(B) Quantifications of bile acids in colonic content from mice on a chow diet, HFD, and HFD with 2-week Trp-CA gavage. *n* = 6 mice/group.
(C) Trp-CA levels in serum and gut lumens from mice after intravenous (i.v.) infusion of vehicle or Trp-CA (20 μM, 2 μL/min). *n* = 6 mice/group.
(D–F) Serum insulin levels (D); the AUC of 0–10 min refers to the 1st phase, and 10–90 min refers to the 2nd phase of insulin secretion (E); and GIR (F) during the hyperglycemic clamp in mice with i.v. infusion of vehicle or Trp-CA (20 μM, 2 μL/min). *n* = 6 mice/group.
(G) Trp-CA levels in serum and gut lumens from mice after duodenal infusion of vehicle or Trp-CA (20 μM, 2 μL/min). *n* = 6 mice/group.
(H–J) Serum insulin levels (H); the AUC of 0–10 min refers to the 1st phase, and 10–90 min refers to the 2nd phase of insulin secretion (I); and GIR (J) during the hyperglycemic clamp in mice with duodenal infusion of vehicle or Trp-CA (20 μM, 2 μL/min). *n* = 6 mice/group.
(K) Trp-CA levels in serum and gut lumens from mice after colonic infusion of vehicle or Trp-CA (20 μM, 2 μL/min). *n* = 6 mice/group.
(L–N) Serum insulin levels (L); the AUC of 0–10 min refers to the 1st phase, and 10–90 min refers to the 2nd phase of insulin secretion (M); and GIR (N) during the hyperglycemic clamp in mice with colonic infusion of vehicle or Trp-CA (20 μM, 2 μL/min). *n* = 6 mice/group.
(O) Experimental procedure and hyperinsulinemic-euglycemic clamp protocol of C57BL/6j mice with duodenal, colonic, and i.v. delivery of Trp-CA.
(P) Trp-CA levels in serum and gut lumens from mice after i.v. infusion of vehicle or Trp-CA (20 μM, 2 μL/min). *n* = 6 mice/group.
(Q) Trp-CA levels in serum and gut lumens from mice after duodenal infusion of vehicle or Trp-CA (20 μM, 2 μL/min). *n* = 6 mice/group.
(R) Trp-CA levels in serum and gut lumens from mice after colonic infusion of vehicle or Trp-CA (20 μM, 2 μL/min). *n* = 6 mice/group.
(S–W) GIRs (S), glucose production (T), percent suppression of clamp versus basal glucose production (U), glucose uptake (V), and serum C-peptide level (W) during hyperinsulinemic-euglycemic clamps in mice i.v. infusion of vehicle or Trp-CA (20 μM, 2 μL/min). *n* = 6 mice/group.
(X–AB) GIRs (X), glucose production (Y), percent suppression of clamp versus basal glucose production (Z), glucose uptake (AA), and serum C-peptide level (AB) during hyperinsulinemic-euglycemic clamps in mice duodenal infusion of vehicle or Trp-CA (20 μM, 2 μL/min). *n* = 6 mice/group.
(AC–AG) GIRs (AC), glucose production (AD), percent suppression of clamp versus basal glucose production (AE), glucose uptake (AF), and serum C-peptide level (AG) during hyperinsulinemic-euglycemic clamps in mice colonic infusion of vehicle or Trp-CA (20 μM, 2 μL/min). *n* = 6 mice/group.
All data are presented as the means ± SEMs. In (A) and (B), the *p* values were determined by one-way ANOVA with Tukey's post hoc test. In (K), (M), (N), (X)–(Z), (AC), (AD), and (AE), the *p* values were determined by a two-tailed Student's t test. In (C), (G), and (P)–(R), the *p* values were determined by a two-tailed Student's t test with Welch's correction. $^{*}p < 0.05$, $^{**}p < 0.01$, and $^{***}p < 0.001$ versus vehicle group.

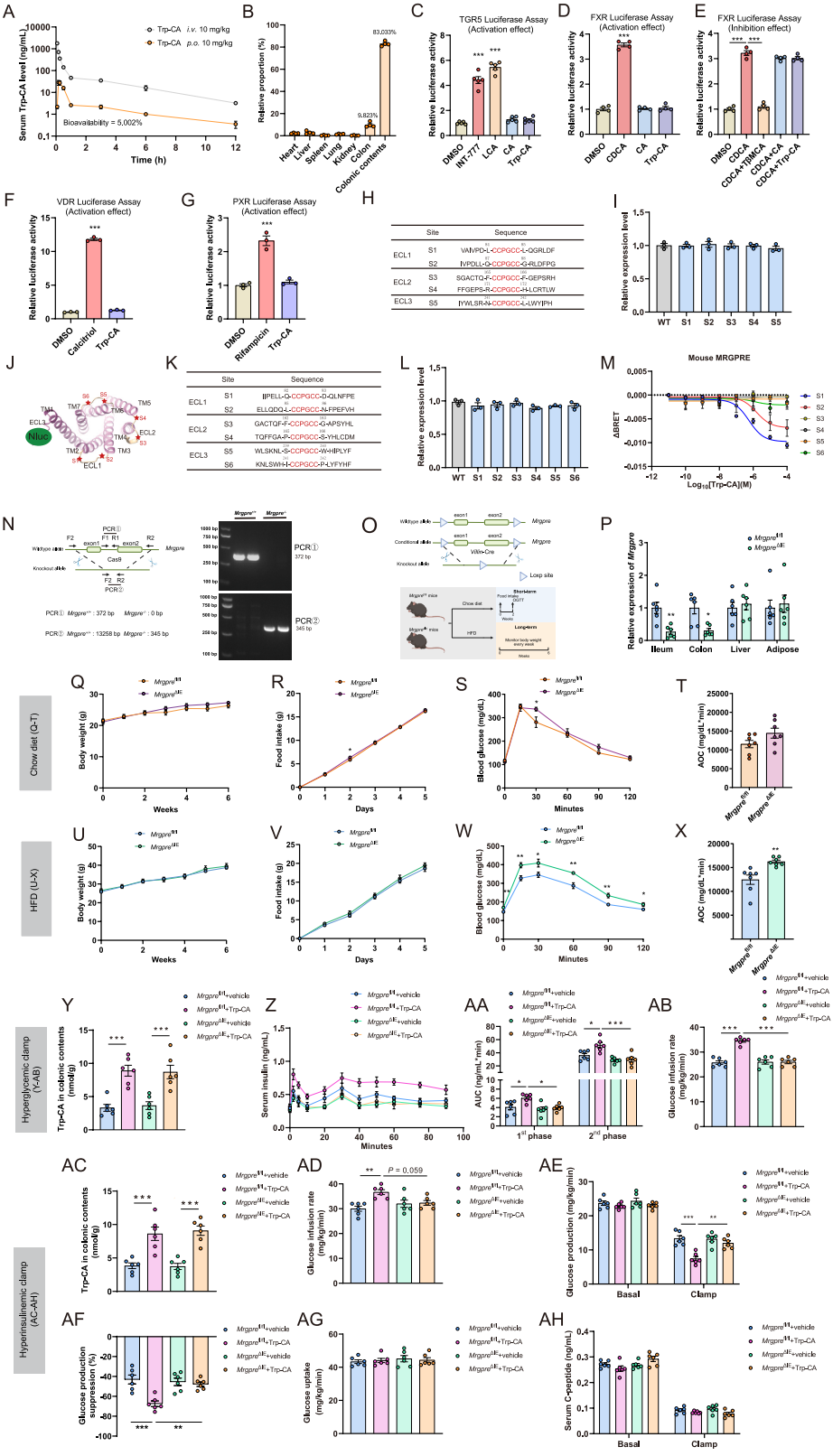

(legend on next page)

Figure S3. Trp-CA is an endogenous ligand of the orphan GPCR receptor MRGPRE, related to Figure 2

(A) Blood pharmacokinetics of 10 mg/kg Trp-CA administered by intravenous injection (i.v.) or oral gavage (p.o.) over time. *n* = 5 mice.

(B) Tissue distribution of Trp-CA at the time of peak plasma concentration (15 min) after being given 10 mg/kg Trp-CA by gavage. *n* = 4 mice.

(C–G) Luciferase activity in HEK293T cells constructed for detecting TGR5 (C) (*n* = 5), FXR (D and E) (*n* = 4), VDR (F) (*n* = 3), and PXR (G) (*n* = 3) activity. The cells were treated with 1 μM INT-777 (TGR5 agonist), 10 μM lithocholic acid (LCA), 10 μM CA, 20 μM chenodeoxycholic acid (CDCA), 50 μM tauro-β-muricholic acid (TβMCA) (FXR antagonist), 10 nM calcitriol (a VDR agonist), 20 μM rifampicin (a PXR agonist), or 10 μM Trp-CA.

(H) Detailed description of the FlAsH motif incorporation site at the ECLs of MRGPRE (human). FlAsH motifs were labeled in red.

(I) ELISA experiments to determine the expression levels of the WT MRGPRE (human) and five FlAsH motif-incorporated FlAsH-BRET sensors.

(J) Schematic representation of the FlAsH-BRET assay design. The nano luciferase (NLUC) was inserted at the N-terminal of MRGPRE (mouse), and the FlAsH motif was inserted in the designated positions in the figure.

(K) Detailed description of the FlAsH motif incorporation site at the extracellular loops of MRGPRE (mouse). FlAsH motifs were labeled in red.

(L) ELISA experiments to determine the expression levels of the WT MRGPRE (mouse) and six FlAsH motif-incorporated FlAsH-BRET sensors. Data were from three independent experiments.

(M) The maximal response of five MRGPRE (mouse) FlAsH-BRET sensors in response to Trp-CA stimulation.

(N) Representative gel picture by using indicated primers to show the deletion of *Mrgpre* in the genome of *Mrgpre*$^{-/-}$ mice.

(O) Experimental scheme for (P)–(X) (*n* = 7 mice/group).

(P) Intestine-specific *Mrgpre* knockout mice (*Mrgpre*$^{\Delta IE}$) were generated by *Villin*-Cre mice and *Mrpgre*$^{fl/fl}$ mice.

(Q–T) Chow diet-fed *Mrpgre*$^{fl/fl}$ and *Mrgpre*$^{\Delta IE}$ mice were monitored for 6 weeks.

(Q) Body weight.

(R) Cumulative food intake.

(S) Blood glucose in OGTTs.

(T) AOC of OGTTs.

(U–X) HFD-fed *Mrpgre*$^{fl/fl}$ and *Mrgpre*$^{\Delta IE}$ mice were monitored for 6 weeks.

(U) Body weight.

(V) Cumulative food intake.

(W) Blood glucose in OGTTs.

(X) AOC of OGTTs.

(Y) Trp-CA levels in colonic contents from *Mrgpre*$^{fl/fl}$ mice and *Mrgpre*$^{\Delta IE}$ mice after colonic infusion of vehicle or Trp-CA in hyperglycemic clamp (20 μM, 2 μL/min). *n* = 6 mice/group.

(Z–AB) Serum insulin levels (Z), the AUC of the first/second phase of insulin secretion (AA), and GIR (AB) during the hyperglycemic clamp in *Mrgpre*$^{fl/fl}$ mice and *Mrgpre*$^{\Delta IE}$ mice with colonic infusion of vehicle or Trp-CA (20 μM, 2 μL/min). *n* = 6 mice/group.

(AC) Trp-CA levels in colonic contents from *Mrgpre*$^{fl/fl}$ mice and *Mrgpre*$^{\Delta IE}$ mice after colonic infusion of vehicle or Trp-CA in hyperinsulinemic-euglycemic clamps (20 μM, 2 μL/min). *n* = 6 mice/group.

(AD–AH) GIRs (AD), glucose production (AE), percent suppression of clamp versus basal glucose production (AF), glucose uptake (AG), and serum C-peptide (AH) during hyperinsulinemic-euglycemic clamps in mice with colonic infusion of vehicle or Trp-CA (20 μM, 2 μL/min). *n* = 6 mice/group.

All data are presented as the means ± SEMs. *n* = 3 biological replicates for (I), (L), and (M). In (C)–(G), the *p* values were determined by one-way ANOVA with Tukey's post hoc test. In (P), the *p* values were determined by a two-tailed Mann-Whitney U test. In (X), the *p* value was determined by a two-tailed Student's t test. In (R), (S), and (W), the *p* values were determined by two-way repeated-measures ANOVA with unpaired Student's t test post hoc. In (Y) and (AA)–(AF), the *p* values were determined by two-way ANOVA with Tukey's post hoc test. $^{*}p < 0.05$ and $^{**}p < 0.01$ versus the control group.

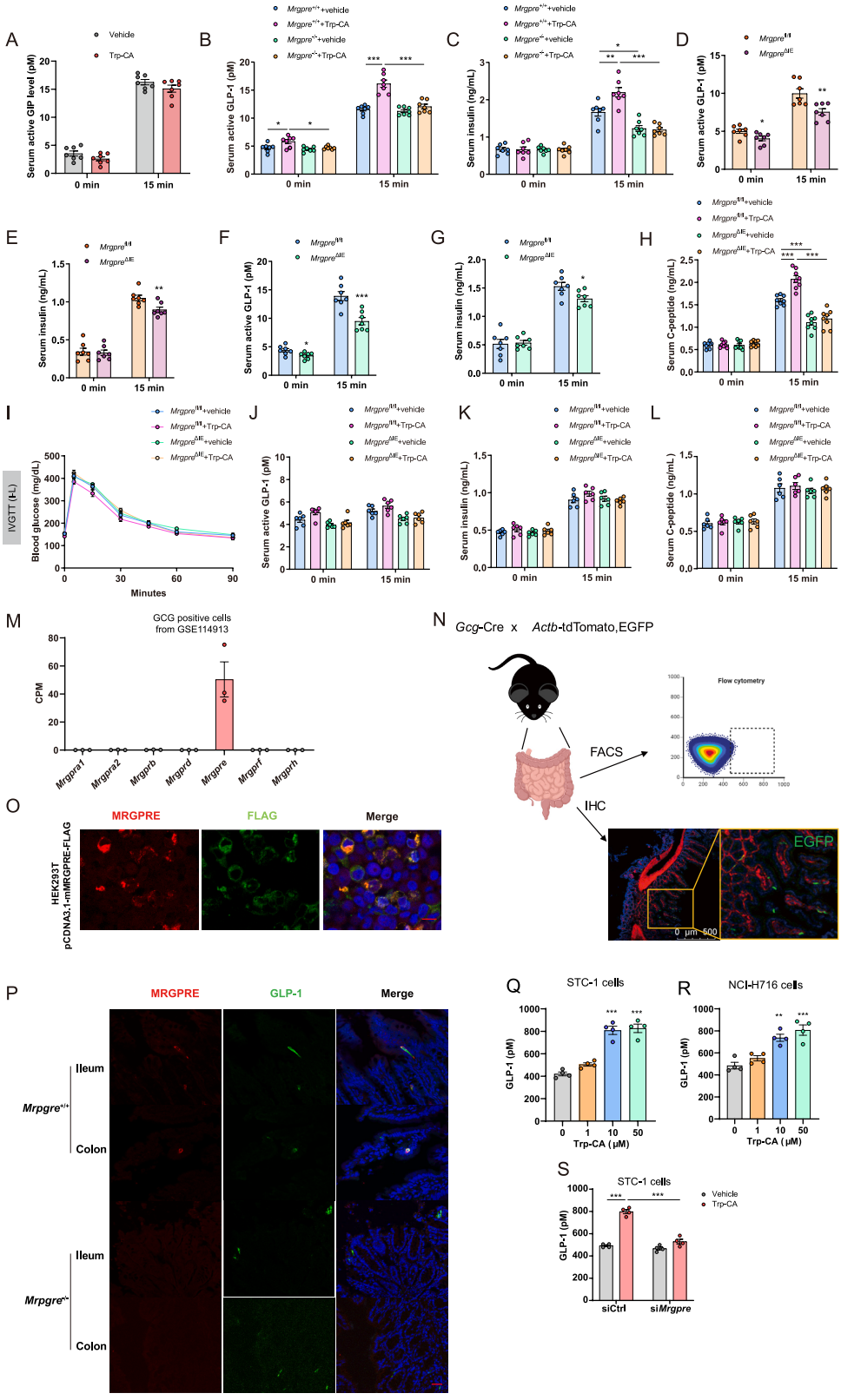

(legend on next page)

Figure S4. Trp-CA promotes GLP-1 secretion by activating MRGPRE, related to Figure 3

(A) HFD-fed C57BL/6 mice were treated with PBS (vehicle), Trp-CA (10 mg/kg) three times per week for the 2 weeks. Serum active GIP-1 levels at 0 and 15 min after oral glucose gavage (n = 7 mice/group). Related to Figure 1L.

(B and C) HFD-fed *Mrpgre*$^{+/+}$ and *Mrgpre*$^{-/-}$ mice were treated with PBS (vehicle), Trp-CA (10 mg/kg) three times per week for 2 weeks (n = 7 mice/group). Serum active GLP-1 (B) and insulin (C) levels at 0 and 15 min after oral glucose gavage.

(D and E) Chow diet-fed *Mrpgre*$^{fl/fl}$ and *Mrgpre*$^{\Delta IE}$ mice were monitored for 6 weeks (n = 7 mice/group). Serum active GLP-1 (D) and insulin (E) levels at 0 and 15 min after oral glucose gavage. Related to Figure S3S.

(F and G) HFD-fed *Mrpgre*$^{fl/fl}$ and *Mrgpre*$^{\Delta IE}$ mice were monitored for 6 weeks (n = 7 mice/group). Serum active GLP-1 (F) and insulin (G) levels at 0 and 15 min after oral glucose gavage. Related to Figure S3W.

(H) Serum C-peptide at 0 and 15 min after oral glucose gavage in 2-week HFD-fed mice with PBS (vehicle), Trp-CA (10 mg/kg) three times per week (n = 8 mice/group). Related to Figure 2K.

(I–L) HFD-fed *Mrpgre*$^{fl/fl}$ and *Mrgpre*$^{\Delta IE}$ mice were treated with vehicle or Trp-CA (10 mg/kg, three times per week) for 2 weeks.

(I) Blood glucose in IVGTT.

(J–L) Serum active GLP-1 (J), insulin (K), and C-peptide (L) levels at 0 and 15 min after i.v. glucose injection (n = 6 mice/group).

(M) CPM of itch family receptors in GCG-positive cells from GEO: GSE114913 dataset.

(N) FACS of intestine epithelial cells dissociated from *Gcg*-Cre; *Actb*-tdTomato/EGFP mouse. Gcg-expressing cells were labeled by EGFP and sorted by FACS.

(O) Co-immunostaining of MRGPRE and FLAG in HEK293 cells transiently transfected with pcDNA3.1-FLAG-mouse MRGPRE. Scale bars, 20 μm.

(P) Co-immunostaining of MRGPRE and GLP-1 in mouse ileum and colon from *Mrpgre*$^{+/+}$ and *Mrgpre*$^{-/-}$ mice. Scale bars, 50 μm.

(Q) Active GLP-1 level in cell culture. STC-1 cells were treated with indicated dose of Trp-CA for 1 h.

(R) Active GLP-1 level in cell culture. NCI-H716 cells were treated with indicated dose of Trp-CA for 1 h.

(S) Active GLP-1 level in cell culture. STC-1 cells transfected with an siCtrl or with an si*Mrgpre* were treated with Trp-CA (10 μM) for 1 h.

All data are presented as the means ± SEMs. n = 4 biological replicates for (Q)–(S). In (A) and (D)–(G), the p values were determined by a two-tailed Student's t test. In (B), (C), (H), (J)–(L), and (S), the p values were determined by two-way ANOVA with Tukey's post hoc test. In (Q) and (R), the p values were determined by one-way ANOVA with Tukey's post hoc test. *$p < 0.05$, **$p < 0.01$, and ***$p < 0.001$ versus the control group.

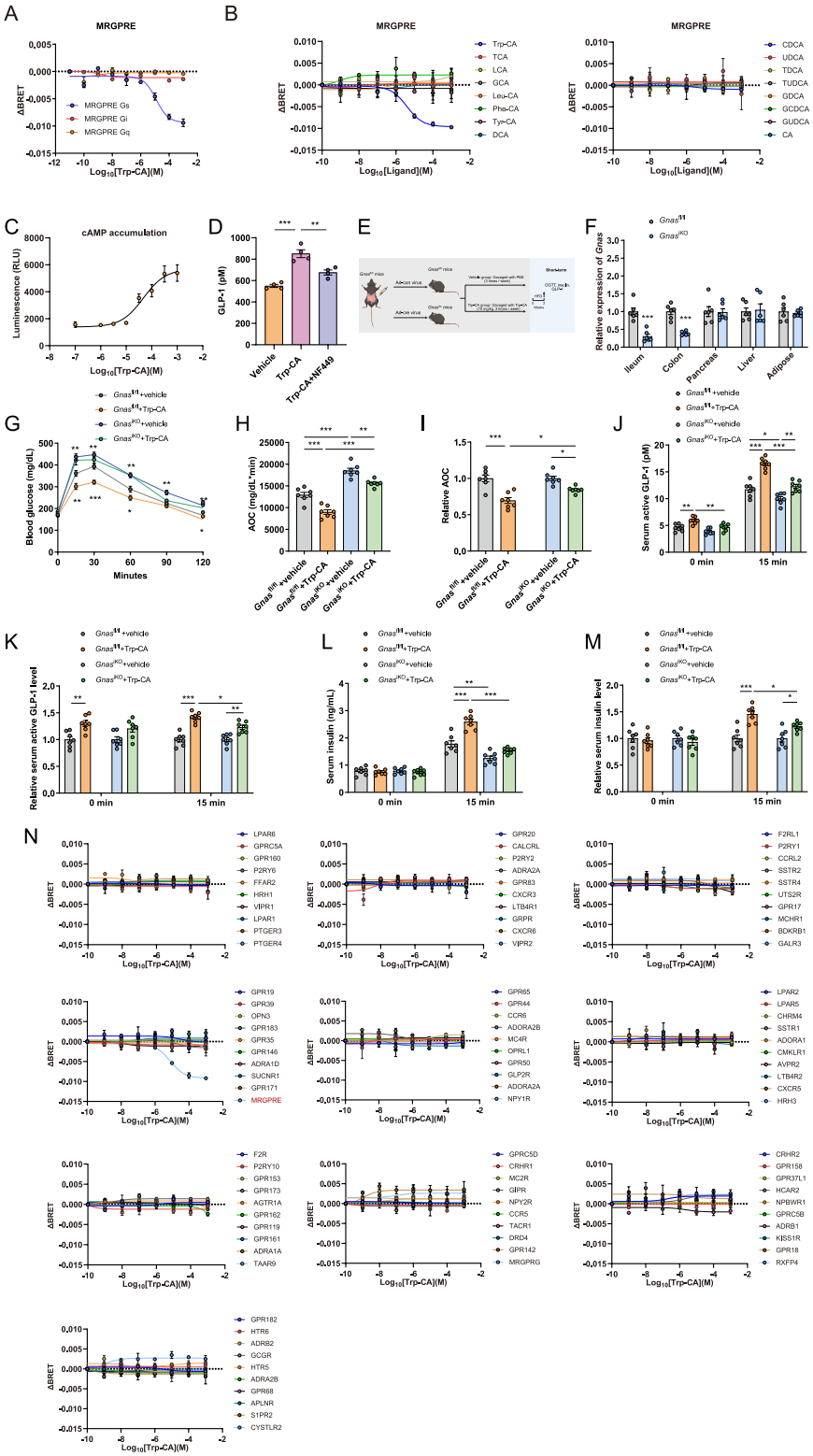

Figure S5. Trp-CA induces GLP-1 secretion partially via an MRGPRE-Gs-cAMP pathway, related to Figure 4

(A) Dose-response curves in HEK293 cells overexpressing hMRGPRE in response to stimulations with Trp-CA by Gαi/Gαs/Gαq-Gγ dissociation assay.

(B) Concentration-dependent curves of Gαs-Gβγ dissociation in hMRGPRE-overexpressing HEK293 cells in response to stimulation with different bile acids or their amino-acid conjugations.

(legend continued on next page)

(C) Dose-response curves of HEK293 cells transfected with hMRGPRE in the cAMP accumulation assay.
(D) Active GLP-1 level in cell culture. GLUTag cells were treated with DMSO (vehicle), 10 μM Trp-CA, and 10 μM Trp-CA plus 10 μM NF449 for 1 h. $n = 4$ biological replicates.
(E) Experimental scheme for (F)–(M) ($n = 7$ mice/group). Intestine-specific *Gnas* knockout mice ($Gnas^{iKO}$) were generated by cre-expressing adenovirus injection into the intestines of $Gnas^{fl/fl}$ mice. HFD-fed $Gnas^{fl/fl}$ and $Gnas^{iKO}$ mice were treated with PBS (vehicle), Trp-CA (10 mg/kg) three times per week for 2 weeks.
(F) Relative gene expression of *Gnas* in different tissues from $Gnas^{fl/fl}$ mice and $Gnas^{iKO}$ mice.
(G) Blood glucose in OGTTs.
(H) AOC of OGTTs.
(I) Relative AOC of OGTTs.
(J–M) Serum active GLP-1 (J), relative active GLP-1 (K), insulin (L), and relative insulin (M) levels at 0 and 15 min after oral glucose gavage.
(N) G-protein signaling of the most highly expressed GPCRs in the intestine was analyzed using a Gαs-Gβγ dissociation assay. Concentration-dependent activity curves of HEK293 cells overexpressing MRGPRE and different GPCRs in response to Trp-CA stimulation.
All data are presented as the means ± SEMs. $n = 3$ biological replicates for (A)–(C) and (N). In (E), the p values were determined by one-way ANOVA with Tukey's post hoc test. In (G), the p values were determined by a two-tailed Student's t test. In (H), the p values were determined by two-way repeated-measures ANOVA with LSD test. In (I)–(N), the p values were determined by two-way ANOVA with Tukey's post hoc test. $^{*}p < 0.05$, $^{**}p < 0.01$, and $^{***}p < 0.001$ versus the control group.

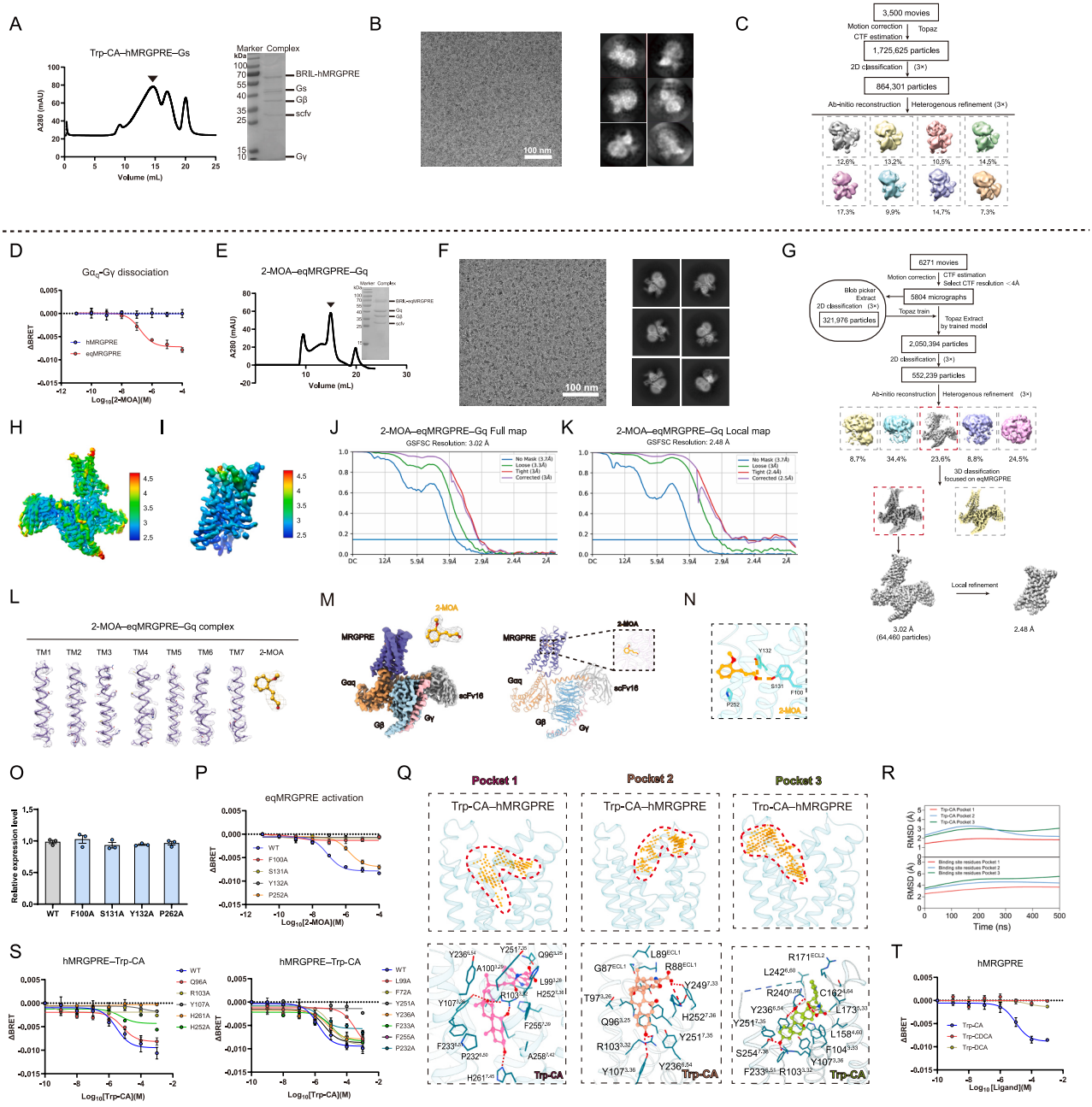

Figure S6. Cryo-EM images and single-particle reconstruction of 2-MOA-eqMRGPRE-Gq complexes and the ligand-binding pockets of the Trp-CA-hMRGPRE-Gs structure, related to Figure 4

(A) Representative elution profiles of *in vitro* reconstituted Trp-CA-hMRGPRE-Gs on Superose 6 increase 10/300 column and SDS-PAGE results of the size-exclusion chromatography peak.

(B) Representative cryo-EM micrograph and two-dimensional (2D) class averages of Trp-CA-hMRGPRE-Gs particles (scale bar, 100 nm).

(C) Flow chart for three-dimensional (3D) classification of Trp-CA-hMRGPRE-Gs particles. Representative cryo-EM micrographs from 3,500 movies and representative 2D class averages determined using approximately 864,301 particles after 3D classification are shown. Initial micrographs were processed with UCSF MotionCor2 and cryoSPARC.

(D) Dose-dependent curve by Gαq-Gγ dissociation assay in HEK293 cells transfected with hMRGPRE or eqMRGPRE in response to 2-MOA stimulation.

(E) Representative elution profiles of *in vitro* reconstituted 2-MOA-eqMRGPRE-Gq on Superose 6 increase 10/300 column and SDS-PAGE results of the size-exclusion chromatography peak.

(F) Representative cryo-EM micrograph and two-dimensional (2D) class averages of 2-MOA-eqMRGPRE-Gq particles (scale bar, 100 nm).

(G) Flow chart for three-dimensional (3D) classification of 2-MOA-eqMRGPRE-Gq particles. Representative cryo-EM micrographs from 6,271 movies and representative 2D class averages determined using approximately 552,239 particles after 3D classification are shown. Initial micrographs were processed with

(legend continued on next page)

UCSF MotionCor2 and cryoSPARC. 3D volume of classes and refinements are shown, and red box indicates selected classes. We have performed mask for receptor-alone for 2-MOA-eqMRGPRE-Gq complex structures. The result indicated that mask of receptor region in 2-MOE-eqMRGPRE-Gq complex improved the map quality of specific region of eqMRGPRE.

(H and I) Cryo-EM map colored based on local resolution for full map (H) and receptor-masked map (I) of 2-MOA-eqMRGPRE-Gq complex.

(J and K) Gold standard Fourier shell correlation (GSFSC) curves of full map (J) and receptor-masked map (K) at 0.143 threshold.

(L) Cryo-EM density maps and models are shown for 2-MOA, TM1, TM2, TM3, TM4, TM5, TM6, and TM7 of eqMRGPRE and α5 helix of Gαs in the 2-MOA-eqMRGPRE-Gq complex using the global map of 2-MOA-eqMRGPRE-Gq complex with map threshold at 0.20.

(M) Cryo-EM map and ribbon representation of eqMRGPRE-Gq complex. MRGPRE, slate blue; Gαs, orange; Gβ, light blue; Gγ, pink; scFv16, light gray; 2-methoxycinnamaldehyde (MOA), dark orange.

(N) 3D representation of the detailed interactions of 2-MOA with the pocket residues of eqMRGPRE. Hydrogen bonds or polar interactions are shown as orange dashed lines.

(O) ELISA experiments to determine the expression levels of the WT eqMRGPRE and key residues in 2-MOA-binding pocket of eqMRGPRE.

(P) Dose-response curves of mutations of key residues in 2-MOA binding pocket of eqMRGPRE in response to stimulation with 2-MOA by G protein dissociation assay.

(Q) Three predicted ligand-binding pockets in the hMRGPRE as determined using the SiteMap algorithm. The predicted ligand-binding pockets are filled with orange balls. 3D representation of the detailed interactions between Trp-CA and hMRGPRE in predicted pockets 1, 2, and 3. Hydrogen bonds or polar interactions are shown as red dashed lines.

(R) The average RMSD value of Trp-CA (upper) and binding site residues (lower) in Trp-CA-MRGPRE complex during triplicate 200 ns MD simulations.

(S) Dose-response curves of mutations of key residues in Trp-CA-binding pocket of MRGPRE in response to stimulation with Trp-CA by G protein dissociation assay.

(T) Dose-response curves of hMRGPRE in response to stimulation with Trp-CA, Trp-CDCA, and Trp-DCA by Gαs-Gβγ dissociation assay.

All data are presented as the means ± SEMs. n = 3 biological replicates for (D), (O), (P), (S), and (T).

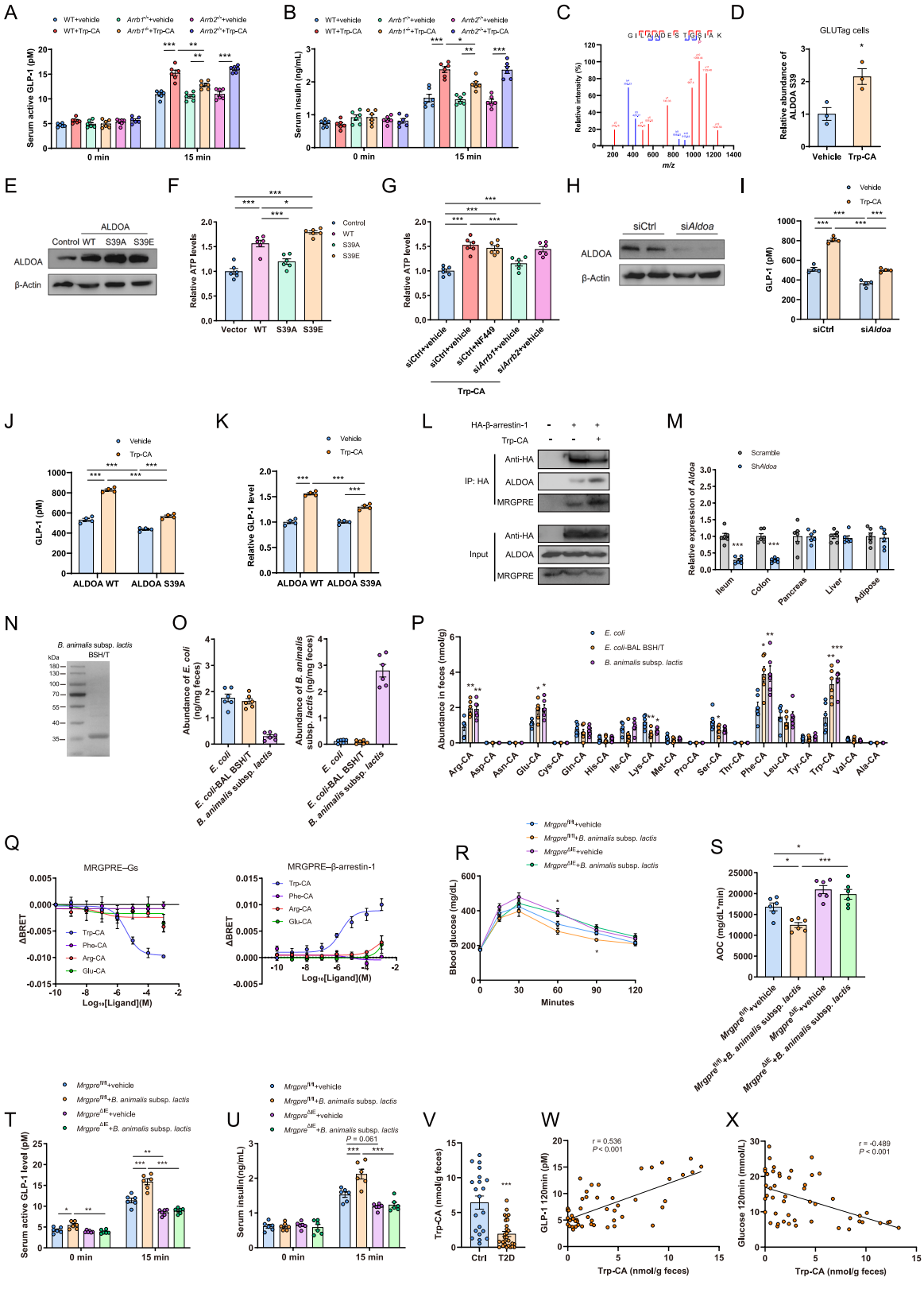

(legend on next page)

Figure S7. Trp-CA induces GLP-1 secretion partially via an MRGPRE-β-arrestin-1-ALDOA pathway, and BSH/T of *B. animalis* subsp. *lactis* produces Trp-CA, related to Figures 5, 6, and 7

(A and B) HFD-fed *Arrb1*$^{-/-}$ and *Arrb2*$^{-/-}$ mice were treated with PBS (vehicle), Trp-CA (10 mg/kg) three times per week for 2 weeks. Serum active GLP-1 (A) and insulin (B) levels at 0 and 15 min after oral glucose gavage. n = 6 mice/group.

(C) Representative higher-energy collisional dissociation (HCD) spectra showing the identification of the phosphopeptides of ALDOA (Ser39) by mass spectrometry.

(D) Quantification of the phosphorylation level of ALDOA (Ser39) in GLUTag cells treated with vehicle or 10 μM Trp-CA. n = 3 biological replicates.

(E) Immunoblot analysis of whole-cell extract from GLUTag cells transfected with empty vector (control), ALDOA WT, ALDOA S39A mutant, and ALDOA S39E mutant.

(F) Relative ATP level of cell lysates from GLUTag cells transfected with empty vector (control), ALDOA WT, ALDOA S39A mutant, and ALDOA S39E mutant.

(G) Relative ATP levels of cell lysates from GLUTag cells transfected with an siCtrl or with an si*Arrb1* or with an si*Arrb2* were treated with DMSO (vehicle), 10 μM Trp-CA, and 10 μM Trp-CA plus 10 μM NF449 for 1 h.

(H) Immunoblot analysis of whole-cell extract from GLUTag cells transfected with an siCtrl or with an si*Aldoa*.

(I) Active GLP-1 level in cell culture. GLUTag cells transfected with an siCtrl or with an si*Aldoa* were treated with DMSO (vehicle) and 10 μM Trp-CA for 1 h. Related to Figure 6F.

(J) Active GLP-1 level in cell culture. We constructed new ALDOA-overexpressing plasmids, which the si*Aldoa*-targeted sequence was synonymously mutated to avoid degrading. GLUTag cells transfected with an si*Aldoa* and ALDOA WT/ALDOA S39A were treated with DMSO (vehicle) and 10 μM Trp-CA for 1 h.

(K) Relative active GLP-1 level in cell culture. Related to (J).

(L) Immunoblot analysis of whole-cell extracts that were immunopurified by anti-HA immunoprecipitation (HA-IP) from GLUTag cells expressed HA-β-arrestin-1. Where indicated, the cells were pretreated with or without 10 μM Trp-CA for 10 min.

(M) Relative gene expression of *Aldoa* in different tissues from scramble mice and sh*Aldoa* mice (n = 6 mice/group).

(N) Coomassie-stained SDS-PAGE of purified *B. animalis* subsp. *lactis* (BAL) BSH/T.

(O) Colonization efficiency of *E. coli* (left) and *B. animalis* subsp. *lactis* (right) in feces of *E. coli*, *E. coli*-BAL BSH/T, and *B. animalis* subsp. *lactis*-treated mice (n = 6 mice/group).

(P) Fecal MABAs level in mice after control *E. coli*, *E. coli*-BAL BSH/T, and *B. animalis* subsp. *lactis* colonization (n = 6 mice/group).

(Q) Dose-response curves of hMRGPRE in response to stimulation with Trp-CA, Phe-CA, Arg-CA, and Glu-DCA by Gαs-Gβγ dissociation assay and β-arrestin-1 recruitment assay. n = 3 biological replicates.

(R–U) HFD-fed *Mrpgre*$^{fl/fl}$ and *Mrgpre*$^{\Delta IE}$ mice were treated with or without *B. animalis* subsp. *lactis* one time per week for 2 weeks (n = 6 mice/group).

(R) Blood glucose in OGTTs.

(S) AOC of OGTTs.

(T and U) Serum active GLP-1 (T) and insulin (U) levels at 0 and 15 min after oral glucose gavage.

(V) Fecal Trp-CA level in healthy controls (n = 21) and diabetic patients (n = 28).

(W) Correlative analysis of fecal Trp-CA level and GLP-1 level at 120 min after oral glucose gavage (n = 49)

(X) Correlative analysis of fecal Trp-CA level and glucose level at 120 min after oral glucose gavage (n = 49).

All data are presented as the means ± SEMs. n = 4 biological replicates for (I)–(K). n = 6 biological replicates for (F) and (G). In (A), (B), (I)–(K), and (S)–(U), the p values were determined by two-way ANOVA with Tukey's post hoc test. In (D) and (V), the p values were determined by a two-tailed Student's t test. In (F), (G), and (P), the p values were determined by one-way ANOVA with Tukey's post hoc test. In (M), the p values were determined by a two-tailed Student's t test with Welch's correction. In (R), the p values were determined by two-way repeated-measures ANOVA with LSD test. *$p < 0.05$, **$p < 0.01$, and ***$p < 0.001$ versus the control group.